The Regional Oceanic Modeling System: A Split-Explicit, Free-Surface, Topography-Following-Coordinate Oceanic Model

Alexander F. Shchepetkin
and
James C. McWilliams

Institute of Geophysics and Planetary Physics,
University of California at Los Angeles,
405 Hilgard Avenue, Los Angeles, CA 90024-1567

e-mail: *alex@atmos.ucla.edu* *jcm@atmos.ucla.edu*

March 10, 2003

Abstract. Following Blumberg & Mellor, 1987, Bleck & Smith, 1990, and Killworth *et al.*, 1991, split-explicit free-surface versions have been developed for the three major types of oceanic models: sigma, isopycnic, and $Z-$coordinates. Besides the implied time-scale separation, splitting into barotropic and baroclinic modes typically relies on the smallness of the free-surface elevation relative to the total water depth and the smallness of density variations in a Boussinesq sense. Once separate time-stepping algorithms are used for the barotropic mode and the three-dimensional part, the continuity equation holds only within the order of discretization accuracy, but not exactly for the baroclinic time step. The discrepancy is associated with details of the time evolution of barotropic mass fluxes and free surface within the baroclinic step that are typically averaged out to avoid numerical instability. At the same time, conservative, flux-divergent discretizations for the tracer equations (*i.e.,* heat content, salinity, *etc.*) require that the implied three-dimensional continuity equation holds exactly on the time-discrete level in order to simultaneously maintain *volume conservation* and *constancy preservation* properties for tracers. The inconsistency in the discrete continuity equation causes biases in tracer values proportional to the tracer value itself, the ratio of free-surface elevation change to the water depth, and a factor depending on the difference in temporal discretization errors of the barotropic and baroclinic modes. Although this error is typically small for basin-scale configurations, it can become significant and cause non-physical behavior and even numerical instability in coastal regions, estuaries, and fjords where the free-surface change is not very small relative to the total depth.

In the present study we propose a split-explicit hydrodynamic kernel of the model which utilizes consistent temporal averaging of barotropic mode to allow both exact conservation and constancy preservation properties for tracers. Due to mathematical feedback between the momentum and density equations (via temperature and salinity) for the baroclinic mode and, similarly, between the free surface and barotropic momentum equations, it is advantageous to treat both modes in such a way that after a time step for the momentum equation is complete, the computed velocities participate immediately in the computation of tracers and *vice versa* (rather than advancing all equations for one time step simultaneously). This leads to a new family of time-stepping algorithms that introduce *forward-backward* feedback into the best known synchronous schemes. This allows an increased time step due to the enhanced internal stability of the algorithm without sacrificing its accuracy. An additional gain in stability is achieved by a more accurate mode-splitting of pressure-gradient terms in which the barotropic sub-model retains information about the local density stratification via a specially designed vertical averaging of density and pressure.

1. Introduction

The motivation to build a free-surface oceanic model is twofold. From a physical point of view, it is desirable to recapture processes lost or altered by the rigid-lid assumption. These include tidal motions, altered dispersion relations for the Rossby waves, *etc.* The other motivation comes from computational economics: as pointed out by Killworth *et al.*, 1991, there is a natural physical ratio of phase speeds for the external and internal gravity-wave modes. Once the model time step is chosen from the CFL criterion based on the fastest baroclinic wave speed, the external mode has to be treated by either (*i*) a streamfunction method using rigid-lid approximation; or (*ii*) a two-dimensional pressure Poisson equation for pressure on the rigid-lid or due to free-surface elevation; or (*iii*) a special two-dimensional barotropic submodel that uses a smaller time step chosen from a CFL criterion based on the barotropic speed. Approaches (*i*)-(*ii*) require solution of a two-dimensional elliptic problem (Dukowitz, 1994; Dukowitz & Smith, 1994) at every time step that, with a conventional Successive Over-Relaxation (SOR) or similar method, requires a number of iterations of the order of the number of grid points in the longest direction of the computational domain. Since on this path the number of operations needed to be performed at every grid point at every time step tends to increase with the increase of resolution, on finer grids the approach (*iii*) tends to be more efficient than the others with threshold set by the ratio of phase speeds of the external and the fastest internal gravity waves compared to the number of grid points in the longest dimension[1],

$$\frac{|V_{\text{ext}}|}{|V_{\text{int}}|\cdot\max\left(N_x,N_y\right)}\,. \tag{1.1}$$

Despite the long-time existence of split-explicit versions for all three major classes of oceanic models — z-, sigma-, and density-coordinate — there are only few published studies about the mathematical aspects: consistency, accuracy and stability associated with mode splitting (*e.g.,* Higdon & Bennett, 1996; Higdon & de Szoeke, 1997; Hallberg, 1997; as well as an earlier theoretical work Yanenko, 1971; and Skamarock & Klemp, 1992 more related to atmospheric modeling). It has been shown that even within the limits of numerical stability based on the usual CFL condition, mode splitting may introduce additional sources of numerical instability that are not present in models with uniform time steps nor in rigid-lid models.

The purpose of the present study is to reconsider the computational kernel of an oceanic model, including the optimal choice of time-stepping algorithms for the barotropic and baroclinic momentum equations, tracer equations, and their mutual interaction. Here we advocate an integral approach whose main focus is on time-step limitations coming from the system as a whole that, as we will show, are typically more restrictive than the CFL limitations coming from each equation taken individually. We design a finite-volume, finite-time-step discretization for the tracer equations in order to eliminate the conflict between integral conservation and constancy preservation properties associated with the variable free surface. We alternatively define the barotropic mode splitting to take into account the variable density. Collectively, these steps reduce the mode-splitting error and improve the stability and robustness of the model.

1.1. A Generalized Topography-Following Coordinate

The topography-following vertical coordinate system implies that there is a transformation,

$$z=z(x,y,\sigma)\,, \tag{1.2}$$

where z is the Cartesian height, σ is the vertical distance from surface to the point an depth z measured as the fraction of the local water column thickness (*i.e.,* $-1\le\sigma\le 0$, where $\sigma=0$ corresponds to the free surface, $z=\zeta$, and $\sigma=-1$ corresponds to the oceanic bottom, $z=-h(x,y)$). The resulting system of coordinates is nonorthogonal; however, it is usually assumed that the vertical to horizontal aspect ratio is very small so one can neglect some of the associated curvilinear coordinate metric terms and the coordinate transformation reduces to the set of chain rules for derivatives,

$$\left.\frac{\partial}{\partial x}\right|_z=\left.\frac{\partial}{\partial x}\right|_\sigma-\left.\frac{\partial z}{\partial x}\right|_\sigma\cdot\frac{\partial}{\partial z}\,. \tag{1.3}$$

In the simplest case (1.2) reduces to

$$z=\sigma\cdot h(x,y)\,, \tag{1.4}$$

which is the classical σ-coordinate. A more general system of coordinate uses nonlinear mapping function, $S(\sigma)$,

$$z(x,y,\sigma)=S(\sigma)\cdot h(x,y)\,. \tag{1.5}$$

---

[1] This criterion may be shifted in favor of the rigid-lid model if a more efficient (*e.g.,* conjugate gradient, direct, or multigrid, Multigrid Methods, 1981) elliptic solver is used instead of SOR. These kinds of solvers are available for relatively simple geometries but not for general complex geometry and topography. This justifies the utility of all three types of models: rigid-lid streamfunction; implicit free-surface pressure; and split-explicit. Similarly, if the rigid-lid is abandoned in favor an implicit free-surface approach, the associated elliptic operator becomes diagonally-dominant, which alleviates the requirements for the solver and ultimately helps to reduce the computational cost, Dvinsky & Dukowicz, 1993; Dukowitz *et al.*, 1993; Dukowitz & Smith, 1994.

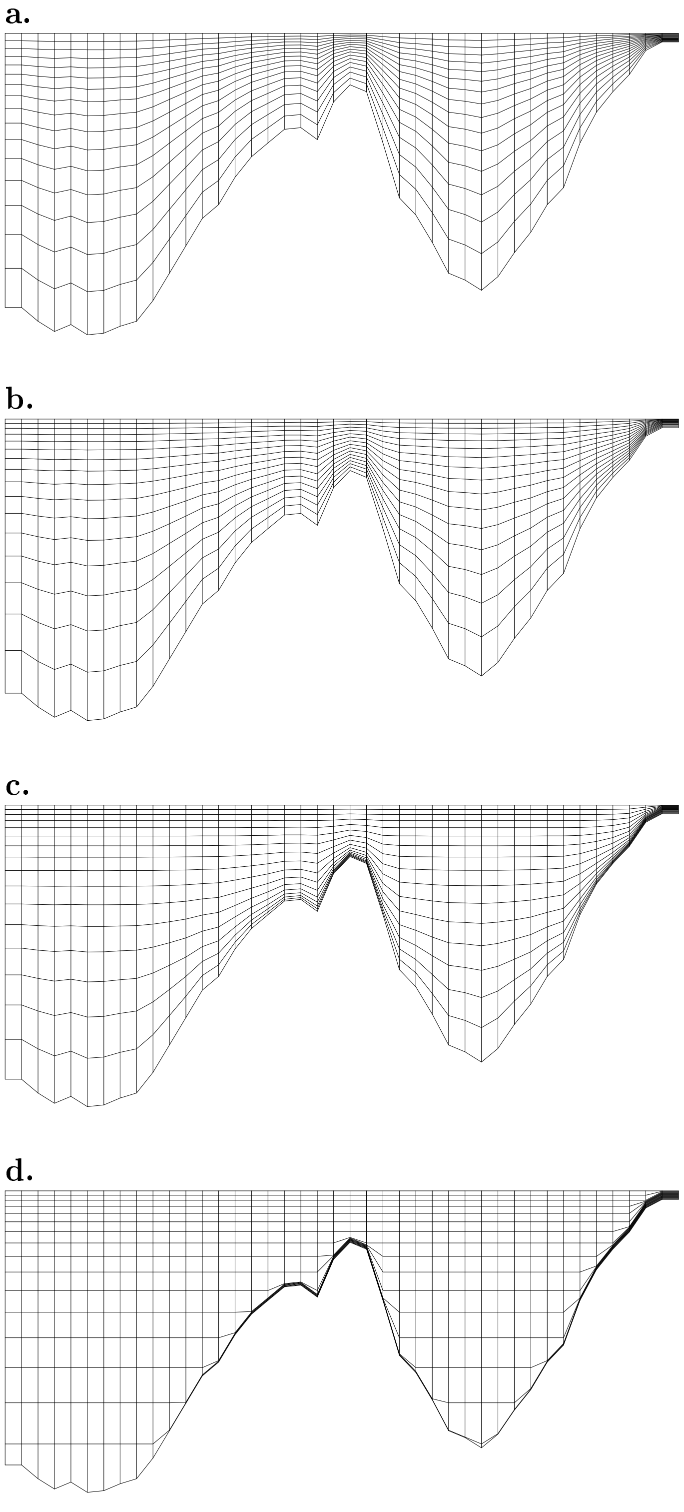

Figure 1. Vertical coordinate systems: **a:** s-coordinate of Song & Haidvogel, 1994 with $\theta_s = 3$, $\theta_b = 0.01$; **b,c:** Hybrid $z-\sigma$ coordinate systems obtained by relaxing the z-coordinate system **d** toward the s-coordinate.

which can be viewed as a special case of (1.2), classified as a separable coordinate transformation in the sense that $S(\sigma)$ that does not depend on the horizontal coordinates.

Song & Haidvogel, 1994 introduced a quasi-separable vertical S-coordinate,

$$z(x,y,\sigma) = \sigma \cdot h_{\min} + C(\sigma) \cdot \big(h(x,y) - h_{\min}\big)\,, \qquad (1.6)$$

where

$$C(\sigma) = (1-\theta_b)\frac{\sinh(\theta\sigma)}{\sinh(\theta)} + \frac{1}{2}\theta_b\left[\frac{\tanh\left[\theta(\sigma+1/2)\right]}{\tanh(\theta/2)} - 1\right]\,,$$

and θ, θ_b are non-dimensional parameters controlling the vertical coordinate stretching. This system has an advantage over both (1.4) and (1.5) by allowing stretched coordinates selectively in the deep fraction of the water column (giving the possibility of concentrating much of the vertical resolution within the thermocline) while producing uniform vertical grid spacing in the shallowest fraction to avoid making the topmost grid-cells too small and making a severe CFL restriction. An example of such coordinate transformation is shown in Fig. 1a.

Past experience with σ-coordinate models and intercomparisons with z-coordinate and isopycnic models (Beckmann, 1998; Willebrand, *et al.*, 2001) reveals that the solutions from σ-models exhibit stronger topographic sensitivity than the other two classes of models. This is attributed to the fact that the isosurfaces of vertical coordinate intersect the isopycnals at some angle, even in the case of horizontally uniform stratification and cause pressure-gradient error. One way to address this problem is to redesign the model algorithms to make them less sensitive to such errors (Shchepetkin & McWilliams, 2003). It is also desirable to allow the possibility of smooth transition from σ to z-coordinates, such that the top-most isosurfaces are nearly flat while the bottom-most are still aligned with topography. Such a general system of coordinates is no longer separable in the sense that it cannot be generated by the simple relationships (1.5) or (1.6) but involves a full three-dimensional transformation (1.2).

For example, one can chose a set of z-levels, $\left\{z^*_{k+\frac{1}{2}} \,|\, k = 0,1,...,N\right\}$, where $z^*_{\frac{1}{2}} = -h_{\max}$ is chosen to be the maximum depth and $z^*_{N+\frac{1}{2}} = 0$ is the unperturbed free surface [2]. Then, starting from the bottom, for $k=0$ set

$$z_{\frac{1}{2}}(x,y) = -h(x,y)\,, \qquad (1.7)$$

---

[2] For notational consistency throughout the paper, $z^*_{k+\frac{1}{2}}$ have half-integer indices to reflect the fact that these z-levels are placed between the tracer point levels on a vertically staggered grid. Specifically, these z-levels correspond to interfaces between two adjacent grid boxes in the finite-volume discretization described below.

and for each $k = 1, ..., N-1$ set

$$z_{k+\frac{1}{2}}(x,y) = \max\left(z^{*}_{k+\frac{1}{2}}\,,\, z_{k-\frac{1}{2}}(x,y) + \Delta z_{\min}\right)\,, \qquad (1.8)$$

where $\Delta z_{\min}$ is the chosen minimal vertical grid spacing (*n.b.,* to avoid surfacing of coordinate isolines, $\Delta z_{\min} \leq h_{\min}/N$, where $h_{\min}$ is the minimal depth). In principle, $\Delta z_{\min}$ may be chosen to be infinitely small, so the resultant system is equivalent to a z-coordinate with the necessity of handling the layers near the bottom as "massless" layers. Its disadvantage is the non-smooth transition from z-level to topography-following regions. This non-smoothness can be repaired by applying two-dimensional diffusion to $z_{k+\frac{1}{2}}$, with variable diffusivity coefficient — zero for the bottom and increasing toward the surface. The resultant coordinate systems are shown in Fig. 1b-d for the cases of two different degrees of smoothing: case (b) is closer to the stretched σ-coordinate, while (c) retains more features of the original z-coordinate (d). Unlike the σ-coordinate, in both cases the coordinate surfaces near the top are almost horizontal and have less resemblance to the topography.

As an alternative to using a smooth coordinate system, one can design vertical discretizations tolerant of non-smoothness. For example, later we describe an option of reconstructing vertical density profiles by conservative parabolic splines that do not require a smooth grid. Another potentially attractive possibility is to construct a dynamically adaptive vertical grid depending on the evolving density field that concentrates resolution in the vicinity of pycnocline while also avoiding difficulties associated with isopycnic coordinates (*e.g.,* Dietachmayer & Droegemeier, 1992). In this study we assume that the vertical transformation (1.2) is generally non-separable; hence, the applicability of the methods developed here is not limited to just a σ- or S-coordinate class of models.

1.2. Perturbed Vertical Coordinate System

Discretization of vertical coordinate $z(x,y,\sigma)$ introduces a set of σ-isosurfaces,

$$\left\{z_{k+\frac{1}{2}}(x,y) = z(x,y,\sigma_{k+\frac{1}{2}})\,,\;\; k = 0, 1, ..., N\right\}. \qquad (1.9)$$

If the ocean is at rest, the free-surface elevation is $\zeta = 0$, hence $z_{N+\frac{1}{2}} = 0$, and the whole set corresponding to zero free-surface $\left\{z^{(0)}_{k+\frac{1}{2}}\right\}$ is referred as an unperturbed coordinate system. In the case of a non-zero ζ, all $z_{k+\frac{1}{2}}$ are displaced by a distance proportional to ζ and the distance from the bottom as the fraction of unperturbed local depth,

$$z_{k+\frac{1}{2}} = z^{(0)}_{k+\frac{1}{2}} + \zeta \cdot \frac{z^{(0)}_{k+\frac{1}{2}} + h}{h} \qquad (1.10)$$

(recall that $z_{\frac{1}{2}} \equiv z^{(0)}_{\frac{1}{2}} \equiv -h$ and $z_{N+\frac{1}{2}} \equiv \zeta$). As a result the perturbed grid-box height, $\Delta z_k \equiv z_{k+\frac{1}{2}} - z_{k-\frac{1}{2}}$, is related to the unperturbed height, $\Delta z^{(0)}_k \equiv z^{(0)}_{k+\frac{1}{2}} - z^{(0)}_{k-\frac{1}{2}}$ according to

$$\Delta z_k = \Delta z^{(0)}_k \left(1 + \frac{\zeta}{h}\right)\,, \qquad (1.11)$$

where the multiplier $(1 + \zeta/h)$ is independent of the vertical coordinate. This choice is similar to Higdon & Bennett, 1996, Higdon & de Szoeke, 1997, with the exception that they applied it for an isopycnic coordinate model. But is different from Killworth *et al.*, 1991, Dukowitz & Smith, 1994, where free-surface elevation affects only the top-most grid box, as well as from Song & Haidvogel, 1994, where the displacement by ζ is distributed linearly in σ-space, rather than in z-space. Later we show that (1.11) has several consequences, including the fact that vertical mass fluxes generated by a purely barotropic motion vanish identically at every interface, $z_{k+\frac{1}{2}}$.

1.3. Conflict Between Integral and Constancy Preservation for Tracers

Combining the tracer equation in advective form,

$$\frac{\partial q}{\partial t} + (\mathbf{u} \cdot \nabla) q = 0 \qquad (1.12)$$

with the nondivergence equation,

$$(\nabla \cdot \mathbf{u}) = 0\,, \qquad (1.13)$$

we derive the tracer equation in conservation form,

$$\frac{\partial q}{\partial t} + \nabla \cdot (\mathbf{u} q) = 0\,. \qquad (1.14)$$

As a consequence of (1.12), if the tracer is specified as a constant filed at the initial time, it remains so regardless of the velocity field. On the other hand, as a consequence of (1.14), the volume integral of the tracer concentration is conserved in the absence of incoming and outgoing fluxes across the boundary of the domain. The continuity equation (1.13) provides the compatibility condition between these two properties. Both properties are valuable and should be considered in constructing numerical oceanic models.

The discretization of (1.14) is usually done using a finite-volume approach,

$$\begin{aligned}\Delta\mathcal{V}^{n+1}_{i,j,k} q^{n+1}_{i,j,k} = \Delta\mathcal{V}^{n}_{i,j,k} q^{n}_{i,j,k} - \Delta t \Big[&\widetilde{q}_{i+\frac{1}{2},j,k} U_{i+\frac{1}{2},j,k} \\ &- \widetilde{q}_{i-\frac{1}{2},j,k} U_{i-\frac{1}{2},j,k} \\ &+ \widetilde{q}_{i,j+\frac{1}{2},k} V_{i,j+\frac{1}{2},k} - \widetilde{q}_{i,j-\frac{1}{2},k} V_{i,j-\frac{1}{2},k} \\ &+ \widetilde{q}_{i,j,k+\frac{1}{2}} W_{i,j,k+\frac{1}{2}} - \widetilde{q}_{i,j,k-\frac{1}{2}} W_{i,j,k-\frac{1}{2}}\Big]\,,\end{aligned} \qquad (1.15)$$

where $q_{i,j,k}$ is understood as a volume-averaged concentration over the grid-box $\Delta\mathcal{V}_{i,j,k}$,

$$q_{i,j,k} = \frac{1}{\Delta\mathcal{V}^{n}_{i,j,k}} \int\limits_{\Delta\mathcal{V}^{n}_{i,j,k}} q \, d\mathcal{V} \, . \tag{1.16}$$

The $\widetilde{q}_{i+\frac{1}{2},j,k}$ (q with one index half-integer) are the interfacial values of tracer concentration. Uppercase[3] $U_{i+\frac{1}{2},j,k}$, $V_{i,j+\frac{1}{2},k}$, and $W_{i,j,k+\frac{1}{2}}$ are volumetric fluxes[4] in the two horizontal and vertical directions. These are defined as velocity components multiplied by the contact area between two adjacent grid boxes,

$$\begin{aligned} U_{i+\frac{1}{2},j,k} &= u_{i+\frac{1}{2},j,k} \Delta z_{i+\frac{1}{2},j,k} \Delta\eta_{i+\frac{1}{2},j} \\ V_{i,j+\frac{1}{2},k} &= v_{i,j+\frac{1}{2},k} \Delta z_{i,j+\frac{1}{2},k} \Delta\xi_{i,j+\frac{1}{2}} \, , \end{aligned} \tag{1.17}$$

where $\Delta z_{i+\frac{1}{2},j,k}$, $\Delta\eta_{i,j+\frac{1}{2}}$, and $\Delta z_{i,j+\frac{1}{2},k}$, $\Delta\xi_{i,j+\frac{1}{2}}$ are vertical and horizontal measures of the corresponding grid-box interfaces ($\Delta\xi, \Delta\eta$ are assumed to be nonuniform because of curvilinear horizontal coordinates). The superscripts $n+1$ and n denote new and old time steps. The time step for the flux variables in (1.16) is not specified yet, but the flux form of (1.16)–(1.16) guarantees exact conservation of the global volume integral of the advected quantity as long as there is no net flux across the boundary.

The discretized continuity equation can be formally obtained from (1.16) by setting $q_{i,j,k} \equiv 1$,

$$\begin{aligned} \Delta\mathcal{V}^{n+1}_{i,j,k} = \Delta\mathcal{V}^{n}_{i,j,k} - \Delta t \cdot \Big[& U_{i+\frac{1}{2},j,k} - U_{i-\frac{1}{2},j,k} \\ & + V_{i,j+\frac{1}{2},k} - V_{i,j-\frac{1}{2},k} + W_{i,j,k+\frac{1}{2}} - W_{i,j,k-\frac{1}{2}} \Big] \, . \end{aligned} \tag{1.18}$$

Once it holds, the conservative form of the discrete tracer equation (1.16) has the property of constancy preservation in addition to the property of global content conservation, mentioned above.

Vertical summation of (1.18) for different k leads to the equation for the free surface,

$$\begin{aligned} \zeta^{n+1}_{i,j} = \zeta^{n}_{i,j} - \frac{\Delta t}{\Delta\mathcal{A}_{i,j}} \Big[& \overline{U}_{i+\frac{1}{2},j} - \overline{U}_{i-\frac{1}{2},j} \\ & + \overline{V}_{i,j+\frac{1}{2}} - \overline{V}_{i,j-\frac{1}{2}} \Big] \, . \end{aligned} \tag{1.19}$$

$\Delta\mathcal{A}_{i,j}$ is the horizontal area of the grid box i,j;

$$\overline{U}_{i+\frac{1}{2},j} = \sum_{k=1}^{N} U_{i+\frac{1}{2},j,k} \;, \quad \overline{V}_{i,j+\frac{1}{2}} = \sum_{k=1}^{N} V_{i,j+\frac{1}{2},j} \, , \tag{1.20}$$

are vertically integrated (barotropic) volume fluxes; and we have used the identity

$$(\zeta_{i,j} + h_{i,j}) \cdot \Delta\mathcal{A}_{i,j} \equiv \sum_{k=1}^{N} \Delta\mathcal{V}_{i,j,k} \;, \tag{1.21}$$

where the bottom topography $h_{i,j}$ is independent of time.

In a hydrostatic model the discrete continuity equation (1.18) is used to compute vertical velocity rather than grid-box volume $\Delta\mathcal{V}^{n+1}_{i,j,k}$. (The latter is entirely controlled by change of ζ via (1.11).) Hence,

$$W_{i,j,\frac{1}{2}} = 0 \, , \qquad \text{at the sea floor, and} \tag{1.22}$$

$$\begin{aligned} W_{i,j,k+\frac{1}{2}} = - \sum_{k'=1}^{k} \Bigg\{ & \frac{\Delta\mathcal{V}^{n+1}_{i,j,k'} - \Delta\mathcal{V}^{n}_{i,j,k'}}{\Delta t} + U_{i+\frac{1}{2},j,k'} \\ & - U_{i-\frac{1}{2},j,k'} + V_{i,j+\frac{1}{2},k'} - V_{i,j-\frac{1}{2},k'} \Bigg\} \\ & \text{for all} \qquad k = 1, 2, ..., N \, , \end{aligned} \tag{1.23}$$

which, in fact, defines the meaning of $W_{i,j,k+\frac{1}{2}}$ as a finite-volume flux across the moving grid-box interface $z_{i,j,k+\frac{1}{2}}$. (Recall that setting $k = N$ in (1.23) and using (1.19)–(1.21) results in

$$W_{i,j,N+\frac{1}{2}} = 0 \, , \tag{1.24}$$

as required by the kinematic boundary condition at the free surface.)

Thus far we have assumed that the time step and time-stepping algorithm for the tracer (1.16) and for ζ (1.19) are the same. This would be possible if the barotropic and baroclinic components of the system were advanced using the same small time step dictated by the stability criterion for the barotropic mode; or if the barotropic mode were treated implicitly and if special care were taken to construct volume fluxes $U_{i+\frac{1}{2},j,k}$, $V_{i,j+\frac{1}{2},k}$, and $W_{i,j,k+\frac{1}{2}}$ so that the (1.18) holds exactly, Dukowitz & Smith, 1994. In a split-explicit, free-surface model, the free-surface equation and the vertically integrated (two-dimensional) momentum equations are stepped forward with a much smaller time step than the tracer equations. Moreover — in order to avoid the errors associated with aliasing of the frequencies resolved by the barotropic time step but not resolved by the baroclinic one — the barotropic fields usually are averaged within the one baroclinic time step, so that its fast signals are suppressed. Usually (*cf.,* Killworth *et al.*, 1991), at every baroclinic time step before the barotropic time stepping is started, the vertically integrated right sides of the momentum equations are computed and used as a forcing function for the barotropic mode. During the barotropic time stepping, the free surface and the barotropic velocity components are averaged

---

[3] We use uppercase letters to denote finite-volume fluxes, while the corresponding lowercase letters are reserved for the velocity components.

[4] We assume that a Boussinesq approximation is made that implies that density is constant and equal to the background density ρ_0 everywhere except in the gravitational force. This implies that mass conservation is equivalent to volume conservation and in the present paper these two terms mass are used interchangeably.

over the sequence of the barotropic steps, and these averaged values are used to feed back in the three-dimensional momentum equations. At first the latter are stepped forward in time for one baroclinic step (thus, with violation of CFL criterion for the external mode) to compute the new fields at time step $n+1$. Immediately after that, the vertical integrals of the newly computed fields are computed and subtracted from similar fields obtained from the barotropic submodel. The resultant difference (*i.e.,* correction) is then uniformly distributed throughout the water column to make sure that the corrected three-dimensional velocity components have the same vertically averaged values as those from the barotropic submodel. At the same time, ζ at the new baroclinic time step $n+1$ is assigned to be the same as the fast-time-step-averaged free surface from the two-dimensional submodel.

Thus, the time-stepping algorithms for the tracer and free-surface equations are very different. In particular, the continuity equation holds exactly only in the sense of its vertical integral and only within the fast-time-stepping procedure. There will be only approximate agreement between left and right sides of (1.19) if the fast-time-averaged free surface and fast-time-averaged barotropic velocity components are substituted for ζ^n, ζ^{n+1}, $\overline{U}$ and $\overline{V}$. Consequently, the integral conservation and/or constancy preservation properties for the tracer equation (1.16) hold only within the order of accuracy of time stepping, but not exactly.

2. Accuracy and Stability of Time-Stepping Algorithms

2.1. Simple Time Stepping

Consider the one-dimensional linear hyperbolic equation,

$$\frac{\partial q}{\partial t} = -c\frac{\partial q}{\partial x}\,, \tag{2.1}$$

and one-dimensional hyperbolic system of equations,

$$\frac{\partial \zeta}{\partial t} = -c\frac{\partial u}{\partial x} \qquad \frac{\partial u}{\partial t} = -c\frac{\partial \zeta}{\partial x}\,, \tag{2.2}$$

where c is phase speed. This is a simple analog for the barotropic mode in the absence of Coriolis force and topography. In the free-surface equation the barotropic mass fluxes are the product of vertically averaged velocities and total depth (which itself depends on ζ; the nonlinear barotropic system (3.48)-(3.49) has a similarity with both (2.1) and (2.2) in the sense that ζ may be advected by the flow, as well as be changed by its divergence [5]. Therefore, our goal is to design an accurate and stable algorithm to advance both (2.1) and (2.2). We focus mostly on achieving the greatest stability for the system (since the waves usually propagate faster than the advection speed), while at the same time minimizing dissipation for the advection equation.

A Fourier transform of (2.1)-(2.2) respectively yields

$$\frac{\partial \hat{q}_k}{\partial t} = -i\omega\cdot\hat{q}_k\,, \tag{2.3}$$

and

$$\frac{\partial \hat{\zeta}_k}{\partial t} = -i\omega\cdot\hat{u}_k \qquad \frac{\partial \hat{u}_k}{\partial t} = -i\omega\cdot\hat{\zeta}_k\,, \tag{2.4}$$

where $\omega \equiv ck$ and, in the continuous case, k is spatial wavenumber. In the case of spatial second-order finite differences on a staggered grid (2.2) becomes

$$\begin{aligned} \frac{\partial \zeta_j}{\partial t} &= -c\cdot\frac{u_{j+\frac{1}{2}} - u_{j-\frac{1}{2}}}{\Delta x} \\ \frac{\partial u_{j+\frac{1}{2}}}{\partial t} &= -c\cdot\frac{\zeta_{j+1}-\zeta_j}{\Delta x}\,, \end{aligned} \tag{2.5}$$

Fourier transform of which has the same form as (2.4), except that k is replaced with

$$\widetilde{k} = \frac{\sin\left(\frac{k\Delta x}{2}\right)}{\frac{\Delta x}{2}} = \begin{cases} k\,, & k\Delta x \ll 1 \\ 2/\Delta x\,, & k=\pi/\Delta x\,, \end{cases} \tag{2.6}$$

which has its maximum value $\widetilde{k}_{\max} = 2/\Delta x$. This means that if a time stepping algorithm for (2.4) has stability limit $\omega\Delta t_{\max}$, it translates into maximum allowed Courant number

$$\left.\frac{c\Delta t}{\Delta x}\right|_{\max} = \frac{1}{2}\omega\Delta t_{\max}\,, \tag{2.7}$$

if the same algorithm is applied to (2.5).

Explicit time-stepping algorithms for single oscillatory equation (2.3) are well studied (see Canuto *et al.*, 1988; Durran, 1991 and Appendix A for a review). The same algorithms can be applied to the system when the right-side terms for both equations of (2.4) are computed at the same time and then added to their respective prognostic variables. This results in the same order of accuracy and stability limit as for the single equation. Let

$$q^{n+1} = \mathcal{F}(q^n, q^{n-1}, \ldots) - i\alpha\cdot\mathcal{G}(q^n, q^{n-1}, \ldots)\,, \tag{2.8}$$

---

[5] A similar duality exists in the baroclinic case, where temperature and salinity fields are advected directly by the flow as well as coupled with the momentum equations via the background stratificationl this results in internal-wave propagation.

where $\alpha = \omega \mathit{\Delta} t$, and

$$\mathcal{F}(q^n, q^{n-1}, ...) = \sum_{m=0}^{r} \beta_m q^{n-m}$$

$$\mathcal{G}(q^n, q^{n-1}, ...) = \sum_{m=0}^{r} \gamma_m q^{n-m}$$

be an explicit time-stepping algorithm for (2.3). Its amplification factors are the roots of the characteristic polynomial,

$$\mathcal{P}(\lambda) = \lambda^{r+1} - \sum_{m=0}^{r} (\beta_m - i\alpha \cdot \gamma_m) \lambda^{r-m} \,. \tag{2.9}$$

Similarly, the same algorithm applied to the system, (2.4),

$$\begin{aligned} \begin{pmatrix} \zeta \\ u \end{pmatrix}^{n+1} &= \mathcal{F}\left[\begin{pmatrix} \zeta \\ u \end{pmatrix}^{n}, \begin{pmatrix} \zeta \\ u \end{pmatrix}^{n-1}, ... \right] \\ &+ \begin{pmatrix} 0 & -i\alpha \\ -i\alpha & 0 \end{pmatrix} \cdot \mathcal{G}\left[\begin{pmatrix} \zeta \\ u \end{pmatrix}^{n}, \begin{pmatrix} \zeta \\ u \end{pmatrix}^{n-1}, ... \right], \end{aligned} \tag{2.10}$$

gives

$$\begin{vmatrix} \mathcal{F}(1, \lambda^{-1}, ...) - \lambda & -i\alpha \cdot \mathcal{G}(1, \lambda^{-1}, ...) \\ -i\alpha \cdot \mathcal{G}(1, \lambda^{-1}, ...) & \mathcal{F}(1, \lambda^{-1}, ...) - \lambda \end{vmatrix} = 0 \tag{2.11}$$

or

$$\begin{aligned} &\left(\mathcal{F}(1, \lambda^{-1}, ...) - \lambda \right)^2 + \alpha^2 \mathcal{G}^2 \left(1, \lambda^{-1}, ... \right) \\ &= \left(\lambda - \sum_{m=0}^{r} (\beta_m - i\alpha \cdot \gamma_m) \lambda^{-m} \right) \\ &\times \left(\lambda - \sum_{m=0}^{r} (\beta_m + i\alpha \cdot \gamma_m) \lambda^{-m} \right) = 0 \,. \end{aligned} \tag{2.12}$$

This obviously has the same set of roots as (2.9) as well as their complex conjugates, since the coefficients β_m and γ_m are real numbers. (2.8) is the most general form that covers both single-step (*e.g.,* Leap-Frog (LF) and Adams-Bashforth (AB2,AB3)) and multistage algorithms (*e.g.,* Runge-Kutta (RK2,RK3, etc) and various predictor-correctors). In the last case β_m and γ_m also depend on α, but they are still real-valued.

Eqs. (2.8)-(2.10) are not the most efficient way to advance the system (2.2), since none of them has an efficiency factor exceeding unity (Appendix A)[6]. In contrast, a simple Forward-Backward (FB) step,

$$\begin{aligned} \zeta^{n+1} &= \zeta^n - i\alpha \cdot u^n \\ u^{n+1} &= u^n - i\alpha \cdot \zeta^{n+1} \end{aligned} \tag{2.13}$$

retains its stability for up to $\alpha = 2$. The FB algorithm may be rewritten in matrix form as

$$\begin{pmatrix} \zeta \\ u \end{pmatrix}^{n+1} = \begin{pmatrix} 1 & -i\alpha \\ -i\alpha & 1 - \alpha^2 \end{pmatrix} \begin{pmatrix} \zeta \\ u \end{pmatrix}^{n}, \tag{2.14}$$

leading to characteristic equation

$$\lambda^2 - (2 - \alpha^2)\lambda + 1 = 0 \,. \tag{2.15}$$

This has roots

$$\lambda_{\pm} = 1 - \frac{\alpha^2}{2} \pm i\alpha \sqrt{1 - \frac{\alpha^2}{4}} \,. \tag{2.16}$$

Obviously $|\lambda_{\pm}| \equiv 1$ as long as the expression under the square root remains positive (*i.e.,* $\alpha \leq 2$). Substitution of the "ideal" value of $\lambda = e^{\pm i\alpha}$ into (2.15) and subsequent expansion in Taylor series for small α results in a mismatch between the left and right sides. To cancel the leading-order term of this mismatch, $\frac{\alpha^3}{24}$, we set $\lambda = e^{\pm i\alpha\left(1 + \frac{1}{24}\alpha^2\right)}$; this indicates that the phase approximation has second-order accuracy. The positions of the roots $\lambda_{\pm}$ on a complex plane are shown in Fig. 2. As predicted, they show a positive dispersion.

The FB algorithm has been successfully used in many models for the barotropic mode (Bleck & Smith, 1990; Killworth *et al.*, 1991; Hallberg, 1997). Its efficiency is explained by the fact that ζ^{n+1} is immediately used in the computation of u^{n+1}, while in (2.10) it is used only during the next time step (or sub-step if a predictor-corrector scheme is used). Compared with LF, FB is twice as efficient, and it does not have computational modes since both roots correspond to physical waves traveling to the left and right. Furthermore, because one needs to suppress the computational modes of LF, the efficiency contrast is even larger.

The major drawback of FB lies in the fact that the forward step is unconditionally unstable for (2.1). In the context of a free-surface model, this implies that unless the actual free-surface equation is linearized,

$$\overline{\mathbf{V}} = (h + \zeta)\overline{\mathbf{v}} \quad \rightarrow \quad \overline{\mathbf{V}} = h\overline{\mathbf{v}}, \tag{2.17}$$

the algorithm is unstable due to the advective features of in the free-surface equation. The linearization is undesirable because it destroys the consistency of the three-dimensional continuity equation and eventually results in loss of conservation or constancy preservation for the tracers. In (2.17) $\overline{\mathbf{V}}$ is the vertically integrated (barotropic) mass flux; $\overline{\mathbf{v}}$ is the vertically averaged velocity; h is topography, and $(h + \zeta)$ is total thickness of water column. A similar difficulty occurs for the Coriolis force, so a special treatment is required (*e.g.,* , an AB3 or implicit time step). Additionally, FB and LF are quite inaccurate in terms of

---

[6] The efficiency factor is defined as maximum allowed Courant number α divided by the number of computations of the right side per time step.

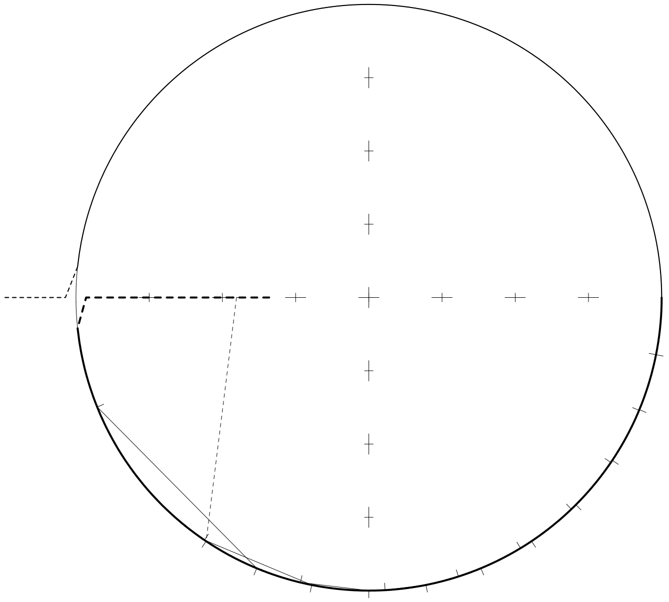

Figure 2. Roots of the characteristic equation for the forward-backward time-stepping scheme. The unit circle is shown for reference. Tickmarks on the outer side of the unit circle show the location of "ideal" amplification factors $e^{-i\alpha}$, where $\alpha = \left\{-\frac{\pi i}{16}, , -\frac{\pi i}{8}, -\frac{3\pi i}{16}, \ldots \text{etc}\right\}$. Tickmarks on the inner side of the unit circle show the location of the actual roots of the characteristic equation. The mismatch between inner and outer tickmarks indicates the phase error.

phase error at the second half of their range of stability, and neither provides any damping for motions it cannot accurately represent. Therefore, we seek to generalize the FB algorithm such that the first sub-step — the update of ζ — is stable if applied to single oscillation equation (2.3). A secondary goal is to improve on the phase error of FB.

2.2. Generalized Predictor-Corrector Algorithm

The simplest predictor-corrector algorithm is the second-order Runge-Kutta (RK2) step modified by introducing terms with coefficients β and ϵ to make the predictor sub-step,

$$\zeta^{n+1,*} = \zeta^n - i\alpha \cdot u^n \tag{2.18}$$

$$u^{n+1,*} = u^n - i\alpha \cdot \Big(\beta\zeta^{n+1,*} + (1-\beta)\zeta^n\Big), \tag{2.19}$$

and the corrector sub-step,

$$\zeta^{n+1} = \zeta^n - \frac{i\alpha}{2} \cdot \Big(u^{n+1,*} + u^n\Big) \tag{2.20}$$

$$u^{n+1} = u^n - \frac{i\alpha}{2} \cdot \Big(\epsilon\zeta^{n+1} + (1-\epsilon)\zeta^{n+1,*} + \zeta^n\Big). \tag{2.21}$$

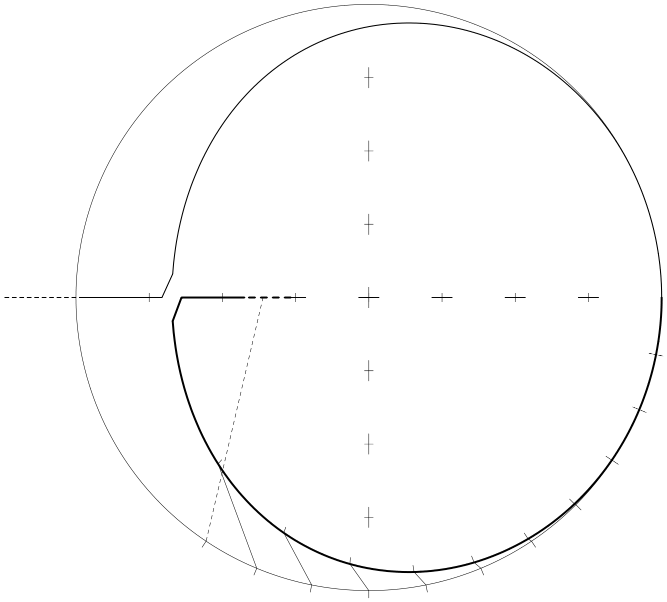

Figure 3. Roots of the characteristic equation for the modified RK2 algorithm with $\beta = 1/3$, $\epsilon = 2/3$, resulting in a stability limit $\alpha_{\max} = 2.14143$.

The case $\beta = \epsilon = 0$ corresponds to the original RK2 that is second-order accurate and is known to have a weak instability for a hyperbolic problem. The presence of the new terms with β and ϵ makes it similar to FB in the sense that, as soon as each prognostic variable is updated, the new values participate immediately in the update of the partner variable (*cf.,* the synchronous time step (2.10) where it happens only during the next step).

The algorithm (2.18)-(2.21) can be rewritten in matrix form as a single step,

$$\begin{pmatrix}\zeta\\ u\end{pmatrix}^{n+1} = \begin{pmatrix} 1-\frac{\alpha^2}{2} & -i\alpha\left(1-\frac{\alpha^2\beta}{2}\right) \\ -i\alpha\left(1-\frac{\alpha^2\epsilon}{4}\right) & 1-\frac{\alpha^2}{2}+\frac{\alpha^4\beta\epsilon}{4}\end{pmatrix}\begin{pmatrix}\zeta\\ u\end{pmatrix}^{n},$$

with the characteristic equation,

$$\begin{aligned}\lambda^2 - \left(2-\alpha^2+\frac{\alpha^4\beta\epsilon}{4}\right)\lambda + 1 \\ +\frac{\alpha^4}{4}\left(1-2\beta-\epsilon+\beta\epsilon\right) = 0\,.\end{aligned} \tag{2.22}$$

After substituting $\lambda = e^{i\alpha}$ and expanding (2.22) in Taylor series for small α, it becomes,

$$\alpha^4\left(\frac{1}{3}-\frac{\beta}{2}-\frac{\epsilon}{4}\right) - \frac{i\alpha^5}{4}\left(1-2\beta-\epsilon-\beta\epsilon\right) = \mathcal{O}\left(\alpha^6\right), \tag{2.23}$$

where setting $\epsilon = \frac{4}{3} - 2\beta$ eliminates the $\mathcal{O}(\alpha^4)$ term, transforming it into

$$-\frac{i\alpha^5}{36}\left[1-2\left(\beta-\frac{1}{3}\right)^2\right]=\mathcal{O}(\alpha^6)\,. \tag{2.24}$$

No choice of real-valued β can eliminate the $\mathcal{O}(\alpha^5)$; however, ($\beta = 1/3$, $\epsilon = 2/3$) minimizes it. This choice also corresponds to the largest possible stability limit, $\alpha_{\max} = 2.14143$. The resultant algorithm is third-order accurate for $\lambda(\alpha)$ with a dissipative, leading-order truncation term. The positions of the roots of the characteristic equation relative to the unit circle are shown in Fig. 3; note the much smaller phase error in comparison with the classical FB. Since this algorithm does not require any knowledge of past time steps, it is a good choice for the starting time step since it cures the usual problem of loss of accuracy associated with a forward Euler step.

Another commonly used algorithm is the Leap-Frog–Trapezoidal Rule (LF-TR) predictor-corrector step. Following the same methodology, we introduce FB-feedback (β- and ϵ-terms) between the equations during both the predictor stage,

$$\zeta^{n+1,*}=\zeta^{n-1}-2i\alpha\cdot u^n \tag{2.25}$$

$$\begin{aligned} u^{n+1,*}=u^{n-1}-2i\alpha\cdot\big[&(1-2\beta)\,\zeta^n \\ &+\beta\left(\zeta^{n+1,*}+\zeta^{n-1}\right)\big]\,, \end{aligned} \tag{2.26}$$

and the corrector stage,

$$\begin{aligned} \zeta^{n+1}=\zeta^n-i\alpha\cdot\Bigg\{&\left(\frac{1}{2}-\gamma\right)u^{n+1,*} \\ &+\left(\frac{1}{2}+2\gamma\right)u^n-\gamma u^{n-1}\Bigg\} \end{aligned} \tag{2.27}$$

$$\begin{aligned} u^{n+1}=u^n-i\alpha\cdot\Bigg\{&\left(\frac{1}{2}-\gamma\right)\Big[\epsilon\zeta^{n+1} \\ +(1-\epsilon)\zeta^{n+1,*}\Big]&+\left(\frac{1}{2}+2\gamma\right)\zeta^n-\gamma\zeta^{n-1}\Bigg\}\,. \end{aligned} \tag{2.28}$$

When $\beta = \epsilon = \gamma = 0$, this is equivalent to the familiar LF-TR algorithm with the stability limit $\alpha_{\max} = \sqrt{2}$. $\beta = \epsilon = 0$ and $\gamma = 1/12$ result in LF-AM3 that is third-order accurate and has the slightly larger stability limit of 1.587 (Appendix A).

The algorithm (2.25)-(2.28) may be rewritten in matrix form,

$$\begin{aligned} \begin{pmatrix}\zeta\\ u\end{pmatrix}^{n+1} &= \begin{pmatrix}A & -iB\\ -iC & D\end{pmatrix}\begin{pmatrix}\zeta\\ u\end{pmatrix}^{n} \\ &+\begin{pmatrix}E & -iF\\ -iG & H\end{pmatrix}\begin{pmatrix}\zeta\\ u\end{pmatrix}^{n-1} \end{aligned} \tag{2.29}$$

with

$$A=1-2\alpha^2\left(\frac{1}{2}-\gamma\right)(1-2\beta)$$

$$B=\alpha\left\{\frac{1}{2}+2\gamma-4\alpha^2\left(\frac{1}{2}-\gamma\right)\beta\right\}$$

$$\begin{aligned} C=\alpha\Bigg\{\frac{1}{2}+2\gamma+\epsilon\left(\frac{1}{2}-\gamma\right)\Bigg[&1-2\alpha^2\left(\frac{1}{2}-\gamma\right) \\ &\times(1-2\beta)\Bigg]\Bigg\} \end{aligned}$$

$$D=1-2\alpha^2\left(\frac{1}{2}-\gamma\right)\left\{1-\epsilon\left[\frac{3}{4}-\gamma+2\alpha^2\left(\frac{1}{2}-\gamma\right)\beta\right]\right\}$$

$$E=-4\alpha^2\left(\frac{1}{2}-\gamma\right)\beta \qquad F=\alpha\left(\frac{1}{2}-2\gamma\right)$$

$$H=-\alpha^2\left(\frac{1}{2}-\gamma\right)\left(\frac{1}{2}-2\gamma\right)\epsilon$$

$$G=\alpha\left\{\frac{1}{2}-2\gamma-\epsilon\left(\frac{1}{2}-\gamma\right)\left[1+4\alpha^2\left(\frac{1}{2}-\gamma\right)\beta\right]\right\}\,.$$

This leads to the characteristic equation,

$$\begin{aligned} \lambda^2-(A+D)\lambda+AD+BC-H-E& \\ +(AH+ED+BG+FC)\lambda^{-1}& \\ +(EH+FG)\lambda^{-2}=0\,.& \end{aligned} \tag{2.30}$$

Substitution of all coefficients $A, B, ..., H$ into (2.30) along with $\lambda = e^{i\alpha}$, and subsequent Taylor series expansion for powers of α yields,

$$\begin{aligned} -\alpha^4\left(\frac{1}{6}-2\gamma\right)+i\alpha^5\Bigg[&\frac{1}{3}-2\gamma+4\gamma^2-(1-2\gamma)\beta \\ -\left(\frac{1}{4}-\frac{3}{2}\gamma+2\gamma^2\right)\epsilon\Bigg]&+\alpha^6\Bigg[\frac{133}{720}-\frac{3}{2}\gamma+\frac{7}{3}\gamma^2 \\ &-\frac{\epsilon}{24}\left(5-26\gamma+32\gamma^2\right)-\beta(1-2\gamma) \\ &\times\left(\frac{2}{3}-\epsilon(1-2\gamma)\right)\Bigg]+\mathcal{O}\left(\alpha^7\right)=0\,. \end{aligned} \tag{2.31}$$

This indicates that setting $\gamma = 1/12$ ensures third-order accuracy, regardless of the settings of β and ϵ.

Once the choice of $\gamma = 1/12$ is made, β and ϵ must satisfy

$$\beta=\frac{7}{30}-\frac{\epsilon}{6} \tag{2.32}$$

in order to eliminate $\mathcal{O}(\alpha^5)$ term in (2.31), and

$$\frac{41}{15}-\frac{55}{12}\epsilon-5\beta(4-5\epsilon)=0 \tag{2.33}$$

to eliminate $\mathcal{O}(\alpha^6)$. Substitution of β from (2.32) into (2.33) leads to a quadratic equation for ϵ which does not have a real-valued solution. One can only minimize the error in (2.33) by choosing $\epsilon = 11/20$ and correspondingly $\beta = 17/120$ to satisfy (2.32). This results in fourth-order accuracy with the minimum possible truncation error

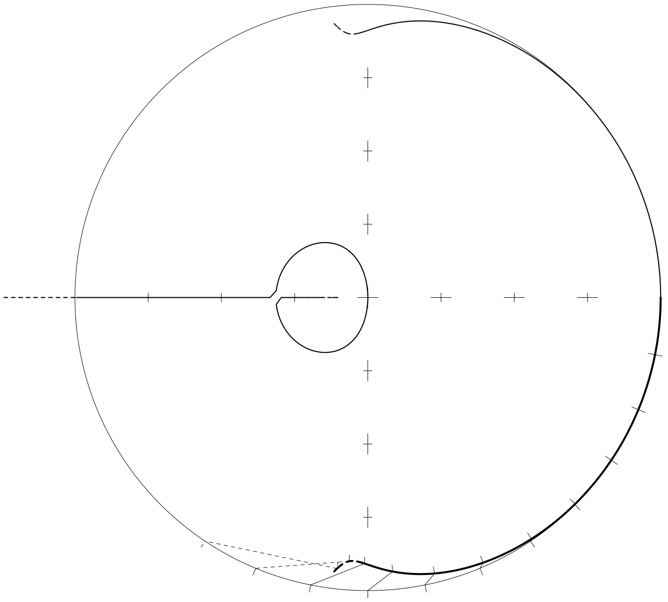

Figure 4. Roots of the characteristic equation for the modified LF-AM3 algorithm with $\gamma = 1/12$, $\beta = 17/120$, $\epsilon = 11/20$. This choice corresponds to the minimum truncation error in terms of a Taylor-series analysis among all possible settings of γ, β, ϵ. It has a stability limit $\alpha_{\max} = 1.853$.

(among all possible β, γ, and ϵ) and in the stability limit, $\alpha_{\max} = 1.853$ (Fig. 4).

We next seek an algorithm with minimum phase error while trying to achieve the best possible stability limit. To do so, we keep $\gamma = 1/12$, but instead of determining β and ϵ from (2.32)-(2.33), we arbitrarily pick β within the range of values from 0.0 - 0.15, and then for each β we choose ϵ to eliminate the phase error at $\alpha = \pi/2$ and determine the stability limit, $\alpha_{\max}$:

β	ϵ	$\alpha_{\max}$
0.00	0.97	1.6076
0.01	0.96	1.6352
0.02	0.94	1.6659
0.03	0.92	1.6965
0.04	0.90	1.7241
0.05	0.86	1.7548
0.06	0.82	1.7855
0.07	0.77	1.8100

β	ϵ	$\alpha_{\max}$
0.08	0.72	1.8315
0.09	0.66	1.8438
0.10	0.60	1.8469
0.11	0.53	1.8285
0.12	0.45	1.7916
0.13	0.35	1.7303
0.14	0.23	1.6474
0.15	0.00	1.4971

The choice ($\beta = 0.1$, $\epsilon = 0.60$) corresponds to a two-dimensional optimum for $\alpha_{\max}$, subject to zero phase error at $\alpha = \pi/2$. Roots of its characteristic equation are shown in the top-left panel of Fig. 5. In addition to its small phase error, it also has remarkably small dissipation within the range of $0 < \alpha < \pi/4$, although it is slightly more dissipative than in Fig. 4. This is clearly a desirable algorithm if an accurate representation of wave-like processes is desired. In comparison with the original LF-AM3 (Appendix A), it has a greater stability limit by approx. 16%, and it does not show the phase-lead error of LF-AM3. Since the right-side terms have to be computed twice per time step, this algorithm is approximately twice less efficient in comparison with FB.

Thus far we have explored the possibility to achieve the best possible accuracy. For the barotropic mode stepping in a split-explicit model, the design goals are different: the phase error is of lesser priority, but it is desirable that the algorithm have a large stability limit and be dissipative for high frequencies. Giving up third-order accuracy allows γ to be a free parameter and makes it possible to achieve much greater stability limit. In the table following, for each γ we choose β and ϵ such that they produce the largest $\alpha_{\max}$:

γ	β	ϵ	$\alpha_{\max}$
0.04	0.155	0.93	2.1046
0.03	0.156	0.90	2.1230
0.02	0.161	0.88	2.1874
0.01	0.161	0.87	2.2518
0	0.166	0.83	2.4420
−0.01	0.152	0.84	2.5065
−0.02	0.137	0.84	2.5678
−0.025	0.130	0.84	2.6077
−0.03	0.124	0.84	2.6445
−0.04	0.113	0.84	2.7304
−0.05	0.105	0.84	2.8010
−0.055	0.106	0.84	2.7765*

The three remaining panels in Fig. 5 show examples of algorithms from this sequence. When γ decreases and then becomes negative, the arms corresponding to the physical mode contract, allowing a larger stability limit; at the same time, the roots corresponding to the computational mode became closer to the unit circle, and finally touch it at $\gamma = -0.055$. Although this shows the possibility of a dramatic increase of $\alpha_{\max}$ up to 2.8, algorithms with negative γ do not behave well in practice because of poor damping of the computational mode. This leads to a compromise choice of $\gamma = 0$, resulting in $\alpha_{\max} = 2.44$ that is still 70% more efficient than the standard LF-TR.

As the final remark we note that predictor-corrector algorithm (2.25)–(2.28) may be reformulated as

$$\zeta^{n+\frac{1}{2}} = \left(\frac{1}{2} - 2\gamma\right)\zeta^{n-1} + \left(\frac{1}{2} + 2\gamma\right)\zeta^{n} \qquad (2.34)$$

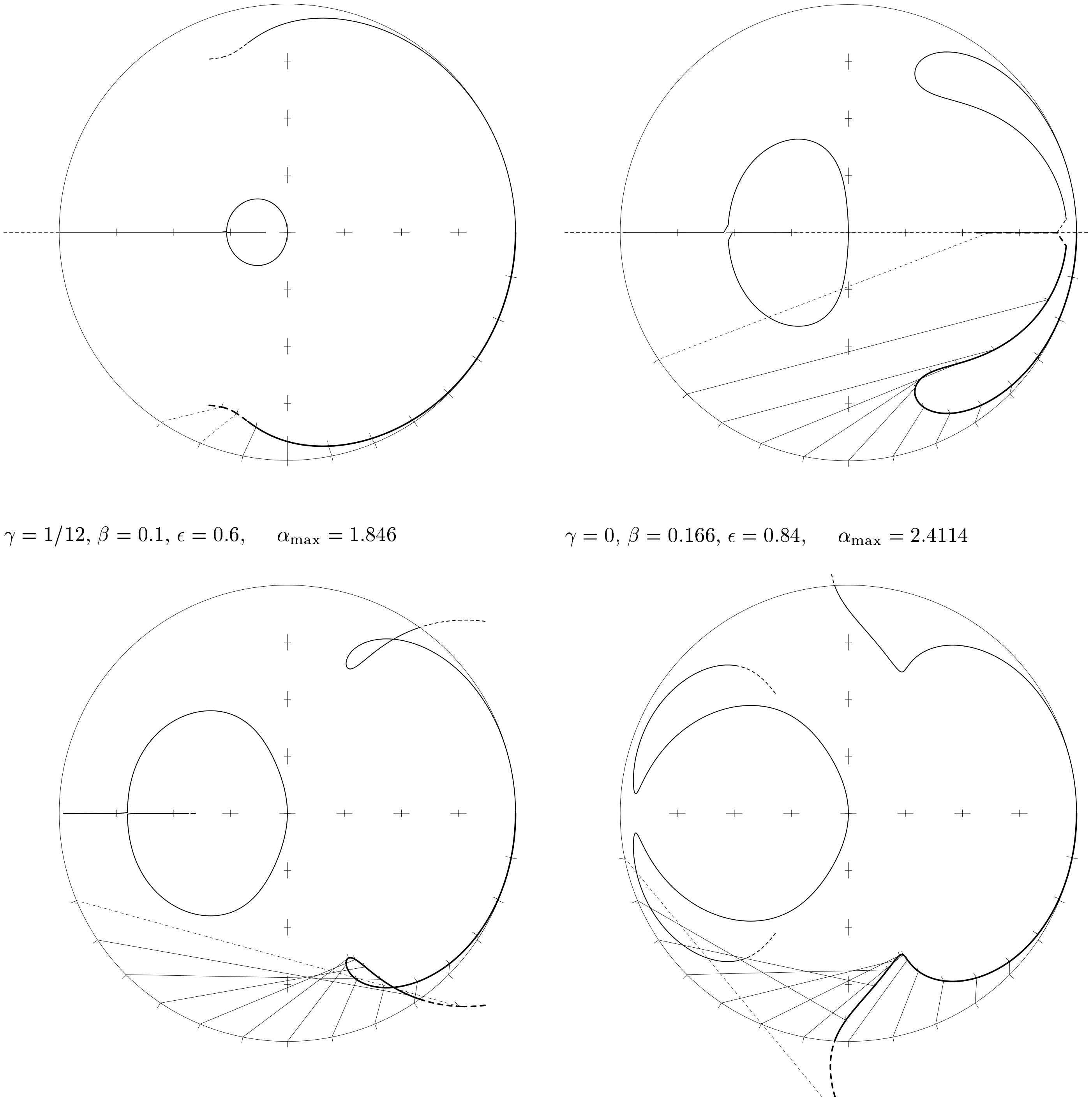

$\gamma = 1/12$, $\beta = 0.1$, $\epsilon = 0.6$, $\alpha_{\max} = 1.846$

$\gamma = 0$, $\beta = 0.166$, $\epsilon = 0.84$, $\alpha_{\max} = 2.4114$

$\gamma = -0.025$, $\beta = 0.130$, $\epsilon = 0.84$, $\alpha_{\max} = 2.6078$

$\gamma = -0.05$, $\beta = 0.105$, $\epsilon = 0.84$, $\alpha_{\max} = 2.8010$

Figure 5. Complex roots and stability limits $\alpha_{\max}$ for the generalized predictor-corrector algorithm with four different parameter sets for γ, β, and ϵ. Top-left: Algorithm optimized for the maximum stability, under the constraint of retaining third-order accuracy (thus γ=1/12) and minimal phase error. Since right sides for both equations have to be computed twice, it is more than twice less efficient than FB. This algorithm is remarkably accurate within the whole its range of stability. In the remaining three panels, the two remaining coefficients, β and ϵ, are optimized to achieve the largest possible stability range (for given values of γ=0; -0.025 and -0.05).

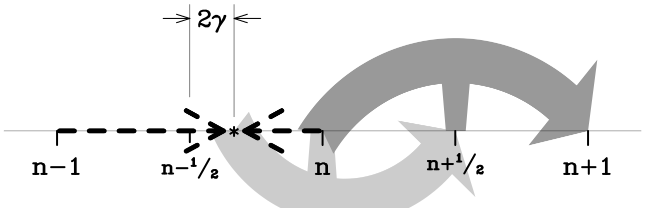

Figure 6. Geometrical interpleration of reformulated LF-AM3 predictor-corrector step (2.34)–(2.37) with $\beta = \epsilon = 0$: initial data at $n-1$ and n is linearly interpolated to $n - \frac{1}{2} + 2\gamma$ (bold dashed arrows) and advanced to $n + \frac{1}{2}$ using r.h.s. at n (light gray curved arrow, predictor). The resultant values participate only in computation of r.h.s. at $n + \frac{1}{2}$ to advance prognostic variables from n to $n+1$ (dark gray arrow, corrector), and does not need to be stored between time steps.

$$-i\alpha\left(1-2\gamma\right)u^{n}$$

$$u^{n+\frac{1}{2}} = \left(\frac{1}{2} - 2\gamma\right)u^{n-1} + \left(\frac{1}{2} + 2\gamma\right)u^{n} \tag{2.35}$$
$$-i\alpha\left(1-2\gamma\right)\left[\zeta^{n} + \beta\frac{2\zeta^{n+\frac{1}{2}} - 3\zeta^{n} + \zeta^{n-1}}{1-2\gamma}\right],$$

followed by

$$\zeta^{n+1} = \zeta^{n} - i\alpha u^{n+\frac{1}{2}} \tag{2.36}$$

$$u^{n+1} = u^{n} - i\alpha\left\{\left(1-\epsilon\right)\zeta^{n+\frac{1}{2}} + \epsilon\left[\left(\frac{1}{2} - \gamma\right)\zeta^{n+1} + \left(\frac{1}{2} + 2\gamma\right)\zeta^{n} - \gamma\zeta^{n-1}\right]\right\}, \tag{2.37}$$

after which the provisional values $\zeta^{n+\frac{1}{2}}$ and $u^{n+\frac{1}{2}}$ are discarded. Despite its rather sophisticated appearance, this algorithm can be interpreted and a combination of linear interpolation and two LF-like steps, Fig. 6, which results in a very efficient code: in comparison with its prototype, the new algorithm eliminates the need to store time tendencies for the prognostic variables from one time step to the next. Later it will also be shown that (2.34)—(2.37) is a more suitable prototype for a nonlinear system, than the original (2.25)–(2.28).

2.3. Generalized Forward-Backward Algorithm

We first consider the AB2 algorithm for the first substep. Although it is known to be asymptotically unstable for the advection equation, the instability is relatively weak, and it is instructive to begin the search with this algorithm. The modified FB algorithm now becomes

$$\zeta^{n+1} = \zeta^{n} - i\alpha\left(\frac{3}{2}u^{n} - \frac{1}{2}u^{n-1}\right) \tag{2.38}$$

$$u^{n+1} = u^{n} - i\alpha\left[\delta\zeta^{n+1} + \left(1-\delta-\gamma\right)\zeta^{n} + \gamma\zeta^{n-1}\right],$$

where δ and γ are to be determined. The corresponding characteristic equation is

$$\lambda^{2} - \left(2 - \frac{3}{2}\delta\alpha^{2}\right)\lambda + 1 + \left(\frac{3}{2} - 2\delta - \frac{3}{2}\gamma\right)\alpha^{2} \tag{2.39}$$
$$- \left(\frac{1}{2} - \frac{1}{2}\delta - 2\gamma\right)\alpha^{2}\lambda^{-1} - \frac{1}{2}\alpha^{2}\lambda^{-2} = 0\,.$$

We must choose δ and γ is such a way that the algorithm is consistent with the continuous equations. To do so, we substitute $\lambda = e^{i\alpha}$ into (2.39) and Taylor expand for small α, collecting coefficients with the same powers of α:

$$\left(\delta - \gamma - \frac{1}{2}\right)i\alpha^{3} + \left(\frac{1}{3} - \frac{1}{2}\delta + 2\gamma\right)\alpha^{4} + \mathcal{O}\left(\alpha^{5}\right) = 0 \tag{2.40}$$

The choice of ($\gamma = -1/30$, $\delta = 7/15$) eliminates both leading-order terms in (2.40), resulting in a third-order accurate scheme that is asymptotically unstable. To make a stable algorithm, one needs to give up one order of accuracy and treat γ as an adjustable parameter, while δ is chosen from $\delta = \frac{1}{2} + \gamma$. The choice of $\gamma = +0.279$ corresponds to the maximum possible stability range for an algorithm of this kind, $\alpha_{\max} = 1.343$, limited by the instability of one of computational modes (Fig. 7; the roots corresponding to the computational modes are real valued. Note the horizontal thin line crossing the unit circle in the negative direction on the real axis). Unlike the classical FB, the new algorithm produces a remarkably small phase error that is practically invisible for $\alpha < \pi/4$, despite the fact that it is only second-order accurate (the same as FB). However, this algorithm has a weak instability of the physical modes: the corresponding roots are slightly outside the unit circle, which is too small to be visible in Fig. 7 since $1 < |\lambda_{\rm phys}| < 1.01$ in the vicinity of $\frac{\pi}{16} < \alpha < \frac{\pi}{4}$. This instability disappears if $\lambda \geq 1/2$, but at the expense of reducing the stability limit to $\alpha_{\max} = 16/17$ and increasing the phase error.

The next possibility is to use an AB3-like time step for the ζ equation,

$$\zeta^{n+1} = \zeta^{n} - i\alpha\Big[\left(\frac{3}{2} + \beta\right)u^{n} - \left(\frac{1}{2} + 2\beta\right)u^{n-1} + \beta u^{n-2}\Big] \tag{2.41}$$
$$u^{n+1} = u^{n} - i\alpha\Big[\delta\zeta^{n+1} + (1-\delta-\gamma-\epsilon)\zeta^{n} + \gamma\zeta^{n-1} + \epsilon\zeta^{n-2}\Big].$$

Setting $\beta = 5/12$ corresponds to an AB3 time step. We will show that this choice is not optimal for the widest stability range; so for now, β is viewed as an adjustable parameter.

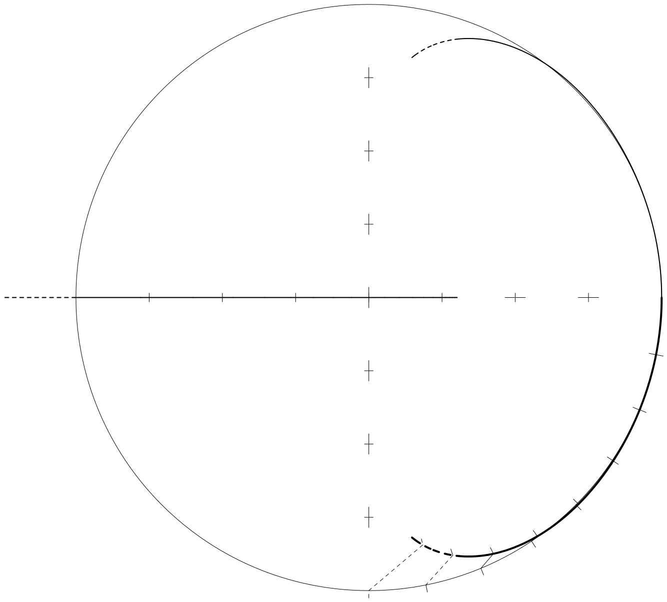

Figure 7. Complex roots of the algorithm consisting of an AB2 step for ζ and a ($\gamma = +0.279$, $\delta = \frac{1}{2} + \gamma$) step for u, resulting in a stability range $\alpha_{\max} = 1.343$ limited by the computational mode leaving the unit circle in negative direction along the real axis. This algorithm is asymptotically unstable, as manifested by the physical modes going slightly outside the unit circle in the vicinity of $\alpha = \pm\pi/4$.

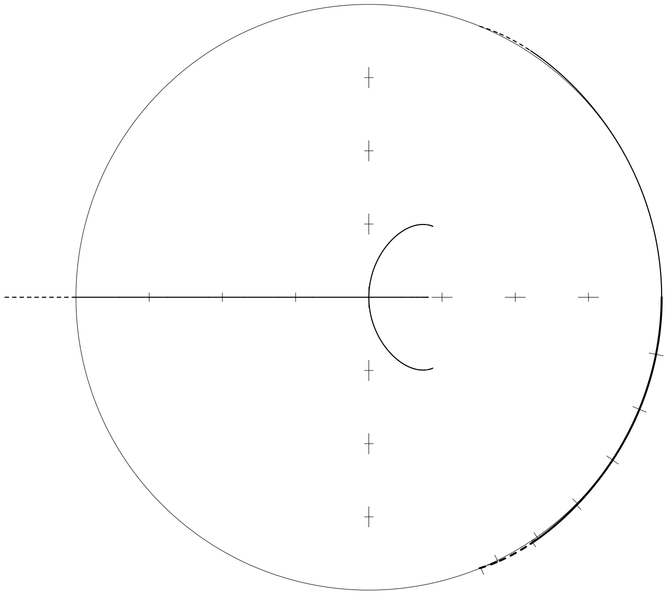

Figure 8. Roots of generalized FB algorithm optimized to achieve the largest possible order of accuracy. It has asymptotic instability of physical modes, (reaching $|\lambda| = 1.014$ at $\alpha \approx 1$), and $\alpha_{\max} = 1.01$ limited by the computational mode leaving the unit circle at $\lambda = -1$.

Algorithm (2.41) has the characteristic equation,

$$\begin{aligned} \lambda^2 - \left[2 - \alpha^2\left(\frac{3}{2} + \beta\right)\delta\right]\lambda + 1 - \alpha^2\Big[-\frac{3}{2} + 2\delta \\ +\frac{3}{2}\gamma + \frac{3}{2}\epsilon - \beta\big(1 - 3\delta - \gamma - \epsilon\big)\Big] \quad (2.42) \\ -\alpha^2\left[\frac{1}{2} - \frac{1}{2}\delta - 2\gamma + \beta\big(2 - 3\delta - 3\gamma - 2\epsilon\big)\right]\lambda^{-1} \\ +\alpha^2\left[\frac{1}{2}\gamma + \frac{3}{2}\epsilon + \beta\big(1 - \delta - 3\gamma\big)\right]\lambda^{-2} \\ +\alpha^2\left[\beta\big(\gamma - 2\epsilon\big) - \frac{1}{2}\epsilon\right]\lambda^{-3} + \alpha^2\beta\epsilon\lambda^{-4} = 0\,. \end{aligned}$$

Similarly to (2.40), we set $\lambda = e^{i\alpha}$ and expand (2.42) in a Taylor series,

$$\begin{aligned} -i\alpha^3\left[\frac{1}{2} - \delta + \gamma + 2\epsilon\right] + \alpha^4\left[\frac{5}{6} - \beta - \delta - \epsilon\right] \\ +\frac{1}{6}i\alpha^5\left[1 - \delta - 2\gamma - \epsilon + 6\beta\big(1 - \delta + \gamma + 2\epsilon\big)\right] \quad (2.43) \\ +\frac{1}{720}\alpha^6\Big[-77 + 60\delta - 180\gamma - 480\epsilon \\ +60\beta\big(7 - 6\delta + 18\gamma + 48\epsilon\big)\Big] + \mathcal{O}\left(\alpha^7\right) = 0\,. \end{aligned}$$

All terms of orders $\mathcal{O}(1)$, $\mathcal{O}(i\alpha)$ and $\mathcal{O}(\alpha^2)$ cancel out for any choice of the coefficients β, γ, δ, and ϵ. To guarantee at least second-order accuracy, we must eliminate $\mathcal{O}(\alpha^3)$ terms in (2.43) by chosing

$$\delta = \frac{1}{2} + \gamma + 2\epsilon\,. \qquad (2.44)$$

This effectively centers the right-side terms in the second equation of (2.41) at $n + 1/2$. It also simplifies (2.43) that now becomes

$$\begin{aligned} \alpha^4\left[\frac{1}{3} - \beta - \gamma - 3\epsilon\right] + \frac{1}{2}i\alpha^5\left[\frac{1}{6} + \beta - \gamma - \epsilon\right] \\ +\alpha^6\left[-\frac{47}{720} - \frac{1}{6}\gamma - \frac{1}{2}\epsilon + \beta\left(\frac{1}{3} + \gamma + 3\epsilon\right)\right] \quad (2.45) \\ +\mathcal{O}(\alpha^7) = 0\,. \end{aligned}$$

First we investigate an algorithm with the largest possible order of accuracy. To eliminate both $\mathcal{O}(\alpha^4)$ and $\mathcal{O}\left(\alpha^5\right)$ terms in (2.45), we need to satisfy

$$\gamma = \frac{1}{4} - 2\epsilon \quad \text{and} \quad \beta = \frac{1}{12} - \epsilon \qquad (2.46)$$

which automatically sets $\delta = 3/4$ for any ϵ. In principle ϵ can be chosen from the condition of cancellation of $\mathcal{O}(\alpha^6)$ terms in (2.45), which, after substitution of (2.46),

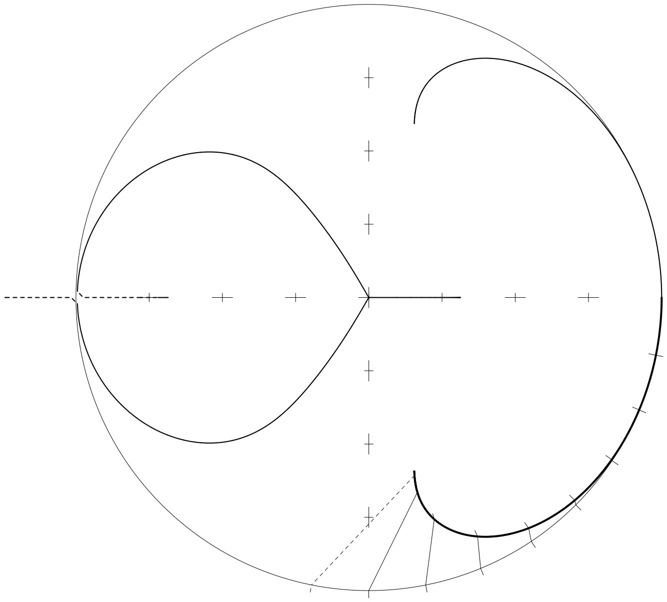

Figure 9. $\epsilon = 0.083$, $\alpha_{\max} = 1.727$. This is the largest possible stability range formally maintaining fourth-order accuracy. The computational modes "touch" the unit circle at the place where they meet at $\lambda = -1$.

becomes

$$-\alpha^6\left[\frac{7}{120}+\frac{2}{3}\epsilon+\epsilon^2\right]+\mathcal{O}\left(\alpha^7\right)=0\,. \tag{2.47}$$

Its roots are

$$\epsilon = -\frac{1}{3}\pm\frac{\sqrt{190}}{60}\,. \tag{2.48}$$

As expected, the resultant algorithm has extremely small phase and amplitude errors (Fig. 8, where we have chosen the "+" sign in (2.48) since the "-" sign results in a much smaller stability limit). But it is not attractive overall because of its modest stability limit of $\alpha_{\max} \approx 1$ and its asymptotic instability for the physical modes. Here it should be noted that unlike for the quartic equation (2.39), there is no general analytical method of finding roots of a fifth- or sixth-order polynomial. However, the roots of (2.42) corresponding to physical modes are always isolated and can be found using an iterative Newton method. Once two physical roots are known, the power of the polynomial is reduced by two, and the remaining roots are found using conventional Cardano or Ferrari solutions.

Abandoning the cancellation of $\mathcal{O}\left(\alpha^6\right)$ terms while retaining both conditions in (2.46) yields asymptotically stable algorithms, as long as $\epsilon > -0.03655$ (corresponding to $\alpha_{\max} = 1.187$). A further increase of ϵ results in an increase of the stability range until it reaches its maximum at $\alpha_{\max} = 1.727$ when $\epsilon = 0.083$; at this point the computational mode touches the unit circle (Fig. 9). This algorithm formally maintains fourth-order accuracy since it eliminates both $\mathcal{O}\left(\alpha^4\right)$ and $\mathcal{O}\left(\alpha^5\right)$ terms in (2.45).

Further relaxing the order of accuracy by abandoning the cancellation of $\mathcal{O}\left(\alpha^5\right)$ terms makes two parameters available for tuning while formally maintaining third-order accuracy. Thus we choose

$$\gamma = \frac{1}{3}-\beta-3\epsilon\,, \tag{2.49}$$

and treat β and ϵ as adjustable parameters.

An obvious choice of ($\epsilon = 0$, $\beta = 5/12$) results in $\gamma = -1/12$ and $\delta = 5/12$ that can be identified as the AB3 coefficients for ζ and AM3 coefficients for u. This has third-order accuracy for each equation in (2.41) taken separately. Its stability limit is $\alpha_{\max} = 1.0039$, with the instability of the physical mode occurring first (Fig. 10, top left).

In this procedure we select β first, then for each beta we choose an ϵ to provide desirable properties of the resultant algorithm. The meaningful range for β is

$$\frac{1}{6}\le\beta\le\frac{5}{12}\,, \tag{2.50}$$

with $\beta = 0$ correspond to AB2 and $\beta = 5/12$ to AB3 time steps for the ζ equation. Because of the advective properties of the nonlinear free-surface and tracer equations, it is also undesirable to choose $\beta < 1/6$ because of the weak instability of AB2 (Appendix A). Setting $\beta = 0.281105$ corresponds to the best stability range for the whole AB2–AB3 family.

A two-parameter optimization for the maximum stability range on the β-ϵ plane results in ($\beta = 0.232$, $\epsilon = 0.00525$) and $\alpha_{\max} = 1.939$ (Fig. 10, top right). This is only insignificantly smaller than for the classical FB algorithm (2.13), but the order of accuracy is now raised to the third and phase lead of FB is eliminated for small values of α. Still, the new algorithm has the same drawback as the classical FB: the second half of its stability range (approx. $\alpha > \pi/3$) is too inaccurate (phase error) and does not provide sufficient damping (roots for physical modes touch the unit circle at $\alpha \approx \pm 2\pi/3$). A slightly modified choice of ($\beta = 0.21$, $\epsilon = 0.0115$) corrects the problem at the expense of a minor reduction of the stability range, $\alpha_{\max} = 1.875$ while maintaining third order accuracy (Fig. 10, bottom left).

It may be advantageous to choose $\beta = 0.281105$ (the largest posiible stability limit among all AB2-AB3 family algorithms for single equation, Appendix A) which leads to a simplification of the algorithm, because separate coefficients for the advection terms in the nonlinear free-surface

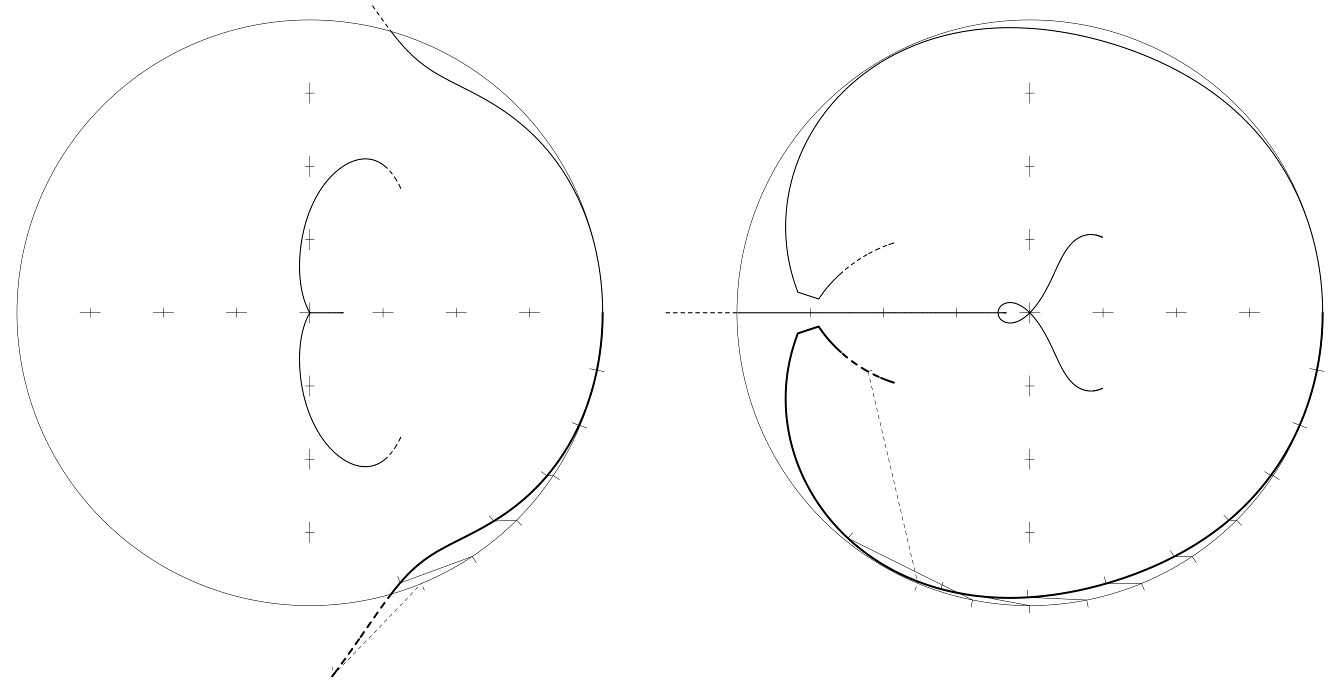

AB3–AM3: $\beta = \frac{5}{12}$, $\gamma = -\frac{1}{12}$, $\epsilon = 0$, $\alpha_{\mathrm{max}} = 1.0038$. $\beta = 0.232$, $\epsilon = 0.00525$, $\gamma = \frac{1}{3} - \beta - 3\epsilon$, $\alpha_{\mathrm{max}} = 1.939$.

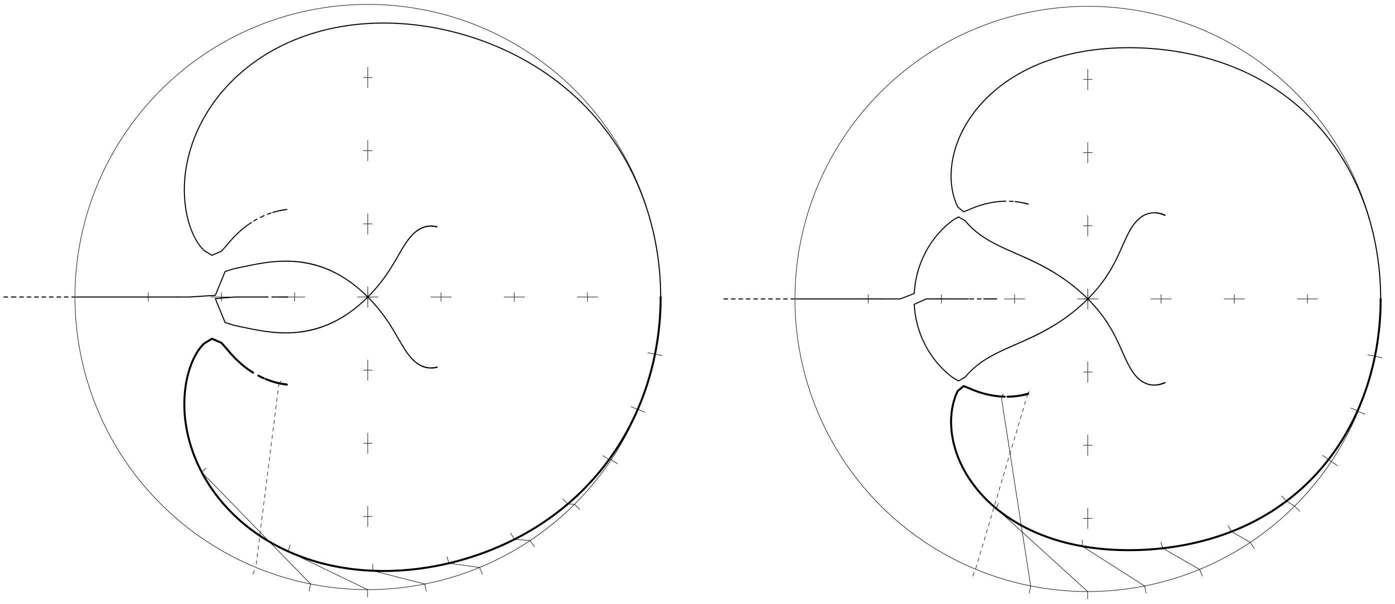

$\beta = 0.21$, $\epsilon = 0.0115$, $\gamma = \frac{1}{3} - \beta - 3\epsilon$, $\alpha_{\mathrm{max}} = 1.875$ $\beta = 0.281105$, $\epsilon = 0.013$, $\gamma = 0.0880$, $\alpha_{\mathrm{max}} = 1.7802$.

Figure 10. Complex roots for generalized AB3-AM3 time-stepping algorithms corresponding to different choices of parameters. Although this choice no longer has formal third-order accuracy of the AM3 time step for ζ, it is effectively more accurate than the one on the left, and it still has third-order asymptotic accuracy for the wave phase speed.

and tracer equations and for the pressure gradient in the momentum equations can be avoided. However, it is then no longer possible to maintain (2.49) and achieve a stability range comparable to 1.8, as in the two previous algorithms. A compromise choice of ($\beta = 0.281105$, $\gamma = 0.088$, $\epsilon = 0.013$) results in a slightly more dissipative algorithm (Fig. 10, bottom right). Since in a split-explicit model the fastest gravity waves are filtered out anyway, this is the algorithm of choice for the barotropic mode.

3. Barotropic Mode Time Stepping

In this section we address specific aspects of the barotropic mode as part of a coupled barotropic-baroclinic system.

3.1. Barotropic Mode for a Stratified Ocean

In a split-explicit method à la Blumberg & Mellor, 1987 and Killworth *et al.*, 1991, after the vertical integration of 3D momentum equations is performed, the Shallow Water Equation (SWE) pressure gradient (computed using the same free surface ζ and a constant reference density ρ_0) is added and subtracted to it, resulting in

$$\frac{\partial \overline{U}}{\partial t} + ... = -gD\nabla_x\zeta + \Big\{ gD\nabla_x\zeta + \mathcal{F} \Big\} \,. \qquad (3.1)$$

g is acceleration of gravity; $D = h + \zeta$ is total depth; $\overline{U} \equiv D\overline{u}$ is depth-integrated velocity (barotropic mass flux); $\nabla_x\zeta$ is a shorthand for $\partial\zeta/\partial x$; and

$$\mathcal{F} = -\frac{1}{\rho_0}\int_{-h}^{\zeta} \frac{\partial P}{\partial x} dz \qquad (3.2)$$

is the vertically integrated pressure gradient. The latter is a functional of the topography, free-surface gradient, and free surface itself, as well as the vertical distribution of density and its gradient,

$$\mathcal{F} = \mathcal{F}\left[\nabla_x\zeta,\ \zeta,\ \nabla_x\rho(z),\ \rho(z)\right] . \qquad (3.3)$$

The term in curly brackets in (3.1) is interpreted as barotropic-baroclinic mode coupling. It is kept "frozen" during the barotropic time stepping while the first term on the right side — the SWE-like term — is evolving in barotropic time.

The disadvantage of this approach is that after the barotropic time stepping is complete and the new free-surface field is substituted into the full baroclinic pressure gradient, its vertical integral will no longer be equal to the sum of the SWE-like pressure gradient (computed using new free surface) and the original coupling term (still based on the old free surface),

$$-gD\nabla_x\zeta' + \Big\{ gD\nabla_x\zeta + \mathcal{F}\left[\nabla_x\zeta,\ \zeta,\ \nabla_x\rho(z),\ \rho(z)\right]\Big\} \qquad (3.4)$$
$$\neq \mathcal{F}\left[\nabla_x\zeta',\ \zeta',\ \nabla_x\rho(z),\ \rho(z)\right] .$$

ζ' is the free-surface elevation after the sequence of barotropic time steps corresponding to one baroclinic time step. This type of discrepancy is usually known as a *mode-splitting* error.

The common argument for the use of (3.1) is based on the fact that the difference is usually very small (since model density $\rho(x,y,z) = \rho_0 + \rho'(x,y,z)$ is always close to ρ_0). However, the primary concern here is that it affects the stability of the split-explicit model. The error (3.4) is discovered during the next baroclinic time step, and it plays the role of a disturbance causing the vertically integrated pressure gradient to be not in equilibrium with the barotropic mass flux. The barotropic time stepping drives the barotropic part toward an equilibrium, but it is disturbed again due to the redefinition of the vertically integrated baroclinic pressure gradient.

Higdon & Bennett, 1996; and later Higdon & de Szoeke, 1997 analyze the stability of a coupled linearized system in an isopycnic vertical coordinate and show that, if non-dissipative time stepping algorithms (LF or FB) are used for both modes, the resultant model is unavoidably unstable[7]. As a remedy they proposed an alternative definition of the barotropic mode in an isopycnic model that eliminates the mode splitting error, resulting in an effectively uncoupled barotropic mode.

One may replace the SWE-like term, $-gD\nabla_x\zeta$, in (3.1) with

$$\frac{\partial\mathcal{F}}{\partial\left(\nabla_x\zeta\right)}\nabla_x\zeta + \frac{\partial\mathcal{F}}{\partial\zeta}\zeta \,, \qquad (3.5)$$

where, for the purpose of partial differentiation, ζ and $\nabla_x\zeta$ are treated as independent variables. After this replacement, (3.4) becomes

$$\mathcal{F}\left[\nabla_x\zeta,\ \zeta,\ ...\right] + \frac{\partial\mathcal{F}}{\partial\left(\nabla_x\zeta\right)}\nabla_x\left(\zeta'-\zeta\right) + \frac{\partial\mathcal{F}}{\partial\zeta}\left(\zeta'-\zeta\right) \qquad (3.6)$$
$$\approx \mathcal{F}\left[\nabla_x\zeta',\ \zeta',\ ...\right] .$$

This removes the dominant portion of the splitting error, and it also implies linearization with respect to ζ.

---

[7] This is evident from Fig. 3.1 from Higdon & de Szoeke, 1997 and the associated discussion. In the case where the roots corresponding to the barotropic mode receive a phase increment during one baroclinic time step equal to the baroclinic roots + an integer times 2π, the barotropic mode is aliased to be in phase with baroclinic mode. So any 2-way coupling between the modes (*i.e.,* a perturbation due to the mode-splitting error) causes at least one root from each pair to go outside the unit circle.

We now show that without significant increase of the computational cost, one can take into account the non-uniform density field in the barotropic mode, resulting in a more accurate mode splitting method that is free of the shortcoming pointed above and is suitable for the use in a terrain-following model. Consider a fluid element bounded horizontally by two vertical lines corresponding to the locations of ζ_i and ζ_{i+1} and vertically by the free surface and bottom. The horizontal component of the pressure-gradient force acting on this element is calculated by the integration of the pressure along the contour surrounding the fluid element (*cf.,* Lin, 1997):

$$\begin{aligned} F_{i+\frac{1}{2}} = & \int_{-h_i}^{\zeta_i} P(x_i,z)\,dz - \int_{-h_{i+1}}^{\zeta_{i+1}} P(x_{i+1},z)\,dz \\ & - \int_{x_i}^{x_{i+1}} P\left(x,-h(x)\right)\left[-\frac{\partial h(x)}{\partial x}\right]dx \\ = & \ \mathcal{I}_i - \mathcal{I}_{i+1} - \mathcal{I}_{i+\frac{1}{2}}\,, \end{aligned} \tag{3.7}$$

where we have neglected the effect of atmospheric pressure applied to the slopping surface of the ocean. In (3.7), $P(x,z)$ is the hydrostatic pressure,

$$P(x,z) = g\int_{z'}^{\zeta_i} \rho(x,z')\,dz'\,. \tag{3.8}$$

Assuming a finite-volume approach to approximate (3.8) and eventually (3.7) at the discrete level, the barotropic pressure-gradient force at the velocity point $i+\frac{1}{2}$ is a function of the density in the vertical columns i and $i+1$, as well as the free-surface elevations ζ_{i+1}. Thus, ζ_i,

$$F_{i+\frac{1}{2}} = \mathcal{F}\left(\zeta_{i+1},\overline{\rho}_{i+1,1},...,\overline{\rho}_{i+1,N},\zeta_i,\overline{\rho}_{i,1},...,\overline{\rho}_{i,N}\right)\,, \tag{3.9}$$

where the structure of the functional $\mathcal{F}$ depends upon the discretization details of the baroclinic pressure gradient. Usually there is a nonlinear dependency of $\mathcal{F}$ on $\zeta_{i'}$ and $\overline{\rho}_{i',k}$,

$$\frac{\partial^2\mathcal{F}}{\partial\zeta_{i'}\,\partial\overline{\rho}_{i'',k}} \neq 0 \tag{3.10}$$

where $i',i'' = i,i+1$ in arbitrary combination and $k = 1,...,N$. Consequently, one cannot split $\mathcal{F}$ into

$$\mathcal{F} \neq \mathcal{F}_1\left(\zeta_{i+1},\zeta_i\right) + \mathcal{F}_2\left(\overline{\rho}_{i+1,1},...,\overline{\rho}_{i+1,N},\overline{\rho}_{i,1},...,\overline{\rho}_{i,N}\right)\,, \tag{3.11}$$

where $\mathcal{F}_2$ does not depend on ζ.

In the mode splitting technique proposed here, we assume that free-surface field ζ is changing during the barotropic time stepping while the density values $\overline{\rho}_{i,k}$ remain frozen and change only during the baroclinic time step. However, the nonlinear relation (3.9) holds in barotropic time. Of course, it would be prohibitively unefficient to recompute $\mathcal{F}$ in (3.9) at every barotropic step by vertical integration of the whole three-dimensional pressure gradient. Instead, in each vertical column, once at every baroclinic time step before the barotropic mode calculation begins, we compute a vertically averaged density,

$$\overline{\rho}(x) = \frac{1}{D}\int_{-h(x)}^{\zeta(x)} \rho(x,z')dz' \tag{3.12}$$

and vertically averaged dynamical density,

$$\rho^*(x) = \frac{1}{\frac{1}{2}D^2}\int_{-h(x)}^{\zeta(x)} \left\{\int_{z}^{\zeta(x)} \rho(x,z')dz'\right\} dz\,, \tag{3.13}$$

where $D \equiv D(x) = \zeta(x) + h(x)$ is the total thickness of the water column. After this, (3.7) becomes

$$F_{i+\frac{1}{2}} = g\left\{\frac{\rho_i^* D_i^2}{2} - \frac{\rho_{i+1}^* D_{i+1}^2}{2} + \int_{x_i}^{x_{i+1}} \overline{\rho} D\,\frac{\partial h}{\partial x}dx\right\}\,. \tag{3.14}$$

This is a finite-volume discretization of the pressure-gradient term in the right side of the vertically integrated momentum equation,

$$\begin{aligned} \frac{\partial}{\partial t}\left(D\overline{U}\right) + ... = & -\frac{1}{\rho_0}g\left\{\frac{\partial}{\partial x}\left(\frac{\rho^* D^2}{2}\right) - \overline{\rho}D\frac{\partial h}{\partial x}\right\} \\ = & -\frac{1}{\rho_0}gD\left\{\rho^*\frac{\partial\zeta}{\partial x} + \frac{D}{2}\frac{\partial\rho^*}{\partial x} + \left(\rho^* - \overline{\rho}\right)\frac{\partial h}{\partial x}\right\}\,. \end{aligned} \tag{3.15}$$

In the case of $\rho^* \equiv \overline{\rho} \equiv \rho_0$, the right side of (3.15) reduces to the familiar free-surface pressure-gradient term of the shallow-water equations, but in general it contains two extra terms that are baroclinic in nature.

Since $\overline{\rho}$ and ρ^* are just two-dimensional fields and neither of them actually depends on ζ (despite the fact that ζ appears in (3.12) and (3.13)), the right-side terms of (3.15) can be efficiently computed at a cost comparable to that of the shallow-water pressure gradient. The problem therefore reduces to the search for a suitable method of calculation of $\overline{\rho}$ amd ρ^* from the set of discrete values $\overline{\rho}_{i,k}$, $k = 1, ..., N$ and an appropriate discretization of (3.15).

To address the first issue, consider, *e.g.,* a piecewise-parabolic reconstruction of the vertical density profile from a set of discrete values $\left\{\overline{\rho}_k \,|\, k = 1,...,N\right\}$ that is interpreted as a set of grid-box averages within each vertical vertical grid box H_k[8], (Fig. 11),

$$\rho(z') = \overline{\rho}_k + \frac{\rho_{k+\frac{1}{2}} + \rho_{k-\frac{1}{2}}}{H_k}z' \tag{3.16}$$

---

[8] For simplicity of notation, we dropped the horizontal index i in

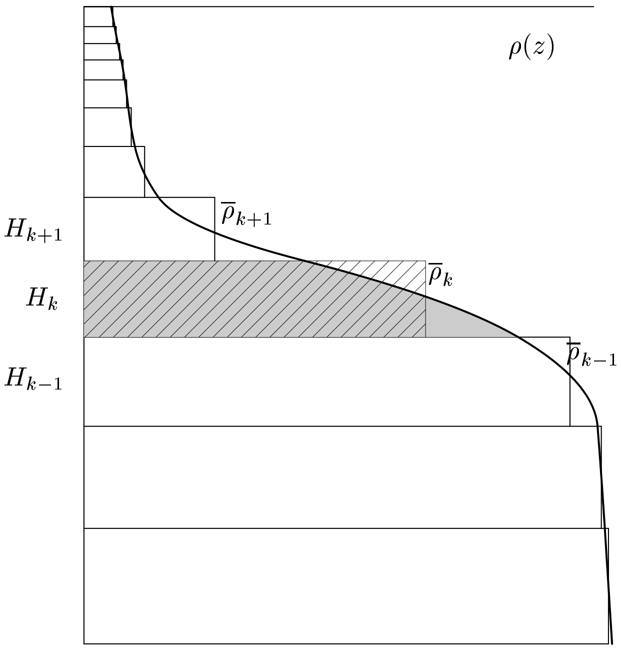

Figure 11. Reconstruction of the vertical density profile using parabolic segments. The gridded data $\overline{\rho}_k$, $k = 1, 2, ..., N$ is interpreted as a set of grid-box averages within grid boxes H_k of the vertically non-uniform grid. The shaded area is the same as the area of the diagonally hatched rectangle.

$$+6\left(\frac{\rho_{k+\frac{1}{2}} + \rho_{k-\frac{1}{2}}}{2} - \overline{\rho}_k\right)\left(\frac{z'^2}{H_k^2} - \frac{1}{12}\right) .$$

Here the local vertical coordinate z' spans within the grid box H_k, so that $-\frac{H_k}{2} \leq z' \leq +\frac{H_k}{2}$, and $\rho_{k\pm\frac{1}{2}} \equiv \rho\left(\pm\frac{H_k}{2}\right)$ are the density values at at the upper and lower grid box interfaces, $z = \pm\frac{H_k}{2}$ computed via an appropriate reconstruction algorithm (Appendix B). (3.16) guarantees that

$$\frac{1}{H_k}\int\limits_{-H_k/2}^{+H_k/2} \rho(z')\, dz' \equiv \overline{\rho}_k\,, \tag{3.17}$$

regardless of the particular method of computation of $\rho_{k\pm\frac{1}{2}}$.

The hydrostatic pressure in (3.7) can be computed analytically within each grid box H_k,

$$P(z') = P_{k+\frac{1}{2}} + g\int\limits_{z'}^{H_k/2} \rho(z'')\, dz''\,, \tag{3.18}$$

or

$$\begin{aligned} P(z') = P_{k+\frac{1}{2}} + gH_k \Bigg\{ & \overline{\rho}_k \left[\frac{1}{2} - \frac{z'}{H_k}\right] \\ & + \frac{1}{2}\left(\rho_{k+\frac{1}{2}} - \rho_{k-\frac{1}{2}}\right)\left[\frac{1}{4} - \frac{z'^2}{H_k^2}\right] \\ & + 2\left(\frac{\rho_{k+\frac{1}{2}} + \rho_{k-\frac{1}{2}}}{2} - \overline{\rho}_k\right)\left[\frac{z'}{4H_k} - \frac{z'^3}{H_k^3}\right]\Bigg\} . \end{aligned} \tag{3.19}$$

$P_{k+\frac{1}{2}}$ is the value of pressure at depth corresponding to the interface between H_k and H_{k+1},

$$P_{N+\frac{1}{2}} = 0 \quad \text{and} \quad P_{k-\frac{1}{2}} = g\sum_{k'=k}^{N} \overline{\rho}_{k'} H_{k'}\,, \qquad k = 1, ..., N\,. \tag{3.20}$$

One can easily verify from (3.19) that $P(-H_k/2) \equiv P_{k-\frac{1}{2}}$, as well as the fact that the pressure distribution is continuous across the grid box interfaces along with its first and second derivatives. In the finite-volume approach, (3.20) is to be understood as exact rather than as a discrete approximation to the hydrostatic equation.

The quantity,

$$\mathcal{I}_i = \int\limits_{-h}^{\zeta} P(z)\, dz = \sum_{k=1}^{N}\int\limits_{-H_k/2}^{+H_k/2} P(z')\, dz' = \sum_{k=1}^{N} H_k \overline{P}_k\,, \tag{3.21}$$

where

$$\begin{aligned} \overline{P}_k &= P_{k+\frac{1}{2}} + \frac{1}{2}gH_k\left(\overline{\rho}_k + \frac{\rho_{k+\frac{1}{2}} - \rho_{k-\frac{1}{2}}}{6}\right) \\ &= \frac{P_{k+\frac{1}{2}} + P_{k-\frac{1}{2}}}{2} + gH_k\frac{\rho_{k+\frac{1}{2}} - \rho_{k-\frac{1}{2}}}{12}\,, \end{aligned} \tag{3.22}$$

has the meaning of pressure averaged over H_k. Consistent with (3.16), the vertically averaged density $\overline{\rho}_i$ is given by

$$\overline{\rho}_i = \frac{\sum\limits_{k=1}^{N} \overline{\rho}_{i,k} H_{i,k}}{\sum\limits_{k=1}^{N} H_{i,k}}\,. \tag{3.23}$$

From (3.22), the vertically averaged dynamical density ρ_i^* is

$$\begin{aligned} \rho_i^* = \frac{1}{\frac{1}{2}\left(\sum\limits_{k=1}^{N} H_{i,k}\right)^2} \cdot \sum_{k=1}^{N} H_{i,k} \Bigg[& \left(\sum_{k'=k+1}^{N} \overline{\rho}_{i,k'} H_{i,k'}\right) \\ & + \frac{1}{2}H_{i,k}\left(\overline{\rho}_{i,k} + \frac{\rho_{i,k+\frac{1}{2}} - \rho_{i,k-\frac{1}{2}}}{6}\right)\Bigg] . \end{aligned} \tag{3.24}$$

(3.16) and throughout the following part of this section. We use index k exclusively for the vertical coordinate while i and j refer to the horizontal coordinates. We will allow indices to disappear and reappear. In the particular context where k is the only present, all related operations are being performed within the vertical column atomically (*i.e.,* independently in one vertical column from another).

Since

$$\sum_{k=1}^{N} H_{i,k}\left[\left(\sum_{k'=k+1}^{N} H_{i,k'}\right)+\frac{1}{2}H_{i,k}\right]\equiv\frac{1}{2}\left(\sum_{k=1}^{N} H_{i,k}\right)^{2} ,$$

the procedure (3.24) is a weighted averaging. Since

$$\sum_{k=1}^{N} H_{i,k}\equiv h_i+\zeta_i\equiv D_i, \tag{3.25}$$

(3.21) may be expressed as

$$\mathcal{I}_i=\frac{1}{2}g\rho_i^{*}D_i^{2} . \tag{3.26}$$

To approximate $\mathcal{I}_{i+\frac{1}{2}}$, we assume that D, $\overline{\rho}$, and h are linear functions of the horizontal coordinate between points x_i and x_{i+1}:

$$\begin{aligned}\mathcal{I}_{i+\frac{1}{2}}=&\int_{x_i}^{x_{i+1}}\left(\overline{\rho}_i\frac{x_{i+1}-x'}{\Delta x}+\overline{\rho}_{i+1}\frac{x'-x_i}{\Delta x}\right)\\&\times\left(D_i\frac{x_{i+1}-x'}{\Delta x}+D_{i+1}\frac{x'-x_i}{\Delta x}\right)\frac{h_{i+1}-h_i}{\Delta x}dx'\\=&\frac{\left(\overline{\rho}_i+\overline{\rho}_{i+1}\right)\left(D_i+D_{i+1}\right)+\overline{\rho}_iD_i+\overline{\rho}_{i+1}D_{i+1}}{6}\\&\times\left(h_{i+1}-h_i\right) .\end{aligned}\tag{3.27}$$

From (3.26) and (3.27) after some algebra — essentially repeating the transition from the first to the second line of (3.15) for the discrete formulation — yields

$$\begin{aligned}F_{i+\frac{1}{2}}=&\,g\frac{D_i+D_{i+1}}{2}\frac{\rho_i^{*}+\rho_{i+1}^{*}}{2}\left(\zeta_i-\zeta_{i+1}\right)\\&+g\frac{D_i^2+D_{i+1}^2}{4}\left(\rho_i^{*}-\rho_{i+1}^{*}\right)\\&+g\frac{D_i+D_{i+1}}{2}\frac{\left(\rho_i^{*}-\overline{\rho}_i\right)+\left(\rho_{i+1}^{*}-\overline{\rho}_{i+1}\right)}{2}\left(h_i-h_{i+1}\right)\\&+\frac{\left(\overline{\rho}_{i+1}-\overline{\rho}_i\right)\left(D_{i+1}-D_i\right)\left(h_{i+1}-h_i\right)}{12}.\end{aligned}\tag{3.28}$$

The terms on the first, second, and third lines are obviously similar to the first, second, and third terms on the second line in (3.15), respectively. The term on the fourth line in (3.28) is of on the order of $\mathcal{O}\left((\Delta x)^3\right)$ while all three preceding terms are $\mathcal{O}\left(\Delta x\right)$, so the former is negligible relative to the others as $\Delta x\to 0$.

In the case of $\zeta_i=\zeta_{i+1}=0$, hence $D_i=h_i$ and $D_{i+1}=h_{i+1}$, (3.28) after some manipulation becomes

$$\begin{aligned}F_{i+\frac{1}{2}}^{(0)}=&\,g\left(\rho_i^{*}-\overline{\rho}_i\right)\frac{h_i^2}{2}-g\left(\rho_{i+1}^{*}-\overline{\rho}_{i+1}\right)\frac{h_{i+1}^2}{2}\\&+g\left(\overline{\rho}_i-\overline{\rho}_{i+1}\right)\frac{h_i^2+h_ih_{i+1}+h_{i+1}^2}{6} .\end{aligned}\tag{3.29}$$

Unlike the SWE pressure gradient, this does not vanish unless there is a special balance between the densities ρ_i^{*}, ρ_{i+1}^{*}, $\overline{\rho}_i$, $\overline{\rho}_{i+1}$, and the unperturbed thicknesses, h_i and h_{i+1}. For example, if density is a linear function of depth, $\rho=\rho(z)=-\alpha z$ resulting in

$$\overline{\rho}_i=\frac{1}{h_i}\int_{-h_i}^{0}\left(-\alpha z\right)dz=\frac{\alpha h_i}{2} \tag{3.30}$$

$$\rho_i^{*}=\frac{2}{h_i^2}\int_{-h_i}^{0}\int_{z}^{0}\left(-\alpha z'\right)dz'=\frac{\alpha h_i}{3} . \tag{3.31}$$

Then $F_{i+\frac{1}{2}}^{(0)}$ vanishes, as verified by direct substitution of these expressions into (3.29).

We therefore split (3.28) into

$$F_{i+\frac{1}{2}}=F_{i+\frac{1}{2}}^{(0)}+F'_{i+\frac{1}{2}} , \tag{3.32}$$

where

$$\begin{aligned}F'_{i+\frac{1}{2}}=&-\frac{1}{2}g\Big\{\left(h_i+h_{i+1}\right)\left(\rho_{i+1}^{*}\zeta_{i+1}-\rho_i^{*}\zeta_i\right)\\&+\rho_{i+1}^{*}\zeta_{i+1}^2-\rho_i^{*}\zeta_i^2\\&+\left(h_{i+1}-h_i\right)\Big[\left(\rho_{i+1}^{*}-\overline{\rho}_{i+1}\right)\zeta_{i+1}+\left(\rho_i^{*}-\overline{\rho}_i\right)\zeta_i\\&+\frac{1}{3}\left(\overline{\rho}_{i+1}-\overline{\rho}_i\right)\left(\zeta_{i+1}-\zeta_i\right)\Big]\Big\}\end{aligned}\tag{3.33}$$

collects all the terms of (3.28) that contain ζ. The transition from (3.28) to (3.29)–(3.33) has been made without any approximations.

We summarize several important properties of (3.29)–(3.33):

(i) (3.33) is comprised of two parts. The first two lines constitute a generalized SWE pressure-gradient term that, in the case of uniform density, $\rho_i^{*}=\overline{\rho}_i=\rho_{i+1}^{*}=\overline{\rho}_{i+1}=\rho_0$, becomes equivalent to the familiar barotropic SWE pressure gradient,

$$F_{i+\frac{1}{2}}=-g\rho_0\frac{D_i+D_{i+1}}{2}\left(\zeta_{i+1}-\zeta_i\right) . \tag{3.34}$$

The remaining two lines in (3.33) correspond to the baroclinic response in pressure-gradient force to a perturbation of ζ in the presense of stratification and topography (*n.b.*, these terms vanish if the density field is uniform).

(ii) For any given set of grid-box-averaged densities, $\overline{\rho}_{i,k}$, in a vertical column i, the values of $\overline{\rho}_i$ and ρ_i^{*} do not depend on the free-surface elevation ζ_i. (1.10)—(1.11) imply that the disturbance of the free-surface field causes a linear stretching of all H_k,

$$H_{i,k}=H_{i,k}^{(0)}\cdot\left(1+\frac{\zeta_i}{h_i}\right) , \tag{3.35}$$

where $H_{i,k}^{(0)}$ are the grid box heights corresponding to an unperturbed free surface. Consequently, replacement of $H_{i,k}^{(0)}$ with $H_{i,k}$ in (3.23) and (3.24) causes both the numerator and denominator to be multiplied by $(1+\zeta_i/h_i)$ and $(1+\zeta_i/h_i)^2$ respectively.

(iii) Once the *in siti* density increases with depth so that all $d_{k+\frac{1}{2}} \le 0$ [9], then

$$\rho_i^* \le \overline{\rho}_i . \tag{3.36}$$

This implies that the effective barotropic pressure gradient (*i.e.,* the contribution due to the perturbation of ζ) of a stratified fluid is systematically less than that for uniform density with the same ζ.

(iv) If the density field is a function of depth only (*i.e.,* horizontally uniform stratification), the baroclinic pressure gradient should vanish. However, in order to make $F_{i+\frac{1}{2}}^{(0)} = 0$ in (3.29), there must be cancellation between its terms that can be achieved only by having a special relation between ρ_i^* and $\overline{\rho}_i$. Except for a few special choices of the density profile (constant, linear, or quadratic in z), this cancellation is not exact, but rather relies on the numerical accuracy of the integration method. This is often referred as *hydrostatic inconsistency.* The use of a high-order integration method does not offer an escape from inconsistency; it just reduces the error. For example, dropping the term,

$$gH_k \frac{\rho_{k+\frac{1}{2}} - \rho_{k-\frac{1}{2}}}{12}, \tag{3.37}$$

in (3.22) is equivalent to switching from a parabolic to a trapezoidal rule in integration of the hydrostatic equation. Since in stable stratification we expect all these terms to be negative, there is a systematic bias in ρ_i^* caused by this reduction of the order of accuracy.

(v) The use of parabolic spline reconstruction formally removes the necessity to have the σ-coordinate mapping (1.5) be a continuous and differentiable function of σ in order to make the discrete approximation be consistent with the continuous equations (*cf.,* Mesinger, 1982, Haney, 1991, Treguier, *et al.*, 1996). Even if the set of grid box thicknesses $\{H_k\ ,\ k=1,...,N\}$ is allowed to change suddenly from large to small values, the spline reconstruction always gives a continuous, smooth density profile that is then integrated analytically without any further approximation.

(vi) The methodology we have adopted for the computation of vertically integrated pressure-gradient force can be viewed as high-order generalization of the finite volume method of Lin, 1997, where the trapezoidal integration rules for pressure field (corresponding to a piecewise-constant density distribution within each grid box) is replaced with parabolic splines for density integration and cubic polynomials for pressure integrals, thus gaining two orders of accuracy of vertical discretization.

3.2. Temporal Averaging of the Barotropic Mode

The fluxes $U_{i+\frac{1}{2},j,k}$, $V_{i,j+\frac{1}{2},k}$, and $W_{i,j,k+\frac{1}{2}}$ in (1.16)–(1.18) are defined in the *finite-volume* and *finite-time-step* senses; *i.e.,* during a time interval Δt, the sum of fluxes across the moving facets of the grid element $\Delta\mathcal{V}_{i,j,k}$ produce a change in the volume of fluid inside that is equivalent to the difference of $\Delta\mathcal{V}_{i,j,k}^{n+1} - \Delta\mathcal{V}_{i,j,k}^{n}$, which in turn is determined by the free-surface equation advanced in time with a different time step and time-stepping algorithm. Hence, the goal of two-dimensional barotropic sub-model is formulated as follows:

Given the initial conditions for the free surface elevation ζ^n and the vertically integrated velocity $\overline{\mathbf{U}}^n$ at the time corresponding to the baroclinic time step n, as well as the baroclinic forcing functions (*i.e.,* vertically integrated right side of the three-dimensional momentum equations), compute the following:

(*i*) $\langle\zeta\rangle^{n+1}$ and $\langle\overline{\mathbf{U}}\rangle^{n+1}$ corresponding to the new baroclinic time step $n+1$, properly averaged to filter out barotropic time scales not resolved by the baroclinic time step (to avoid temporal aliasing); and

(*ii*) barotropic mass flux, $\langle\!\langle\overline{\mathbf{U}}\rangle\!\rangle^{n+\frac{1}{2}}$, integrated over the barotropic time stepping, satisfying the slow-time free-surface equation (1.19).

Assume that there are M barotropic time steps within one baroclinic step, so that the fast time index $m=0$ corresponds to the baroclinic step n, while $m=M$ corresponds to the step $n+1$. We must choose an appropriate weighting shape function a_m; *e.g.,*

$$a_m = \mathcal{A}_* \left(\frac{m}{M_*}\right)^p \left[1 - \left(\frac{m}{M_*}\right)^q\right] \qquad m \le M_* \,, \tag{3.38}$$

where $\mathcal{A}_*$ and M_* are chosen to satisfy discrete normalization and centroid conditions,

$$\sum_{m=1}^{M_*} a_m \equiv 1 \,, \qquad \sum_{m=1}^{M_*} a_m \frac{m}{M} \equiv 1 \,, \tag{3.39}$$

and parameters p and q control the filter shape. (The optimal choices of these are discussed below.) In practice

---

[9] In the case of an incompressible fluid, this condition is equivalent to stable stratification. However, once compressibility effects are taken into account, it becomes less restrictive than stable stratification, since the later requires an increase of potential density with depth, rather than just *in situ* density.

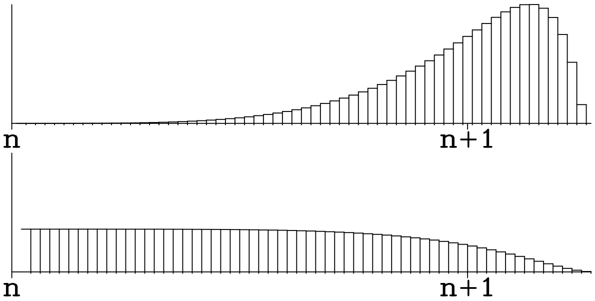

Figure 12. Structure of the fast-time-averaging filter. **upper panel:** primary weights defined by (3.38) with $p = 4$ and $q = 8$; **lower panel:** corresponding secondary weights (3.46). Small tickmarks correspond to fast (barotropic time steps), and large tickmarks labeled by n and $n+1$ correspond to the old and new baroclinic time steps.

we initially set[10]

$$\mathcal{A}_* = 1 \quad \text{and} \quad M_* = M\frac{(p+2)\,(p+q+2)}{(p+1)\,(p+q+1)},$$

compute $\{a_m\}$ via (3.38), normalize them, and iteratively adjust by moving $\{a_m\}$ to the left or right until the second discrete condition (3.39) is satisfied. The actual number of fast time steps performed within each baroclinic step M_* is always greater than the splitting ratio M, depending on the filter width, but it never exceeds $3M/2$.

Once the set of weights $\{a_m\}$ is specified, we define

$$\begin{aligned} \langle\zeta\rangle_{i,j}^{n+1} &= \sum_{m=1}^{M_*} a_m \zeta_{i,j}^m \\ \langle\overline{U}\rangle_{i+\frac{1}{2},j}^{n+1} &= \sum_{m=1}^{M_*} a_m \overline{U}_{i+\frac{1}{2},j}^m \\ \langle\overline{V}\rangle_{i,j+\frac{1}{2}}^{n+1} &= \sum_{m=1}^{M_*} a_m \overline{V}_{i,j+\frac{1}{2}}^m \,, \end{aligned} \tag{3.40}$$

where ζ^m, $\overline{U}^m$, and $\overline{V}^m$ are "instantaneous" barotropic variables. To satisfy the slow-time continuity equation (1.18), we construct another set of fast-time-averaged barotropic fluxes, $\langle\!\langle\overline{U}\rangle\!\rangle \mid$ and $\langle\!\langle\overline{V}\rangle\!\rangle \mid$,

$$\langle\zeta\rangle_{i,j}^{n+1} = \langle\zeta\rangle_{i,j}^{n} - \Delta t \cdot \mathrm{div}\langle\!\langle\overline{\mathbf{U}}\rangle\!\rangle_{i,j}^{n+\frac{1}{2}} \tag{3.41}$$

where

$$\mathrm{div}\langle\!\langle\overline{\mathbf{U}}\rangle\!\rangle_{i,j}^{n+\frac{1}{2}} = \frac{1}{\Delta\mathcal{A}_{i,j}}\left[\langle\!\langle\overline{U}\rangle\!\rangle_{i+\frac{1}{2},j}^{n+\frac{1}{2}} - \langle\!\langle\overline{U}\rangle\!\rangle_{i-\frac{1}{2},j}^{n+\frac{1}{2}} \right. \tag{3.42}$$

$$\left. + \langle\!\langle\overline{V}\rangle\!\rangle_{i,j+\frac{1}{2}}^{n+\frac{1}{2}} - \langle\!\langle\overline{V}\rangle\!\rangle_{i,j-\frac{1}{2}}^{n+\frac{1}{2}} \right] .$$

This is accomplished by defining another set of weighting coefficients, $\{b_m\}$, derived from $\{a_m\}$. Assuming for simplicity that a forward-backward step is applied to advance the barotropic mode (hence just a forward step for the ζ equation),

$$\zeta^m = \zeta^{m-1} + \frac{\Delta t}{M}\cdot \mathrm{div}\overline{\mathbf{U}}^m \,, \qquad \forall\, m = 1, ..., M_* \,, \tag{3.43}$$

where operation $\mathrm{div}\overline{\mathbf{U}}^m$ is similar to (3.42) except that it is applied to instantaneous barotropic fluxes $\overline{U}_{i+\frac{1}{2},j}^m$ and $\overline{V}_{i,j+\frac{1}{2}}^m$. Successive summation of (3.43) with consecutive m yields[11]

$$\zeta^m = \zeta^0 + \frac{\Delta t}{M}\sum_{m'=1}^{m} \mathrm{div}\overline{\mathbf{U}}^{m'} \,, \tag{3.44}$$

which, after applying the time-averaging procedure (3.40) to both sides, becomes

$$\langle\zeta\rangle^{n+1} \equiv \sum_{m=1}^{M_*} a_m \zeta^m = \zeta^0 + \frac{\Delta t}{M}\sum_{m=1}^{M_*}\left[a_m \sum_{m'=1}^{m} \mathrm{div}\overline{\mathbf{U}}^{m'}\right] .$$

After rearranging the order of summation, it is

$$\langle\zeta\rangle^{n+1} = \zeta^0 + \Delta t \sum_{m'=1}^{M_*} b_{m'} \mathrm{div}\overline{\mathbf{U}}^{m'} \,, \tag{3.45}$$

where the new set of weights $\{b_{m'}\}$ is computed from the original set $\{a_m\}$ via

$$b_{m'} = \frac{1}{M}\sum_{m=1}^{m'} a_m \,, \qquad \forall m = 1, ..., M_* \,. \tag{3.46}$$

The relationship between the two sets of weights is illustrated in Fig. 2. We define

$$\begin{aligned} \langle\!\langle\overline{U}\rangle\!\rangle_{i+\frac{1}{2},j}^{n+\frac{1}{2}} &= \sum_{m=1}^{M_*} b_m \overline{U}_{i+\frac{1}{2},j}^m \\ \langle\!\langle\overline{V}\rangle\!\rangle_{i,j+\frac{1}{2}}^{n+\frac{1}{2}} &= \sum_{m=1}^{M_*} b_m \overline{V}_{i,j+\frac{1}{2}}^m \,, \end{aligned} \tag{3.47}$$

---

[10] This setting results in a center of gravity for $\{a_m\}$ at $m/M = 1$ in the limit $M \to \infty$ where m/M in (3.38) is treated as a continuous variable, allowing replacement of the discrete sum with an integral that is calculated analytically.

[11] In this section we use the following convention for temporal indices: n-indices — n, $n+1$ and $n+\frac{1}{2}$ – are the slow time indices corresponding to the time steps of baroclinic mode; m-indices run from 0 to $M|a_M > 0$, so that $M \geq N$ (Fig. 2), fast-time indices corresponding to time steps of the barotropic mode. In (3.44) ζ^0 means ζ corresponding to $m = 0$, the initial state for the sequence of barotropic time steps starting from the time corresponding to baroclinic time step n, so that $\zeta^0 \equiv \zeta^{m=0} = \zeta^n$. The ζ^m are the instantaneous barotropic fields, while ζ^n and ζ^{n+1} are fast-time averaged. Consequently, even though ζ^{n+1} and $\zeta^{m=N}$ correspond to the same absolute time, $\zeta^{n+1} \neq \zeta^{m=N}$; however, this would be the case if the set of filtering weights $\{a_m\}$ is replaced by a delta function, $a_m \equiv 0$ for $m \neq M$ and $a_M = 1$. The same index convention holds for the barotropic mass fluxes.

that satisfy (3.41) when the integration of (3.43) starts with $\zeta^0 \equiv \langle\zeta\rangle^n$. This implies that once the barotropic time stepping is complete, the instantaneous values of free-surface elevation ζ and barotropic mass fluxes $\overline{\mathbf{U}}$ are replaced with their fast-time averages in the sense of (3.40). These averaged values are used as initial conditions for the barotropic mode during the next baroclinic time step.

After the completion of time stepping for the barotropic mode, the vertical coordinate system is updated via (1.11) using $\langle\zeta\rangle^{n+1}$. The new set of $H^{n+1}_{i,j,k}$ becomes available to complete the three-dimensional time step. This is followed by computation of $u^{n+1}_{i+\frac{1}{2},j,k}$, $v^{n+1}_{i,j+\frac{1}{2},k}$ and their subsequent vertical integration. The integrals are subtracted from $\langle\overline{U}\rangle^{n+1}_{i+\frac{1}{2},j}$ and $\langle\overline{V}\rangle^{n+1}_{i,j+\frac{1}{2}}$, and the difference is divided by the depth corresponding to $\langle\zeta\rangle^{n+1}$ and the local topography h. The resultant correction term is then distributed uniformly throughout the vertical column to ensure that vertical integrals of updated $u^{n+1}_{i+\frac{1}{2},j,k}$ and $v^{n+1}_{i,j+\frac{1}{2},k}$ are exactly the same as $\langle\overline{U}\rangle^{n+1}_{i+\frac{1}{2},j}$ and $\langle\overline{V}\rangle^{n+1}_{i,j+\frac{1}{2}}$. The update of the three-dimensional velocity field is now complete.

The update of the tracer fields follows next. It begins with interpolation of three-dimensional velocities between time steps n and $n+1$ to compute the mass fluxes $U^{n+\frac{1}{2}}$ and $V^{n+\frac{1}{2}}$ that are then corrected in the way just described to ensure that their vertical integrals are exactly equal to $\langle\!\langle\overline{U}\rangle\!\rangle^{n+\frac{1}{2}}$ and $\langle\!\langle\overline{V}\rangle\!\rangle^{n+\frac{1}{2}}$. This guarantees that after computation of the vertical velocity $W^{n+\frac{1}{2}}$ via (1.23) and substitution of H^n, H^{n+1}, $U^{n+\frac{1}{2}}$, $V^{n+\frac{1}{2}}$, and $W^{n+\frac{1}{2}}$ into (1.18), the later condition holds exactly. Tracer fluxes are then computed by an interpolation of the tracer concentration in space and in time toward the placement of the corresponding velocity component (Section 4), with a subsequent multiplication by that component. The resultant time step for the tracer field is both conservative and constancy preserving.

3.3. Algorithmic Details

For simplicity in the time averaging procedure above, we have assumed that forward time step is applied to advance the free-surface equation. Since the actual time-stepping algorithm in ROMS is different, we need to show in more detail how to combine it with the averaging procedure.

The equations for the barotropic mode are

$$\frac{\partial\zeta}{\partial t} + \mathrm{div}\overline{\mathbf{U}} = 0 \tag{3.48}$$

$$\frac{\partial\overline{\mathbf{U}}}{\partial t} + f\mathbf{k}\times\overline{\mathbf{U}} = F(\zeta) + \ldots\, . \tag{3.49}$$

The barotropic pressure gradient $F(\zeta)$ is defined in the simplest case as

$$F(\zeta) = -g(h+\zeta)\nabla\zeta\,, \tag{3.50}$$

but more generally it is computed with (3.33). The dots in (3.49) denote slowly varying terms (*e.g.,* the influence of baroclinic-mode, nonlinear, and viscous terms), most of which are kept constant during the barotropic time stepping within one baroclinic step.

Once a value of barotropic time step size, $\Delta t_* = dt/M$ is chosen, two non-dimensional numbers arise, *viz.,*

$$\Delta t_*\sqrt{gh\left(\frac{1}{\Delta x^2}+\frac{1}{\Delta y^2}\right)} \qquad \text{and} \qquad f\Delta t_*\,. \tag{3.51}$$

These are the Courant number for external gravity waves[12] (on the left) and the ratio of the time step to an inertial period (on the right). For any reasonable choice of parameters, the former is more restrictive than that the later: *e.g.,* for horizontal grid spacings $\Delta x = \Delta y = 45$ km and the characteristic depth $h = 5000$ m, it reaches unity at $\Delta t_* = 150$ s, while $f\Delta t_*$ does not exceed 0.01. This contrast is even larger for a finer spatial resolution. Consequently, the design of the time-stepping algorithm for the barotropic mode is optimized for temporal stability of the discrete pressure gradient.

Taking this into account, we introduce a predictor-corrector algorithm optimized for the largest possible time step per computation of the r.h.s. using (2.34)–(2.37) as the prototype:

Predictor sub-step,

$$\zeta^{m+\frac{1}{2}} = \left(\frac{1}{2}-2\gamma\right)\zeta^{m-1} + \left(\frac{1}{2}+2\gamma\right)\zeta^{m} - \Delta t_*\left(1-2\gamma\right)\mathrm{div}\overline{\mathbf{U}}^{m} \tag{3.52}$$

$$\overline{\mathbf{U}}^{m+\frac{1}{2}} = \left(\frac{1}{2}-2\gamma\right)\overline{\mathbf{U}}^{m-1} + \left(\frac{1}{2}+2\gamma\right)\overline{\mathbf{U}}^{m} + \Delta t_*\left(1-2\gamma\right)\left[F(\zeta') - D^m f\mathbf{k}\times\overline{\mathbf{u}}^m + \ldots\right]\,, \tag{3.53}$$

where

$$\zeta' = \zeta^m + \beta\frac{2\zeta^{m+\frac{1}{2}} - 3\zeta^m + \zeta^{m-1}}{1-2\gamma}\,. \tag{3.54}$$

Corrector sub-step,

$$\zeta^{m+1} = \zeta^m - \Delta t_*\mathrm{div}\overline{\mathbf{U}}^{m+\frac{1}{2}} \tag{3.55}$$

$$\overline{\mathbf{U}}^{m+1} = \overline{\mathbf{U}}^{m} + \Delta t_*\left[F(\zeta'') - D''f\mathbf{k}\times\overline{\mathbf{u}}^{m+\frac{1}{2}} + \ldots\right]\,, \tag{3.56}$$

---

[12] The exact expression on the left of (3.51) is derived assuming a non-rotational ($f = 0$), constant-depth shallow-water model discretized on a C-grid and using Forward-Backward time step.

where

$$\zeta'' = (1-\epsilon)\,\zeta^{m+\frac{1}{2}} + \epsilon\left[\left(\frac{1}{2}-\gamma\right)\zeta^{m+1} + \left(\frac{1}{2}+2\gamma\right)\zeta^{m} - \gamma\zeta^{m-1}\right]. \tag{3.57}$$

Here $Df\mathbf{k}\times\overline{\mathbf{u}}^{m+\frac{1}{2}}$ and $D\equiv h+\zeta$ symbolize an Arakawa spatial discretization of the Coriolis term on a C-grid to ensure no contribution to the kinetic energy integral. (It implies that velocity components ($\overline{u}$, $\overline{v}$) are interpolated first to the location of ζ-points on the C-grid, where they multiplied by Coriolis parameter f and depth D; the products are then interpolated further to the locations of the partner component.) Despite its relatively sophisticated appearance, the computational cost of this algorithm is approximately the same as for the widely used Leap-Frog–Trapezoidal Rule (LF–TR) predictor-corrector algorithm. During both sub-steps, the computation begins with obtaining the new ζ field that then immediately participates in the computation of pressure-gradient terms for $\overline{\mathbf{U}}$ updates via the provisional fields, ζ' and ζ'' (time centered at m and $m+\frac{1}{2}$). Computation of $\langle\zeta\rangle^{n+1}$ and $\langle\overline{\mathbf{U}}\rangle^{n+1}$ is done by applying the averaging procedure (3.40) to ζ^{m+1} and $\overline{\mathbf{U}}^{m+1}$ at the end of corrector sub-step. Similarly, $\langle\!\langle\overline{\mathbf{U}}\rangle\!\rangle^{n+\frac{1}{2}}$ is obtained via (3.47) applied to $\overline{\mathbf{U}}^{m+\frac{1}{2}}$ during the update of (3.55).

A more efficient, generalized forward-backward step (*cf.,* (2.41)) starts with AB3-extrapolation of free-surface elevation and barotropic velocities,

$$\zeta^{m+\frac{1}{2}} = \left(\frac{3}{2}+\beta\right)\zeta^{m} - \left(\frac{1}{2}+2\beta\right)\zeta^{m-1} + \beta\zeta^{m-2}$$

$$\overline{\mathbf{u}}^{m+\frac{1}{2}} = \left(\frac{3}{2}+\beta\right)\overline{\mathbf{u}}^{m} - \left(\frac{1}{2}+2\beta\right)\overline{\mathbf{u}}^{m-1} + \beta\overline{\mathbf{u}}^{m-2},$$

with a subsequent computation of fluxes,

$$\overline{U}^{m+\frac{1}{2}} = D^{m+\frac{1}{2}}\overline{u}^{m+\frac{1}{2}}\Delta\eta \qquad \overline{V}^{m+\frac{1}{2}} = D^{m+\frac{1}{2}}\overline{v}^{m+\frac{1}{2}}\Delta\xi\,.$$

$D^{m+\frac{1}{2}} = h + \zeta^{m+\frac{1}{2}}$. The free surface update,

$$\zeta^{m+1} = \zeta^{m} - \Delta t_{*}\,\mathrm{div}\overline{\mathbf{U}}^{m+\frac{1}{2}}\,, \tag{3.58}$$

is followed by an update of the momentum equations,

$$\overline{\mathbf{U}}^{m+1} = \overline{\mathbf{U}}^{m} + \Delta t_{*}\left[F(\zeta') - D'f\mathbf{k}\times\overline{\mathbf{u}}^{m+\frac{1}{2}} + \ldots\right], \tag{3.59}$$

$$\zeta' = \delta\zeta^{m+1} + (1-\delta-\gamma-\epsilon)\zeta^{m} + \gamma\zeta^{n-1} + \epsilon\zeta^{n-2}$$

utilizes the newly computed values of ζ^{m+1}. In all computations performed here we use settings $\beta = 0.281105$, $\gamma = 0.088$, $\delta = 0.614$, and $\epsilon = 0.013$. The computation of fast-time averaged barotropic variables, $\langle\zeta\rangle^{n+1}$ and $\langle\overline{\mathbf{U}}\rangle^{n+1}$, is done by (3.40) applied to (3.58)—(3.59), while the $\langle\!\langle\overline{\mathbf{U}}\rangle\!\rangle^{n+\frac{1}{2}}$ are computed by (3.47) just after the $\overline{\mathbf{U}}^{m+\frac{1}{2}}$ become available.

Since the barotropic time step is limited by the phase speed of non-rotational surface gravity waves, the efficiency of these algorithms can be predicted from a linear theory: $\alpha_{\max}\approx 2.4$ for the predictor-corrector algorithm (2.34)–(2.37), and $\alpha_{\max}\approx 1.8$ for generalized forward-backward step (2.41). In practice this translates into permissible Courant numbers (*cf.,* (2.7) and (3.51), left) of 1.2 and 0.9 respectively. Since the forward-backward step requires only one computation of the r.h.s. of each equation per time step, it is 1.5 times more efficient than the predictor-corrector algorithm in the computational cost per unit simulation time.

3.4. Choice of Filter Shape

The analytical study in Higdon & de Szoeke, 1997 reveals a probable scenario for computational instability in a split-explicit model in which the eigenvalues[13] of uncoupled baroclinic and barotropic modes coincide on the complex plane, and the perturbation due to inaccurate splitting and subsequent coupling moves some of the eigenvalues outside the unit circle. This coincidence is possible when the baroclinic mode gets a phase increment $\omega_k\Delta t$ while the barotropic mode gets $2\pi n + \omega_k\Delta t$ (*i.e.,* aliasing). Temporal filtering of the barotropic variables excludes this possibility, but, as criticized by Hallberg, 1997, it also results in additional numerical inaccuracy and requires an integration of the barotropic mode significantly beyond $n+1$ in order to place the averaged values at $n+1$. Although split-explicit models without temporal averaging of fast mode are known to exist, their numerical stability is most likely attributed to some kind of built-in dissipation. For example, our time-splitting algorithm becomes equivalent to the method of averages of Nadiga, *et al.,* 1997, if we set $\{a_m\}$ to delta function $a_m = \delta(M-m)$ instead of (3.38). That method relies on Smolarkiewicz advection scheme which is sufficiently dissipative and stable if used in combination with a forward-in-time step. Practical experience with ROMS shows that model becomes weakly unstable in the case of delta function setting. In contrast, Hallberg, 1997 uses centered spatial differencing, no time-averaging, but time-stepping algorithm designed there provide a controllable amount of dissipation through its truncation term within the second-order of accuracy. In this part we construct filters which address this criticism.

---

[13] Eigenvalues are roots of the characteristic polynomial that are also Fourier component phase multipliers corresponding to one time step of the slower (baroclinic) mode.

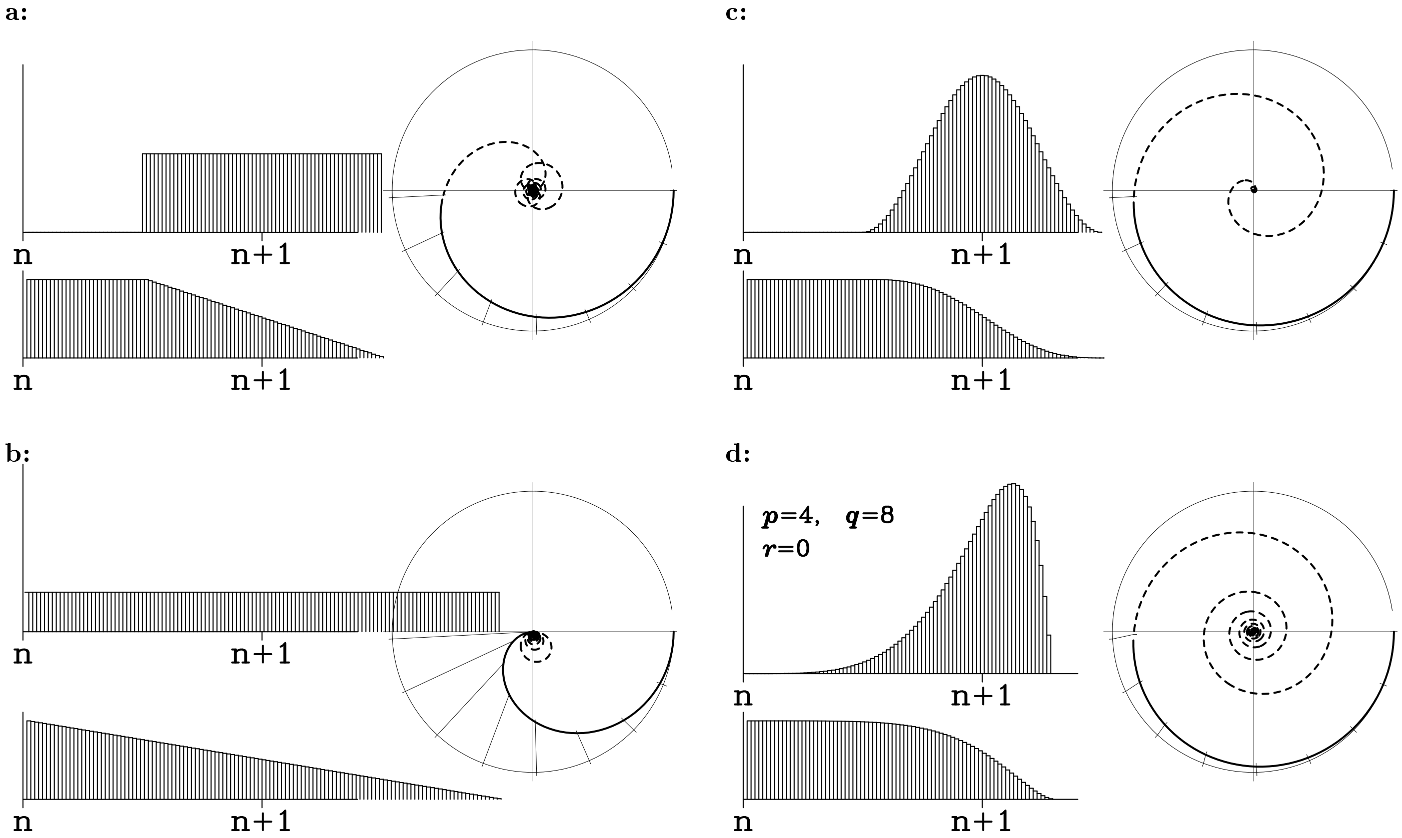

Figure 13. Comparison of different filters for the barotropic mode. Left side: **a,b** — rectangular-shape filters of different width; Right side: **c** — $\cos^2$ shape; **d** — with positive-definite weights (3.38); Left portion of each plot shows the primary and secondary weights in the format similar to Fig 12. The circle on the right side of each plot shows the complex roots for the physical mode of the filtered barotropic mode, assuming that barotropic time stepping is exact. The solid portion of the curve corresponds to the physical range where $\omega\Delta t$ is resolved by the baroclinic time step, ideally these roots should stay on the unit circle. The curve turns to dashed when entering the aliasing range — these roots must be well within the unit circle (depending on the accuracy of mode splitting for the pressure gradient) in order to prevent numerical instability.

Assuming $M \gg 1$, hence the barotropic time step is much smaller that the baroclinic, we neglect the truncation error in the barotropic time-stepping algorithm for the present analysis. Then an unfiltered Fourier component ω_k of the barotropic mode gets a phase increment $\alpha = \omega_k \Delta t$ in one baroclinic time step Δt. If the same component is subject to weighted averaging (3.40), its step multiplier is

$$\lambda(\alpha) = \int_0^{\tau_*} \mathrm{e}^{-i\alpha\cdot\tau} f(\tau)\, d\tau \,, \qquad (3.60)$$

where $f(\tau)$ is analogous of a_m, τ plays the role of m/M, and for simplicity we have replaced discrete summation with integral.

Ideally $\lambda(\alpha) = \mathrm{e}^{-i\alpha}$ for small α, and $\lambda(\alpha) \to 0$ for large α. A Taylor expansion for small α,

$$\mathrm{e}^{-i\alpha\tau} = 1 - i\alpha\tau - \frac{\alpha^2\tau^2}{2} + i\frac{\alpha^3\tau^3}{6} + \ldots$$

leads to

$$\lambda(\alpha) = 1 - i\alpha - \frac{\alpha^2}{2} I_2 + i\frac{\alpha^3}{6} I_3 + \frac{\alpha^4}{24} I_4 + \ldots \qquad (3.61)$$

where

$$I_n = \int_0^{\tau_*} \tau^n f(\tau)\, d\tau, \qquad n = 2, 3, \ldots . \qquad (3.62)$$

This takes into account that $I_0 \equiv I_1 \equiv 1$ due to the normalization and consistency conditions (3.39).

An analysis of (3.61) shows that any choice of a positive-definite shape function, $f(\tau)$, results in at most first-order

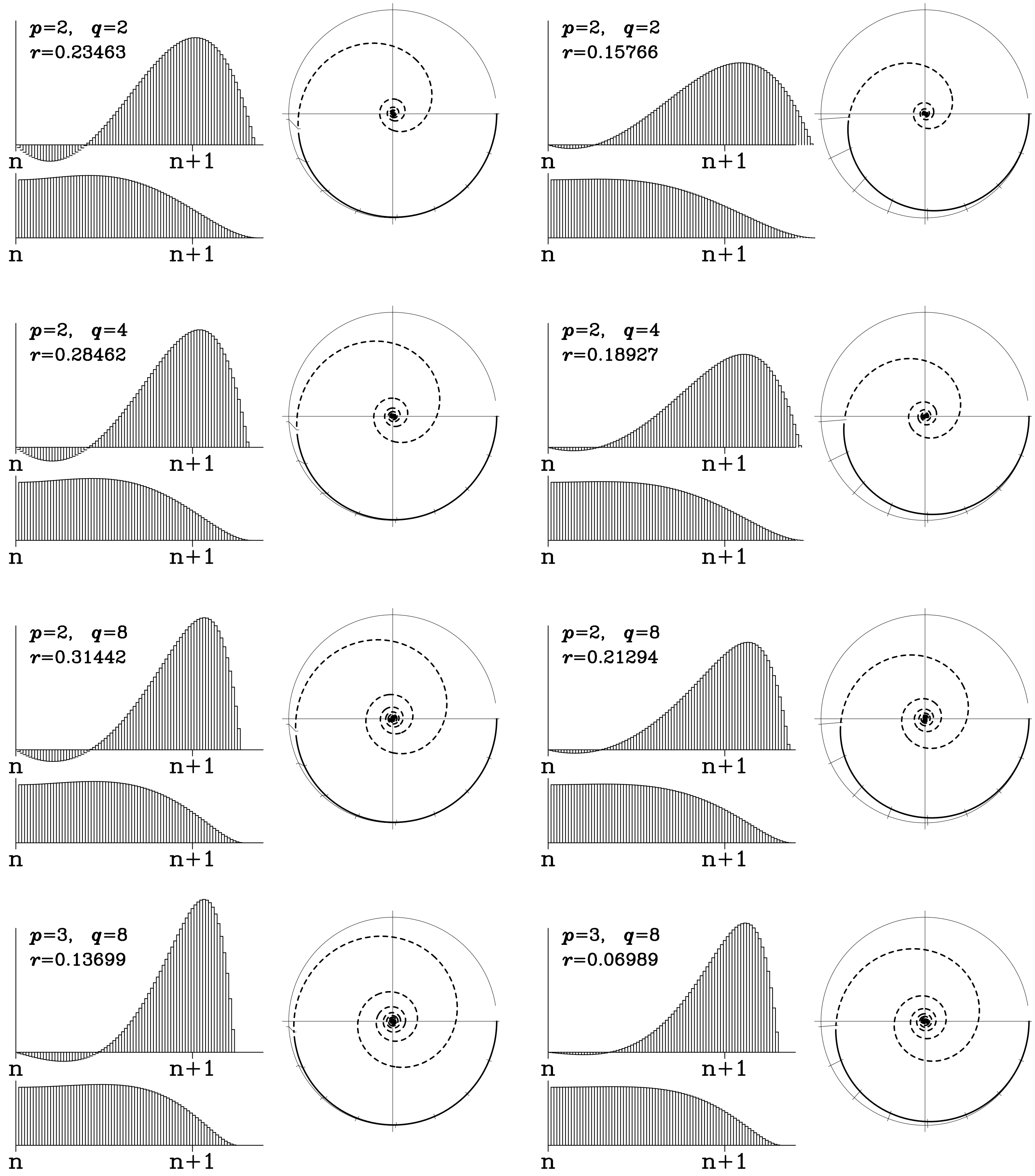

Figure 14. Shape functions and corresponding step multipliers $\lambda(\alpha)$ for filters (3.73) with different settings p, q. **Left side** — second-order accurate filters; **right side** — filters optimized for minimal numerical dispersion ((3.69)).

accuracy for the overall time stepping of the barotropic mode (*i.e.,* $\lambda(\alpha)$ agrees with $\mathrm{e}^{-i\alpha}$ only up to $\mathcal{O}\left(\alpha^2\right)$). Using the identity,

$$\tau^2 \equiv (\tau-1)^2 + 2\tau - 1\,,$$

we find that

$$I_2 = \int\limits_0^{\tau_*} (\tau-1)^2 f(\tau)\, d\tau + 2I_1 - I_0 = 1 + \epsilon\,, \tag{3.63}$$

after using $2I_1 - I_0 = 1$. Unless $f(\tau)$ is a delta-function, $\delta(\tau-1)$, the expression inside the right-side integral is positive definite, hence $\epsilon > 0$. Substitution of $I_2 = 1+\epsilon$ into (3.61) leads to the appearance of ϵ as a coefficient in the leading-order truncation term that is at the second order. The positivity of ϵ corresponds to numerical dissipation.

If (3.60) is represented as

$$\lambda(\alpha) = \mathcal{R}(\alpha)\mathrm{e}^{-i\alpha}\,, \tag{3.64}$$

where $\mathcal{R}(\alpha)$ is a real-valued function, then the resultant filter is non-dispersive (*i.e.,* it has zero phase error). The simplest way to achieve this property is to chose a shape function that is symmetric about $\tau = 1$,

$$\tau = 1 + \xi\,, \quad \text{hence} \quad f(\tau) = f(1+\xi) = f(1-\xi)\,. \tag{3.65}$$

This leads to

$$\begin{aligned} \lambda(\alpha) &= \int\limits_{-\Delta\tau}^{+\Delta\tau} \mathrm{e}^{-i\alpha(1+\xi)}\,\frac{f(1+\xi)+f(1-\xi)}{2} d\xi \qquad (3.66)\\ &= \mathrm{e}^{-i\alpha} \int\limits_{-\Delta\tau}^{+\Delta\tau} cos(\alpha\xi) f(1+\xi) d\xi = \mathcal{R}(\alpha)\mathrm{e}^{-i\alpha}, \end{aligned}$$

when we assume that $f(\tau)$ is distinct from 0 within the interval $1-\Delta\tau \le \tau \le 1+\Delta\tau$, and $\Delta\tau \le 1$.

Since for computational efficiency it is advantageous to use a non-symmetric shape function (because it shortens the extent of integral portion beyond $n+1$), we are also interested in eliminating or minimizing the leading-order dispersive term. To do so, note that any real-valued function may be represented as

$$\mathcal{R}(\alpha) = 1 - \epsilon\frac{\alpha^2}{2} + \delta\frac{\alpha^4}{24} - ..., \tag{3.67}$$

where ϵ and δ are real-valued coefficients. Then

$$\begin{aligned} \mathcal{R}(\alpha)\mathrm{e}^{-i\alpha} &= 1 - i\alpha - (1+\epsilon)\frac{\alpha^2}{2} \qquad (3.68)\\ &+ i(1+3\epsilon)\frac{\alpha^3}{6} + (1+\delta+6\epsilon)\frac{\alpha^4}{24} + \dots\,. \end{aligned}$$

In comparison with (3.61), this leads to the conclusion that

$$I_3 = 3I_2 - 2 \tag{3.69}$$

is the necessary condition to cancel out the $\mathcal{O}\left(i\alpha^3\right)$ dispersive term.

Fig. 13 shows $\lambda(\alpha)$ for several filters in common use, as well as for the filter on Fig. 12. Rectangular-shaped filters are characterized by the largest dissipation for small values of α and relatively slow, oscillatory decay for large α — in comparison with a smooth filter (*e.g.,* a $\cos^2$ shape) with rapid decay after $\alpha = 2\pi$. As inaccurate as it may appear, flat averaging over $2\Delta t$ (Fig. 13b) results in

$$\lambda(\alpha) = \frac{\sin\alpha}{\alpha} e^{-i\alpha}\,, \tag{3.70}$$

which has a truncation error comparable to that of a weighted implicit time step,

$$\begin{aligned} \zeta^{n+1} &= \zeta^n - i\alpha\left[\beta u^{n+1} + (1-\beta)u^n\right] \\ u^{n+1} &= u^n - i\alpha\left[\beta\zeta^{n+1} + (1-\beta)\zeta^n\right]\,, \end{aligned} \tag{3.71}$$

with

$$\lambda(\alpha) = \frac{1 - i\alpha - \beta(1-\beta)\alpha^2}{1+\beta^2\alpha^2}\,, \tag{3.72}$$

and $\beta = 2/3$. This means that the commonly used Backward Euler (BE) time step ($\beta = 1$) is even less accurate for an implicit free-surface model. The $\cos^2$ filter historically used in ROMS is characterized by

$$\lambda(\alpha) = \frac{\sin\frac{\alpha}{2}\cdot e^{-i\alpha}}{\frac{\alpha}{2}\left(1-\frac{\alpha^2}{4\pi^2}\right)} = e^{-i\alpha}\begin{cases} 1 - \frac{\left(\pi^2-6\right)\alpha^2}{24\pi^2}\,, & \alpha \to 0 \\ \mathcal{O}\left(1/\alpha^3\right)\,, & \alpha \to \infty \end{cases}$$

with the singularities at $\alpha = \pm 2\pi$ removable. Although still only first-order accurate, its leading-order dissipation, $\epsilon = (\pi^2-6)/(12\pi^2) \approx 0.0326$, is one-and-half orders of magnitude smaller than for the BE implicit scheme.

To improve the temporal accuracy of the filtered barotropic mode, we modify (3.38) by introducing an extra term which makes some of the weights negative,

$$f(\tau) = A\left\{\left(\frac{\tau}{\tau_0}\right)^p\left[1-\left(\frac{\tau}{\tau_0}\right)^q\right] - r\frac{\tau}{\tau_0}\right\} \tag{3.73}$$

where p, q are picked arbitrarily and A, τ_0, and r are then chosen to satisfy normalization, consistency, and second-order accuracy conditions,

$$I_n = \int\limits_0^{\tau_*} \tau^n f(\tau)\, d\tau = 1\,, \qquad n = 0, 1, 2\,, \tag{3.74}$$

via a Newton-Raphson iterative procedure. τ_* is the upper limit of τ with $f(\tau) \geq 0$). The result is shown in Fig. 14, left side. Alternatively, to targeting $I_2 = 1$, one might chose to satisfy (3.69), which minimizes numerical dispersion, right side. No choice of r eliminates both $\mathcal{O}(\alpha^2)$ and $\mathcal{O}(i\alpha^3)$ truncation terms, but the r-term reduces both of them relative to the $r = 0$ choice. Allowing negative weights in the left portion of the filter is also beneficial for computational efficiency because it shortens the overall number of barotropic time steps needed. All filters on the left side of Fig. 14 extend by no more than $\Delta t/4$ or $\Delta t/3$ beyond the baroclinic time step $n+1$. A comparison with time-stepping schemes available for an implicit free-surface model (since the implicit AM3 is only conditionally stable, these are limited to a weighted backward Euler step; *cf.,* (3.71)) shows that, with a proper choice of $f(\tau)$, the split-explicit model is inherently more accurate for time-resolved barotropic motions.

The choice of parameters p and q controls the damping of the unresolved barotropic frequencies that determine the stability and robustness of the model. A complete quantitative analysis in a manner of Higdon & de Szoeke, 1997 is beyond the scope of the present study; however, our practical experience indicates that even the sharpest ($p = 4$, $q = 8$) filters from Fig. 14 result in a stable model for our model applications without any need for explicit dissipation or viscosity in the barotropic mode.

4. A Hybrid Predictor-Corrector for the Baroclinic Time Step

Because of their mathematical similarity, the time-stepping algorithms for the baroclinic mode are generally similar to the barotropic ones. The differences arise from the necessity for a conservative and constancy-preserving algorithm for tracers. We will show this makes it necessary to update the velocities before the tracers. Similar to (3.51), the allowed time step is limited mainly by internal gravity waves, but the contrast between the two restrictions is not so dramatic. In addition, the advective Courant number is not expected to be very small. For typical oceanographic conditions, the phase speed of internal gravity waves may be 2.5 m/sec, while the advection speed may be as large as 1 m/sec. For coarse to moderate horizontal resolution, the baroclinic time step may be as large as 2 hours, which is less than an order of magnitude away from the inertial period. Although generalized FB algorithm is clear favorite for the barotropic mode, given the considerations presented here, we find that it more favorable to chose predictor-corrector approach for the baroclinic mode.

Most oceanic models use a single-step algorithm for the three-dimensional equations: either LF — MOM and its derivatives, MICOM, POM; or AB3 — SPEM/SCRUM family. This choice has two weaknesses:

(*i*) Since the temperature and salinity are responsible for the stratification, hence the pressure gradient, and since both momentum and tracer equations are advanced simultaneously for one time step, the momentum equations feel feedback from the changed tracer distribution only during the next step. Within the stiffest part of the system (*i.e.,* propagation of internal gravity waves), the even-step velocity is coupled predominantly with the odd-step tracer field, and vice versa, while the odd-odd and even-even couplings are much weaker. In fact, for a linearized system and an LF time step, these two modes are completely independent. The use of AB3 mitigates this effect, but does not eliminate it completely.

(*ii*) In a free-surface model the grid-box heights, $H^{n+1}_{i,j,k}$, are set by the barotropic mode using an entirely different time-stepping algorithm. As the result, in the case of LF it is difficult to build a conservative and constancy-preserving advection scheme for tracers, because LF advances tracer fields from step $n-1$ to step $n+1$ with tracer fluxes computed at time step n, while the discrete continuity equation (1.18) relates $H^{n+1}_{i,j,k}$ with $H^{n}_{i,j,k}$ (instead of $H^{n-1}_{i,j,k}$), and the associated mass fluxes are time-centered at $n+\frac{1}{2}$. In the case of AB3, this problem may be addressed if a forward-in-time extrapolation of the pre-computed right side for the tracer equations is replaced with an extrapolation of velocity components and a subsequent correction of their vertical averages, with a multiplication by the extrapolated tracers to compute tracer fluxes.

To make (1.16) and (1.18) consistent with their continuous prototype tracer and continuity equations, with at least second-order accuracy, the mass fluxes ($U_{i+\frac{1}{2},j,k}$, $V_{i,j+\frac{1}{2},k}$, $W_{i,j,k+\frac{1}{2}}$) and interfacial tracer values ($\widetilde{q}_{i+\frac{1}{2},j,k}$, $\widetilde{q}_{i,j+\frac{1}{2},k}$, and $\widetilde{q}_{i,j,k+\frac{1}{2}}$) must be time-centered at $n+\frac{1}{2}$. Hence (1.16) becomes

$$H^{n+1}_{i,j,k}\Delta\mathcal{A}_{i,j} = H^{n}_{i,j,k}\Delta\mathcal{A}_{i,j} - \Delta t\Big[U^{n+\frac{1}{2}}_{i+\frac{1}{2},j,k} - U^{n+\frac{1}{2}}_{i-\frac{1}{2},j,k} + V^{n+\frac{1}{2}}_{i,j+\frac{1}{2},k} - V^{n+\frac{1}{2}}_{i,j-\frac{1}{2},k} + W^{n+\frac{1}{2}}_{i,j,k+\frac{1}{2}} - W^{n+\frac{1}{2}}_{i,j,k-\frac{1}{2}}\Big]\,, \tag{4.1}$$

and (1.18) turns into

$$q^{n+1}_{i,j,k} = \left\{ q^{n}_{i,j,k}H^{n}_{i,j,k} - \frac{\Delta t}{\Delta\mathcal{A}_{i,j}}\left[\widetilde{q}^{\,n+\frac{1}{2}}_{i+\frac{1}{2},j,k}U^{n+\frac{1}{2}}_{i+\frac{1}{2},j,k} - \widetilde{q}^{\,n+\frac{1}{2}}_{i-\frac{1}{2},j,k}U^{n+\frac{1}{2}}_{i-\frac{1}{2},j,k} + \widetilde{q}^{\,n+\frac{1}{2}}_{i,j+\frac{1}{2},k}V^{n+\frac{1}{2}}_{i,j+\frac{1}{2},k} - \widetilde{q}^{\,n+\frac{1}{2}}_{i,j-\frac{1}{2},k}V^{n+\frac{1}{2}}_{i,j-\frac{1}{2},k} + \widetilde{q}^{\,n+\frac{1}{2}}_{i,j,k+\frac{1}{2}}W^{n+\frac{1}{2}}_{i,j,k+\frac{1}{2}} - \widetilde{q}^{\,n+\frac{1}{2}}_{i,j,k-\frac{1}{2}}W^{n+\frac{1}{2}}_{i,j,k-\frac{1}{2}}\right]\right\} \Big/ H^{n+1}_{i,j,k}\,. \tag{4.2}$$

Here (4.1) is not to be interpreted as a method for computing $H^{n+1}_{i,j,k}$, but rather as a constraint imposed on the set of mass fluxes, ($U^{n+\frac{1}{2}}$, $V^{n+\frac{1}{2}}$, $W^{n+\frac{1}{2}}$), satisfied by enforcing that the vertical integrals of ($U^{n+\frac{1}{2}}$, $V^{n+\frac{1}{2}}$) are equal to ($\langle\!\langle\overline{U}\rangle\!\rangle^{n+\frac{1}{2}}$, $\langle\!\langle\overline{V}\rangle\!\rangle^{n+\frac{1}{2}}$) defined by (3.47). Once this is satisfied, building a tracer advection scheme is just a matter of spatial interpolation of tracer variables to compute interfacial values and of temporal extrapolation/interpolation to $n+\frac{1}{2}$ to achieve at least second-order accuracy and maintain numerical stability. This can be accomplished by four possible methods:

The **first** option is to extrapolate q forward in time before doing the spatial interpolation using a second- or third-order accurate Adams-Bashforth extrapolation rule for the right hand side,

$$q^{n+\frac{1}{2}}_{i,j,k} = \left(\frac{3}{2}+\beta\right) q^{n}_{i,j,k} - \left(\frac{1}{2}+2\beta\right) q^{n-1}_{i,j,k} + \beta q^{n-2}_{i,j,k}\ , \quad (4.3)$$

where $\beta = 0$ yields AB2, $\beta = 5/12$ AB3, or any intermediate value (Appendix A). This is preceded by a similar AB3-like update for the velocity field, so that velocities at $n+1$ participate in interpolation to compute mass fluxes at $n+\frac{1}{2}$ as in (2.41), except that now ζ and u switch roles.

The **second** option is that, instead of using local grid points in the previous time steps, one designs an UTOPIA or COSMIC-like algorithm (Leonard *et al.*, 1996). There is no need for forward extrapolation in time, since only tracer values at time step n are used. This is potentially the most accurate approach because it uses a more compact stencil, and by its design the dispersive errors of time and space differencing compensate each other. However, the resultant schemes are unavoidably upstream-biased in all three spatial directions. This is undesirable for long-term simulations because of its vertical hyper-diffusion in the leading order truncation term. This causes excessive artificial diapycnal mixing if temporal oscillations are present in vertical velocity field — a very common in oceanic models. This algorithm is a single-step method, but its operational complexity is similar to a predictor-corrector's: since a fully three-dimensional UTOPIA algorithm is impractical, COSMIC is the most likely candidate. This algorithm includes computation of multi-dimensional finite-volume fluxes in each direction via successive one-dimensional, non-conservative, advective updates in both transverse directions to get provisional tracer fields, after which the one-dimensional QUICKEST algorithm is applied to compute fluxes.

The **third** approach is to construct an auxiliary non-conservative, advective-form, predictor time step to compute the provisional field $q^{n+\frac{1}{2}}$. The motivation for a non-conservative algorithm comes from the fact that the $q^{n+\frac{1}{2}}$ are used only for the computation of fluxes in (4.2). Furthermore, a set of mass fluxes satisfying (4.1) exists only between time steps n and $n+1$, so a conservative predictor substep cannot be made constancy preserving; therefore, the resultant predictor-corrector algorithm will not be constancy preserving either. A centered scheme for spatial derivatives in combination with an LF time step can be used for the predictor step,

$$q^{n+1,*}_{i,j,k} = q^{n-1}_{i,j,k} - 2\Delta t\left[\overline{u\delta_\xi q}^{\xi} + \overline{v\delta_\eta q}^{\eta} + \overline{w\delta_z q}^{z}\right]\Bigg|^{n}_{i,j,k}\ , \quad (4.4)$$

where symbols δ and overline denote differencing and interpolation in the direction designated by their sub- and superscripts (in principle, these operators can be higher-than-second order accurate); u, v, and w are velocity components computed from interface fluxes $U^{n}_{i+\frac{1}{2},j,k}$, $V^{n}_{i,j+\frac{1}{2},k}$ and $W^{n}_{i,j,k+\frac{1}{2}}$. Once $q^{n+1,*}$ become available, $q^{n+\frac{1}{2}}$ is computed using a three-point interpolation,

$$q^{n+\frac{1}{2}}_{i,j,k} = \left(\frac{1}{2}-\gamma\right) q^{n+1,*}_{i,j,k} + \left(\frac{1}{2}+2\gamma\right) q^{n}_{i,j,k} - \gamma q^{n-1}_{i,j,k}\ . \quad (4.5)$$

after which a high-order, spatial-interpolation scheme (described below) is used to compute the interfacial flux values $\widetilde{q}^{\,n+\frac{1}{2}}_{i+\frac{1}{2},j,k}$, $\widetilde{q}^{\,n+\frac{1}{2}}_{i,j+\frac{1}{2},k}$, $\widetilde{q}^{\,n+\frac{1}{2}}_{i,j,k+\frac{1}{2}}$ in (4.2). Since the provisional $q^{n+1,*}$ is needed only to compute $q^{n+\frac{1}{2}}$, operations (4.4) and (4.5) can be combined into a single step,

$$\begin{aligned} q^{n+\frac{1}{2}}_{i,j,k} = {} & \left(\frac{1}{2}+2\gamma\right) q^{n}_{i,j,k} + \left(\frac{1}{2}-2\gamma\right) q^{n-1}_{i,j,k} \qquad (4.6) \\ & - (1-2\gamma)\,\Delta t\Big[\text{same as in (4.4)}\Big]\ . \end{aligned}$$

The resultant combination of (4.6) and (4.2) is overall similar to LF-AM3 (with setting $\gamma = 1/12$) or LF-TR ($\gamma = 0$) predictor-corrector time step, *cf.*, (2.34)—(2.37) and Fig. 6.

The **fourth** method is similar to the third, except that instead of using the advective form of the tracer equation, the predictor step employs a *pseudo-compressible* algorithm to achieve constancy preservation. In this approach we compute two auxiliary grid-box height fields $H^{-}_{i,j,k}$ and $H^{+}_{i,j,k}$ by stepping it back and forward in time,

$$\begin{aligned} H^{\pm}_{i,j,k} = H^{n}_{i,j,k} \mp \left(\frac{1}{2}-\gamma\right)\frac{\Delta t}{\Delta\mathcal{A}_{i,j}}\Big[& U^{n}_{i+\frac{1}{2},j,k} - U^{n}_{i-\frac{1}{2},j,k} \qquad (4.7) \\ & + V^{n}_{i,j+\frac{1}{2},k} - V^{n}_{i,j-\frac{1}{2},k} + W^{n}_{i,j,k+\frac{1}{2}} - W^{n}_{i,j,k-\frac{1}{2}}\Big]\ , \end{aligned}$$

and perform a flux-divergent update of tracer field q using LF step combined with three-point interpolation, *cf.*, (2.34) and (3.52),

$$q^{n+\frac{1}{2}}_{i,j,k} = \left\{\left[\left(\frac{1}{2}+2\gamma\right) q^{n}_{i,j,k} + \left(\frac{1}{2}-2\gamma\right) q^{n-1}_{i,j,k}\right] H^{-}_{i,j,k}\right.$$

$$\begin{aligned}-\frac{(1-2\gamma)\,\Delta t}{\Delta\mathcal{A}_{i,j}}\cdot\Big[&\widetilde{q}^{\,n}_{i+\frac12,j,k}U^n_{i+\frac12,j,k}-\widetilde{q}^{\,n}_{i-\frac12,j,k}U^n_{i-\frac12,j,k}\\ &+\widetilde{q}^{\,n}_{i,j+\frac12,k}V^n_{i,j+\frac12,k}-\widetilde{q}^{\,n}_{i,j-\frac12,k}V^n_{i,j-\frac12,k}\\ &+\widetilde{q}^{\,n}_{i,j,k+\frac12}W^n_{i,j,k+\frac12}-\widetilde{q}^{\,n}_{i,j,k-\frac12}W^n_{i,j,k-\frac12}\Big]\Big\}\Big/\,H^+_{i,j,k}\,.\end{aligned}\tag{4.8}$$

after which $H^-_{i,j,k}$ and $H^+_{i,j,k}$ are discarded and do not participate in any further computation.

By the construction of (4.7)–(4.8) the constancy preservation property is clear: if $q^{n-1}\equiv q^n\equiv\text{const}$, then $q^{n+\frac12}$ assumes the same constant value, regardless of the divergence of mass fluxes $U^n_{i+\frac12,j,k}$, $V^n_{i,j+\frac12,k}$, and $W^n_{i,j,k+\frac12}$. However, since H^+ and H^+ have no relation with the actual grid-box height field by the barotropic mode, this update is not conservative. For example, neither

$$H^+_{i,j,k}\neq\frac{H^{n+1}_{i,j,k}+H^n_{i,j,k}}{2}$$

nor

$$H^+_{i,j,k}\neq\left(\frac12-\gamma\right)H^{n+1}_{i,j,k}+\left(\frac12+\gamma\right)H^n_{i,j,k}$$

where $H^{n+1}_{i,j,k}$ is determined from $\langle\zeta\rangle^{n+1}_{i,j}$ via (1.11). In fact, the use of artificial divergence equation (4.7) just provides a way of "trading in" the conservation property in favor of constancy preservation, following the continuous identity

$$\nabla\left(q\mathbf{u}\right)=\left(\mathbf{u}\cdot\nabla q\right)+q\nabla\mathbf{u}\tag{4.9}$$

and dropping the last term. At the same time, pseudo-compressible time step is numerically similar to the conservative update during corrector sub-step, and therefore is preferred over the advective form (4.4).

Once tracer concentration is available at proper time, either n or $n+\frac12$, it needs to be interpolated to grid-box interfaces to compute tracer fluxes. Three options are available in ROMS for doing so: either a centered, fourth-order-accurate interpolation (*cf.,* Dietrich *et al.*, 1997),

$$\widetilde{q}_{i+\frac12,j,k}=\frac{-q_{i-1,j,k}+7q_{i,j,k}+7q_{i+1,j,k}-q_{i+2,j,k}}{12}\,,\tag{4.10}$$

which can be expressed as mid-point average enhanced by curvature term,

$$\widetilde{q}_{i+\frac12,j,k}=\frac{q_{i,j,k}+q_{i+1,j,k}}{2}-\frac{\overline{\delta q}_{i+1,j,k}-\overline{\delta q}_{i,j,k}}{6}\tag{4.11}$$

where $\overline{\delta q}_{i,j,k}$ and $\overline{\delta q}_{i+1,j,k}$ are averaged elementary differences,

$$\overline{\delta q}_{i,j,k}=\frac{\delta q_{i-\frac12,j,k}+\delta q_{i+\frac12,j,k}}{2}\,,\tag{4.12}$$

and $\delta q_{i+\frac12,j,k}=q_{i+1,j,k}-q_{i,j,k}$. Alternatively (4.12) is replaced with harmonic averaging (*cf.,* Shchepetkin & McWilliams, 2003),

$$\overline{\delta q}_{i,j,k}=\frac{2\delta q_{i+\frac12,j,k}\delta q_{i-\frac12,j,k}}{\delta q_{i+\frac12,j,k}+\delta q_{i-\frac12,j,k}}\tag{4.13}$$

as long as $\delta q_{i+\frac12,j,k}$ and $\delta q_{i-\frac12,j,k}$ have the same sign, and $\overline{\delta q}_{i,j,k}=0$ the signs are different. In this case (4.11) has the property that interpolated value $\widetilde{q}_{i+\frac12,j,k}$ is bounded by values at the two nearest neighboring points, $q_{i,j,k}$ and $q_{i+1,j,k}$, regardless of values at the two extreme points of the stencil. Although this measure by itself does not strictly guarantee monotonicity preservation for the whole advection scheme (because time stepping is done independently from spatial discretization), it is capable to reduce spurious oscillations in the case of non-smooth advected fields. The third option is an upstream-biased, parabolic interpolation,

$$\widetilde{q}_{i+\frac12,j,k}=\frac{q_{i,j,k}+q_{i+1,j,k}}{2}-\frac16\cdot\begin{cases}q''_{i,j,k}\,, & u_{i+\frac12,j,k}>0\\[6pt] q''_{i+1,j,k}\,, & u_{i+\frac12,j,k}<0\end{cases}$$

where

$$q''_{i,j,k}=q_{i+1,j,k}-2q_{i,j,k}+q_{i-1,j,k}\,,$$

which results in a dissipatively dominant (*i.e.,* hyper-diffusive) truncation error and the overall performance of the advection scheme is similar to that reported in Farrow & Stevens, 1995. Vertical interpolation is done using either a centered fourth-order scheme or, more preferably, an interpolation based on conservative parabolic splines as in (3.16) (Fig. 11; Appendix B). Use of an upstream-biased scheme in the vertical direction is avoided for the reasons mentioned above.

Time stepping of the momentum equations follow the same strategy as above: non-conservative (pseudo-compressible) predictor substep followed by conservative corrector. Spatial discretization of the advective and Coriolis terms generally follows the framework of Lilly, 1965, Mesinger & Arakawa, 1976 adapted for curvilinear horizontal grids (in essence this is done in POM, Blumberg & Mellor, 1987; and SCRUM, Song & Haidvogel, 1994), with the exception that mid-point averaging is replaced with higher order interpolations: third- (upstream-biased) or fourth-order (centered) schemes are applied for horizontal directions and fourth-order or parabolic splines in vertical.

5. Time Stepping the Coupled Baroclinic-Barotropic System

We now summarize the time-stepping engine of ROMS, focusing on the interplay between the modes in discrete time. Two versions — the predictor- and corrector-coupled algorithms — have been developed. As indicated by their names, they differ by the stage at which barotropic mode is advanced in time. They are approximately equivalent in their efficiency and stability.

5.1. Predictor-Coupled Algorithm (Fig. 15, Left)

Stage 1: Compute the r.h.s. (*i.e.,* pressure-gradient, Coriolis, and advective terms) for the 3D baroclinic-mode momentum equations at time step n and vertically integrate them. (These integrals will be later converted into forcing terms for the barotropic mode; *i.e., forward coupling*). Also compute and store the vertically averaged densities, ($\overline{\rho}_i$, ρ_i^*), by (3.23)–(3.24). Apply the r.h.s. terms to advance the 3D momenta using a LF step combined with a half-step, backward interpolation with AM3-like coefficients. (The result is time-centered at $n+\frac{1}{2}$.) Because at this moment no meaningful values of H^{n+1} are available and it is impossible to satisfy exactly the discrete continuity equation, use the artificial continuity equation (*i.e.,* the pseudo-compressible algorithm). Compute the 3D lateral viscosity terms and add their vertical integrals to the forcing term for barotropic r.h.s. However, instead of applying the 3D viscous terms immediately at this time to advance the momentum equations, save them into provisional arrays for later use during the corrector step. At this stage the predictor step is not fully complete because it violates CFL for the barotropic mode and no meaningful vertically integrated mass fluxes are available.

Stage 2: Advance the tracer variables in a similar manner with a pseudo-compressible LF step combined with an AM3 interpolation, resulting in tracer values at $n+\frac{1}{2}$). This algorithm is constancy preserving, but not conservative. This is acceptable because the resultant tracer values at $n+\frac{1}{2}$ are used only for computation of advective fluxes during the subsequent corrector step[14].

Stage 3: Compute the r.h.s. terms for the barotropic mode from barotropic variables using (3.33) for the pressure gradient and subtract it from the corresponding vertical integrals of the 3D r.h.s. computed in Stage 1 (*i.e.,* convert them into baroclinic-to-barotropic forcing terms)[15]. Next, using similar terms stored from the previous baroclinic steps, extrapolate the forcing terms a half-step forward in time using modified AB3 coefficients (Appendix A) so that the result is time-centered at $n+\frac{1}{2}$. Advance the barotropic variables by M_* time steps (slightly beyond the baroclinic time step $n+1$, depending on the shape of the fast-time filter), performing a 2-way, fast-time averaging of barotropic variables on the way. The baroclinic forcing terms are kept constant during this procedure, but the barotropic pressure-gradient terms are recomputed by (3.33) with participation of $\overline{\rho}_i$ and ρ_i^* at every barotropic step. Once this is complete, update the vertical coordinate system, H^{n+1}, to be consistent with $\overline{\zeta}^{n+1}$.

Stage 4: Finalize the computation of the 3D momenta started in Stage 1 by setting the vertical average to $\overline{\mathbf{U}}^{n+\frac{1}{2}}$ from the barotropic mode.

Stage 5: Compute the r.h.s. terms for the 3D momentum equations at $n+\frac{1}{2}$ using the available tracer fields for density and pressure gradient. Add in the 3D lateral viscosity terms saved from Stage 1. Advance the 3D momenta to $n+1$ using a conservative step (recall that correct values of H^n and H^{n+1} are available now and the discrete continuity equation is satisfied exactly between time steps n and $n+1$). Set the vertical average of the 3D momenta to $\overline{\mathbf{U}}^{n+1}$ from the barotropic mode (*i.e., backward coupling*). The computation of 3D momenta at $n+1$ is now complete.

Stage 6: Interpolate the 3D velocity components back in time to $n+\frac{1}{2}$ using a combination of the new-time-step values (from Stage 5), values from the predictor step (Stage 4), and the old-time step values. (This introduces forward-backward feedback between the momentum and tracer equations as in (2.34)-(2.37) but with the roles of u and ζ switched.) Set the vertical average of the resultant fields to $\overline{\mathbf{U}}^{n+\frac{1}{2}}$. Use the resultant velocity field and tracers at $n+\frac{1}{2}$ to compute the tracer fluxes and advance the tracers to $n+1$. This step is both conservative and constancy preserving.

5.2. Corrector-Coupled Algorithm (Fig. 15, Right)

Stage 1: Compute the r.h.s. (pressure-gradient, Coriolis, and advection terms) for the 3D (baroclinic) momentum equations at time step n and advance the 3D momenta using a LF step combined with a half-step, backward interpolation with AM3-like coefficients in a pseudo-compressible algorithm based on the artificial continuity equation. (The result is time-centered at $n+\frac{1}{2}$.) This is similar to Stage 1 of the predictor-coupled scheme with the exceptions that no viscous terms are computed at this time, and, once the stage is complete, the vertically averaged momenta are set back to $\overline{\mathbf{U}}^n$ from time step n.

---

[14] The same comment applies to the predictor update for the momentum equations at Stage 1.

[15] There is no need to compute the $F^{(0)}$-part of the barotropic pressure gradient defined by (3.29) because it is already accounted for in the vertical integral of the three-dimensional r.h.s. Since it does not depend on ζ (hence it remains constant during barotropic time stepping) and because of the "add-subtract" procedure for baroclinic-to-barotropic forcing, this term identically cancels out when the forcing terms are added back to the barotropic r.h.s.

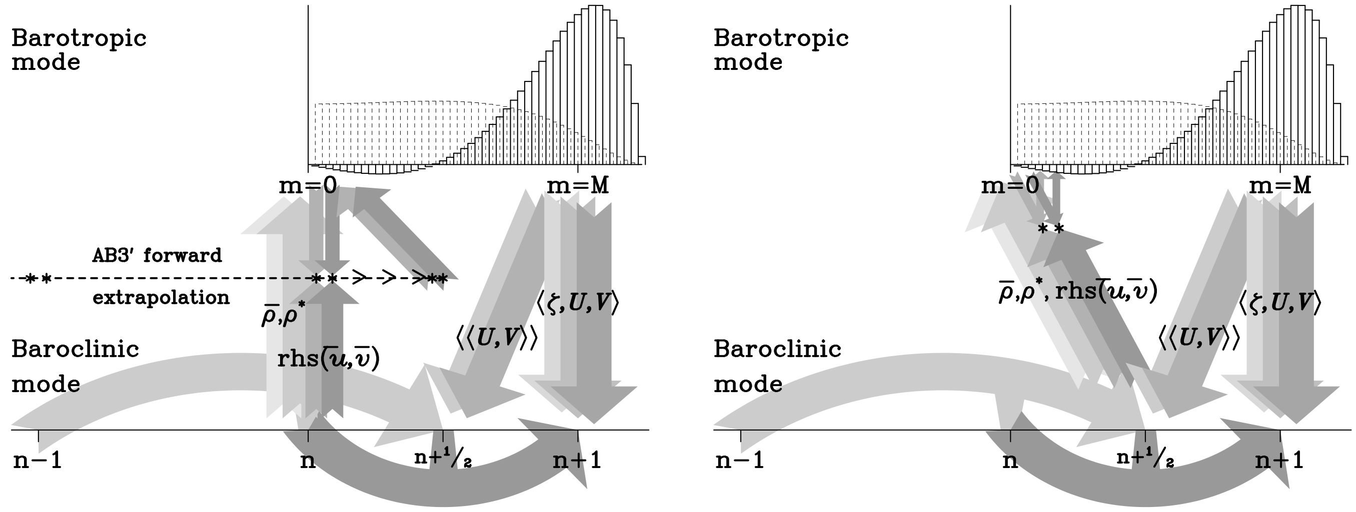

Figure 15. Barotropic-baroclinic mode data exchange in ROMS: **left** — predictor-coupled version, **right** — corrector-coupled. Curved horizontal arrows symbolize the predictor sub-step (LF step integrated with AM3 half-step-back interpolation of the result, light shading) and corrector (darker). Four ascending arrows denote 2-way vertically averaged densities $\overline{\rho}$, ρ^*, and vertically integrated right side for 3D momentum equations [these are met with the right side computed from barotropic variables; hence asterisks (*** ***) symbolize computation of baroclinic-to-barotropic forcing terms that are extrapolated forward in time using modified AB3 weights (predictor-coupled version only)]. Five descending arrows symbolize 2-way, fast-time-averaged barotropic variables for backward coupling. Each arrow originates at the time when the data is logically available, regardless of the temporal placement of the corresponding variable.

Stage 2: Advance tracer variables to $n+\frac{1}{2}$ (the same as in the predictor-coupled version).

Stage 3: Compute the r.h.s. for the 3D momentum equations (*i.e.,* pressure-gradient, Coriolis, and advective terms) from the momenta and tracers (via density) at $n+\frac{1}{2}$ and the lateral viscosity terms from the old-step velocities, $\mathbf{u}^n$. Vertically integrate everything and also compute and store vertically averaged densities, $(\overline{\rho}_i, \rho_i^*)$ with (3.23)-(3.24) time-centered at $n+\frac{1}{2}$. Apply the r.h.s. to the 3D momentum variables, but do not finalize the time step yet since H^{n+1} and $\overline{\mathbf{U}}^{n+1}$ are not available yet.

Stage 4: Compute the r.h.s. terms for the barotropic mode from barotropic variables, then convert vertical integrals from Stage 3 into baroclinic-to-barotropic forcing terms. (This procedure is similar to Stage 3 of the predictor-coupled version, with the exception that the forcing terms are already time-centered at $n+\frac{1}{2}$, hence no forward extrapolation is needed at this time.) Then advance the barotropic variables by M_* time steps, performing 2-way, fast-time averaging. Update the vertical coordinate system, H^{n+1}, to be consistent with $\overline{\zeta}^{n+1}$.

Stage 5: Finalize the computation of the 3D momenta started in Stage 3 using the now available H^{n+1}, and set the vertical average to $\overline{\mathbf{U}}^{n+1}$ from the barotropic mode.

Stage 6: Interpolate 3D velocities back in time to $n+\frac{1}{2}$ in the same way as in Stage 6 in the predictor-coupled version and set its vertical average to $\overline{\mathbf{U}}^{n+\frac{1}{2}}$. Use the resultant velocity field to compute tracer fluxes and advance tracers to $n+1$.

6. Conclusions

We have designed a robust computational kernel for a split-explicit, terrain-following-coordinate oceanic model. It includes the following features:

(*i*) Time-stepping schemes with forward-backward feedback between the variable pairs that combine an extended range of stability with the temporal accuracy of the best known algorithms (in effect, generalizing a forward-backward scheme to higher orders of accuracy);

(*ii*) A redefined formulation of the barotropic mode that takes into account the non-uniform density field to reduce the mode-splitting error (in essence, an adaptation of Higdon & de Szoeke, 1997 to terrain-following coordinates);

(*iii*) Simultaneous conservation and constancy preservation properties for tracer equations in combination with the evolving coordinate system due to changes in free-surface elevation;

(*iv*) A temporal weighted averaging of the barotropic mode

Configuration	Grid Size	Resolution *deg* or *km*	Time Step *sec*	Mode Splitting Ratio	Primary Time Step Limitation by
Atlantic DAMEE	$128 \times 128 \times 20$	0.75^0	8640	60 (Gen. FB)	Coriolis force
Atlantic DAMEE	$256 \times 256 \times 20$	0.375^0	5760	92 (Gen. FB)	Coriolis/internal
Pacific	$384 \times 224 \times 20$	0.5^0	7200	60 (LF-TR)	Coriolis force
US West Coast	$83 \times 168 \times 20$	15 *km*	2880	50 (LF-TR)	internal waves
US West Coast	$126 \times 254 \times 20$	10 *km*	2160	60 (LF-TR)	internal waves
Monterey Bay	$93 \times 189 \times 20$	5 *km*	960	60 (LF-TR)	internal waves

Table 1. Permissible time step sizes and mode splitting ratios for several practical applications of ROMS. (Gen. FB) and (LF-TR) in the column Mode Splitting Ratio indicate type of time stepping algorithm for barotropic mode.

that allows an accurate representation of the barotropic motions resolved by the baroclinic time step (*e.g.,* tides and barotropic Rossby waves); and

(*v*) Treatment of computationally expensive processes that are not critical for numerical stability (*e.g.,* viscosity, diffusion, and vertical mixing parameterizations) outside the main predictor-corrector procedure to mitigate their computational cost.

Built around this kernel, the ROMS model was applied to several oceanographic studies on basin-scale and coastal configurations (Haidvogel *et al.*, 2000, Marchesiello *et al.*, 2003) and has been verified to allow time step sizes and mode splitting ratios summarized in Table 1 for these configurations. As follows from the table, ROMS allows significant increase of time step relatively to its prototypes (SCRUM/SPEM, and POM), as well as known z-(MOM,POP) and isopycnic-coordinate (MICOM) models, which use more simpler (single step, synchronous, mostly LF; AB3 (SCRUM only)) time stepping algorithms. Furthermore, our analysis and practical experience indicate that this gain is achieved without major increase of computational cost due to the introduction of predictor-corrector algorithm, in part because most of the computationally expensive processes are still computed only once per time step (item (*v*) above). Neither we observe any degradation in quality of our solutions due to increased time step and running the model in computational regimes close to theoretical limits of stability.

Acknowledgements This study was supported by grants N00014-02-1-0236 from the Office of Naval Research.

Appendix A: Simple Time-Stepping Algorithms

One of the most commonly used time-stepping algorithms is Leap-Frog (LF) accompanied by an Asselin filter (Asselin, 1972). In the context of (2.3), it may be written as

$$q^{n+1,*} = q^{n-1} - 2i\alpha \cdot q^{n,*} \,, \tag{A.1}$$

followed by

$$q^{n} = \epsilon q^{n+1,*} + (1-2\epsilon) q^{n,*} + \epsilon q^{n-1} \,, \tag{A.2}$$

where $\alpha \equiv \omega \Delta t$; $q^{n+1,*}$ and $q^{n,*}$ are "preliminary" values of q^{n+1} and q^{n}; $\epsilon \geq 0$ is an adjustable parameter. Substitution of $q^{n+1,*}$ from (A.1) into (A.2) yields

$$q^{n} = (1 - 2\epsilon - 2\epsilon i\alpha) q^{n,*} + 2\epsilon q^{n-1}. \tag{A.3}$$

This can be rewritten as

$$q^{n,*} = \frac{q^{n} - 2\epsilon q^{n-1}}{1 - 2\epsilon - 2\epsilon i\alpha} \,. \tag{A.4}$$

Since a similar relationship exists between $q^{n+1,*}$ and q^{n+1}, one can exclude "preliminary" variables from (A.1),

$$\frac{q^{n+1} - 2\epsilon q^{n}}{1 - 2\epsilon - 2\epsilon i\alpha} = q^{n-1} - 2i\alpha \cdot \frac{q^{n} - 2\epsilon q^{n-1}}{1 - 2\epsilon - 2\epsilon i\alpha}, \tag{A.5}$$

and further rewrite it as

$$q^{n+1} = (1-2\epsilon)\, q^{n-1} + 2\epsilon q^{n} - 2i\alpha \left(q^{n} - \epsilon q^{n-1}\right) \tag{A.6}$$

(*i.e.*, a single-step version of (A.1)-(A.2)). This leads to a characteristic equation,

$$\lambda^2 + 2(i\alpha - \epsilon)\lambda - 1 + 2\epsilon(1 - i\alpha) = 0, \tag{A.7}$$

with roots (*cf.,* (12) in Asselin, 1972),

$$\lambda_{\pm} = -i\alpha + \epsilon \pm \sqrt{(1-\epsilon)^2 - \alpha^2} \,, \tag{A.8}$$

and the stability limit,

$$|\alpha_{\max}(\epsilon)| = 1/\sqrt{1 + 2\epsilon - \epsilon^2} \approx 1 - \epsilon \,. \tag{A.9}$$

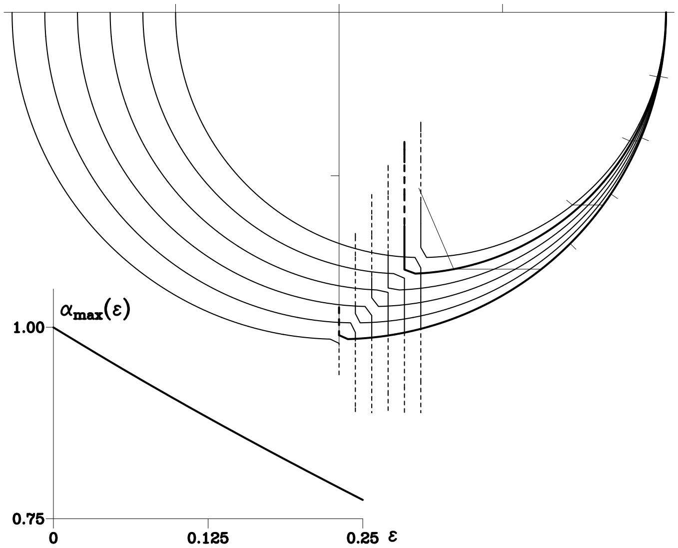

Figure 16. Complex roots for LF-Asselin Filter time-stepping algorithm for $\epsilon = 0, 0.05, 0.1, 0.15, 0.2, 0.25$. The curves corresponding to $\epsilon = 0$, and 0.2 are highlighted. The presense of ϵ terms in (A.8)"moves" roots strictly along the real axis relative to unfiltered LF roots (recall ϵ does not affect the imaginary part of $\lambda_\pm$ as long as the expression under the radical is positive). Because of this feature, an Asselin filter causes additional phase-lead error to an already forward-dispersive LF. The lower-left portion shows dependency of the stability limit $\alpha_{\max}$ on ϵ (*cf.,* (A.9)).

This approximation is valid for $\epsilon \ll 1$. Taylor series analysis of (A.6) leads to a modified equation ,

$$\frac{\partial q}{\partial t} = -i\omega q - \frac{\epsilon \Delta t \omega^2\, q}{2 - 2\epsilon + \epsilon i\omega\Delta t} + \mathcal{O}\left((\omega\Delta t)^2\right) \,, \quad \text{(A.10)}$$

indicating that the formal order of accuracy drops to the first, if $\epsilon > 0$, and that the leading-order truncation term is dissipative. An Asselin filter introduces the desired damping of the LF computational mode at the expense of a reduced stability range, some dissipation of the physical mode, and a further increase of phase-lead error of already strongly dispersive LF (Fig. 16); *e.g.,* for $\alpha = \frac{\pi}{4}$ and a typically used value of $\epsilon = 0.1$, an Asselin filter almost doubles the LF phase error.

The properties of a LF–Asselin filter time step are well known, which stimulates the search for alternatives. Durran, 1991, provides a comprehensive review of the wide collection of commonly used time-stepping algorithms for the first-order hyperbolic problem (2.1). This analysis includes Taylor series expansions for both phase and amplitude errors, so it is redundant to repeat it here. However, it is illustrative to trace the location of the amplification factors on the complex plane since this gives information about the limits for each method; the usual analysis of truncation error based on Taylor series expansion does not provide this information. The results are shown in Fig. 17. Even a brief glance at this figure indicates the existence of a variety of algorithms potentially more attractive than a LF-Asselin filter. It also shows that Runge-Kutta and predictor-corrector methods are generally more accurate than single-step methods. They also require more computational effort because the right side is to be computed more than once per time step. In fact, these types of algorithms can be viewed as combinations of simple single-stage methods arranged in such a way that the leading-order truncation errors of subsequent stages tend to cancel each other (*cf.,* an early work exploring this principle, Hyman, 1979.) In some cases it may be more efficient and more accurate to use a single-step method with a smaller time step. To make the comparison fair, we introduce a modified amplification factor that accounts for the number of right-side computations:

$$\lambda'(\omega\Delta t) = \Big(\lambda\big(r\cdot\omega\Delta t\big)\Big)^{1/r}. \qquad \text{(A.11)}$$

r is the number of right-side computations (r=1 for single-step; r=2 for predictor-corrector methods; r=3,4 for RK3 and RK4 respectively): hence λ' is the "averaged" amplification factor per right-side computation.

The results are shown of Fig. 18. This comparison shows that AB3 and LF-AM3 offer the best accuracy per computational cost, leaving RK4 and LF-TR behind. RK4 is definitely the most accurate if $\omega\Delta t < \frac{\pi}{16}$, but it rapidly departs from the unit circle when $\omega\Delta t > \frac{\pi}{8}$. AB3 and LF-AM3 are less dissipative than RK4 and LF-TR in the vicinity of $\omega\Delta t = \pi/8$, with LF-AM3 having somewhat larger phase-lead error than AB3. Finally, none of these algorithms is accurate if used in a computational regime requiring less than 10 right-side computations per period of physical oscillation. LF (not shown here) has a smaller phase error than LF-AM3 if both are used in the computational regimes close to their limits of stability, but it lacks third-order accuracy, resulting in a noticeable phase-lead error for well resolved frequencies. As a rule of thumb, one may conclude that that $\omega\Delta t \approx 0.8r$ sets a "speed limit" per computational cost for virtually all of the explicit algorithms considered here.

For the advection problem, the truncation error of spatial differencing always causes phase delay for high wavenumbers; therefore, a phase-lead error of the time stepping algorithm can be tolerated. In fact, if a second-order-accurate spatial discretization is used, there is no need for the use of an algorithm other than LF since its phase-lead error is always less than delay caused by spatial differencing, with compensation occurring only at the limit of stability. In the case of fourth- or higher-order

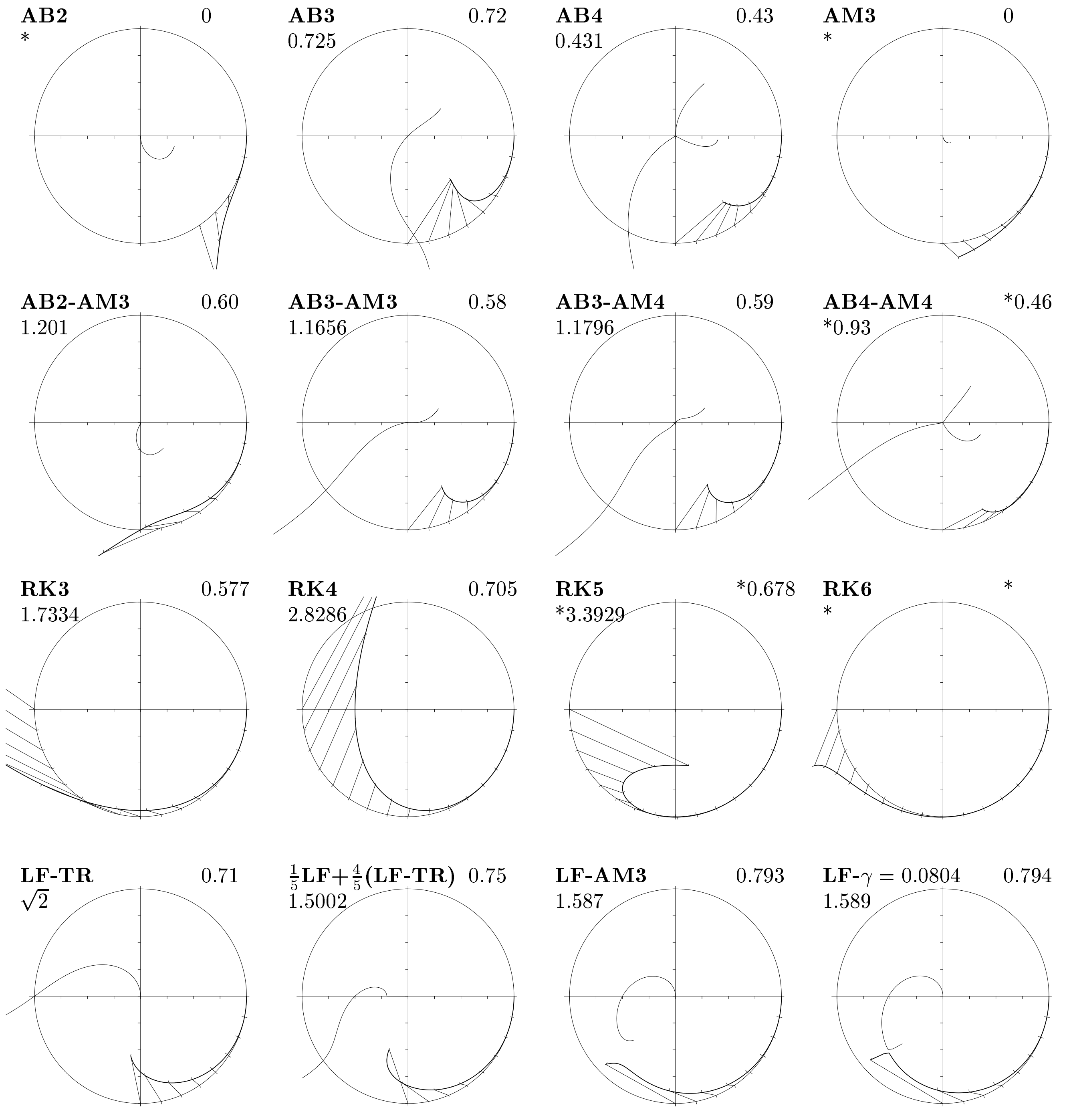

Figure 17. Amplification factors of various time-stepping methods plotted on the complex plane relative to the unit circle. Bold line corresponds to the physical mode and thin solid lines to the computational mode(s), if any. The legend is as follows: LF – Leap Frog; TR – trapezoidal rule; AB – Adams-Bashforth; AM – Adams-Moulton; RK – Runge-Kutta; Digits 2,3,4 denote order of accuracy. The number below the label is the stability limit. An asterisk (*) indicates asymptotic instability. (The physical mode of AB4-AM4 is weakly unstable; 0.93 is the threshold of strong instability of computational mode.) The number on the right is the efficiency factor (stability limit divided by the number of computations of right side). For each method, the roots of computational mode corresponding to "ideal" amplification factors of $\exp\left\{-\frac{\pi i}{16},\,,-\frac{\pi i}{8}\,,-\frac{3\pi i}{16}\,,\,\ldots\text{etc}\right\}$ are connected by straight lines with their ideal locations. This deviation illustrates the numerical error: shifts in azimuthal and radial directions correspond to phase and amplitude errors respectively.

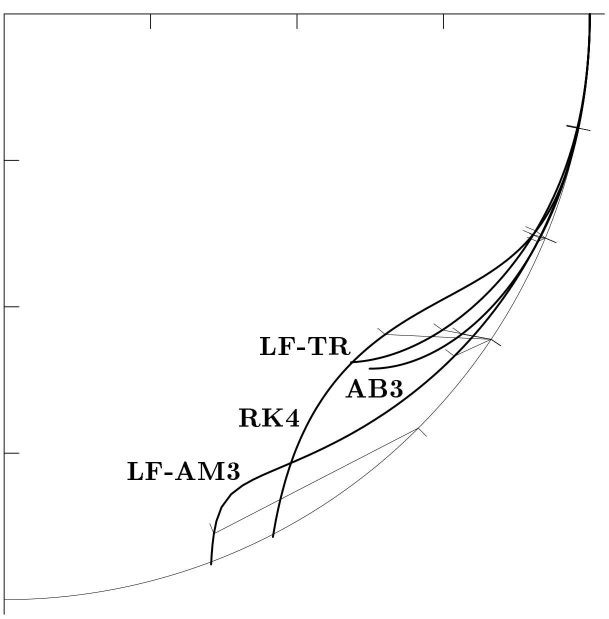

Figure 18. Fair comparison of time-stepping algorithms: amplification factor of physical mode normalized by the number of computations of right side. Each curve is shown within the limits of stability for the method.

spatial differencing, as well as for second-order differencing on a staggered grid (*e.g.,* the shallow-water system on a C-grid), the use of a higher-order algorithm (*i.e.,* AB3 or LF-AM3) is beneficial because the overall phase error may be dominated by the time-integration error.

Another method worth consideration is the generalized Adams-Bashforth step,

$$q^{n+1} = q^n + i\alpha\left\{\left(\frac{3}{2}+\beta\right)q^n - \left(\frac{1}{2}+2\beta\right)q^{n-1} + \beta q^{n-2}\right\} \quad \text{(A.12)}$$

where β is an adjustable parameter. The choice $\beta = 0$ corresponds to AB2, while $\beta = 5/12$ yields a third-order accurate AB3 that achieves the best possible order of accuracy on the given stencil. In the case where $\beta < 1/6$, the method has asymptotic instability of the physical mode (similar to that of AB2). Setting of $\beta = 0.281105$ corresponds to the case where the physical and one of the computational modes meet each other (Fig. 19). Below this value the instability of the physical mode occurs first (as in the case of LF-AM3), while past it one of the computational modes goes unstable first (as in the case of AB3). This β yields a stability limit of $\alpha = 0.78616$ that approximately coincides with that for the β value corresponding to the largest possible stability limit.

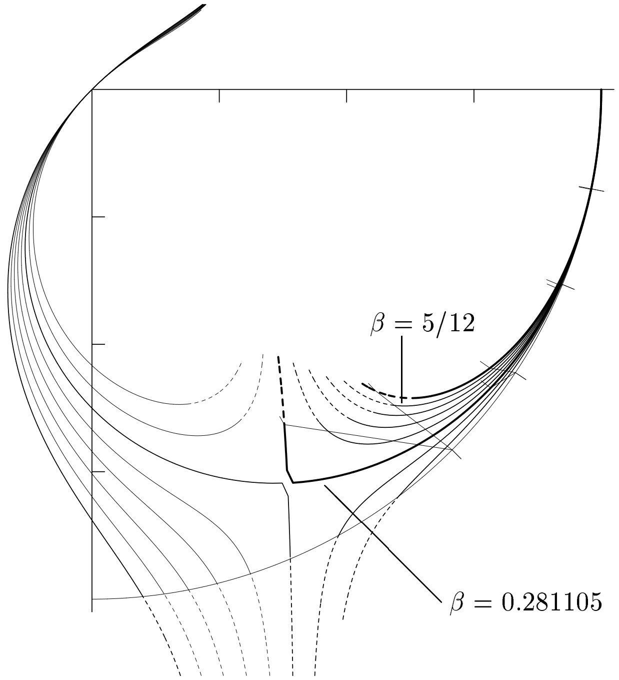

Figure 19. Positions of roots for Adams-Bashforth time-stepping algorithms. Highlighted curves correspond to $\beta = 0.281105$ (where the physical and one of the computational modes meet each other at the saddle point; this choice approximately coincides with the maximum possible stability limit of $\alpha = 0.78616$) and $\beta = 5/12$ (the usual third-order accurate AB3 method.).

Appendix B: Parabolic Spline Reconstruction

Regardless of the choice of values for $\rho_{k+\frac{1}{2}}$, $k = 1, ..., N-1$, the functional form of (3.16) guarantees that the reconstructed profile, $\rho(z)$, is continuous across grid-box interfaces because the side-limits $\rho_{k+\frac{1}{2}}$ are shared by the adjacent grid boxes H_k and H_{k+1}. Spline reconstruction implies that $\rho_{k+\frac{1}{2}}$ is determined from the requirement that the first derivative of ρ is also continuous. Differentiation of (3.16) with respect to z' yields

$$\frac{\partial\rho}{\partial z'} = \frac{\rho_{k+\frac{1}{2}} - \rho_{k-\frac{1}{2}}}{H_k} + 6\frac{\rho_{k+\frac{1}{2}} + \rho_{k-\frac{1}{2}} - 2\overline{\rho}_k}{H_k^2}z' \ , \quad \text{(B.1)}$$

which at the upper and lower interfaces of H_k has the values,

$$\left.\frac{\partial\rho}{\partial z'}\right|_{z'=+H_k/2} = +\frac{4\rho_{k+\frac{1}{2}} + 2\rho_{k-\frac{1}{2}} - 6\overline{\rho}_k}{H_k} \quad \text{(B.2)}$$

$$\left.\frac{\partial\rho}{\partial z'}\right|_{z'=-H_k/2} = -\frac{2\rho_{k+\frac{1}{2}} + 4\rho_{k-\frac{1}{2}} - 6\overline{\rho}_k}{H_k} \ . \quad \text{(B.3)}$$

Hence, to ensure continuity of the first derivative across the grid box interface $k+\frac{1}{2}$, we require

$$\frac{4\rho_{k+\frac{1}{2}}+2\rho_{k-\frac{1}{2}}-6\overline{\rho}_k}{H_k} = -\frac{2\rho_{k+\frac{3}{2}}+4\rho_{k+\frac{1}{2}}-6\overline{\rho}_{k+1}}{H_{k+1}}\,.$$

This leads to the tri-diagonal system of equations for $\rho_{k+\frac{1}{2}}$, $k=2,...,N-1$:

$$\begin{aligned} H_{k+1}\rho_{k-\frac{1}{2}}+2\left(H_{k+1}+H_k\right)\rho_{k+\frac{1}{2}}+H_k\rho_{k+\frac{3}{2}} & \\ = 3\left(H_{k+1}\overline{\rho}_k+H_k\overline{\rho}_{k+1}\right)\,. & \end{aligned} \tag{B.4}$$

The system (B.4) needs two boundary conditions at $k=1$ and $k=N$. These may be either physically motivated (*e.g.,* a Neumann condition stemming from a no-normal diffusive flux condition), or, if the formulation of a physical boundary condition is impossible, an appropriate extrapolation rule may be employed (which is equivalent to local reduction of the order of accuracy in the vicinity of the boundary). Some possible choices are the following:

Dirichlet: $\rho_{\frac{1}{2}}$ and $\rho_{N+\frac{1}{2}}$ are prescribed;

Neumann, [derived from (B.2)—(B.3) by setting them to zero or a prescribed known value]:

$$\rho_{\frac{1}{2}}+\frac{1}{2}\rho_{\frac{3}{2}}=\frac{3}{2}\overline{\rho}_1\,, \qquad \rho_{N+\frac{1}{2}}+\frac{1}{2}\rho_{N-\frac{1}{2}}=\frac{3}{2}\overline{\rho}_N\,.; \tag{B.5}$$

Linear Extrapolation, [assuming linear distributions within grid boxes H_1 and H_N, hence setting the quadratic term in (3.16) to zero]:

$$\rho_{\frac{1}{2}}+\rho_{\frac{3}{2}}=2\overline{\rho}_1\,, \qquad \rho_{N+\frac{1}{2}}+\rho_{N-\frac{1}{2}}=2\overline{\rho}_N\,; \tag{B.6}$$

Quadratic Extrapolation [assuming that the second derivative within the grid box adjacent to the boundary is the same as in the interior box adjacent to it]:

$$\begin{aligned} H_2\rho_{\frac{1}{2}}+\left(H_1+H_2\right)\rho_{\frac{3}{2}} &= \frac{H_2\left(2H_2+3H_1\right)}{H_1+H_2}\overline{\rho}_1 \\ &\qquad +\frac{H_1^2}{H_1+H_2}\overline{\rho}_2\,, \\ \left(H_N+H_{N-1}\right)\rho_{N-\frac{1}{2}}+H_{N-1}\rho_{N+\frac{1}{2}} & \\ = \frac{H_{N-1}\left(2H_{N-1}+3H_N\right)}{H_N+H_{N-1}}\overline{\rho}_N & \\ +\frac{H_N^2}{H_N+H_{N-1}}\rho_{N-1}\,. & \end{aligned} \tag{B.7}$$

References

Asselin, R, 1972: Frequency filter for time integations. *Monthly Weather Review*, **100**, 487-490.

Beckmann, A., 1998: The representation of bottom boundary layer processes in numerical ocean circulation models. in *Ocean modeling and Parametrization*, E. P. Chassignet & J. Verron, editors. *Kluwer Acad. Pub.,* pp. 135-154.

Bleck, R. and L. T. Smith, 1990: A wind-driven isopycnic coordinate model of the north and equatorial Atlantic Ocean: 1. Model development and supporting experiments. *Journ. Geophys. Res.*, **95C**, 3273-3285.

Blumberg, A. F. and G. L. Mellor, 1987: A description of a three-dimensional coastal ocean circulation model. In *Three-dimensional Coastal Ocean Models*, ed. N. Heaps (Pub. AGU), pp. 1-16.

Canuto, C., M. Y. Hussaini, A. Quarteroni and T. A. Zang, 1988: Spectral Methods in in Fluid Mechanics. *Springer-Verlag*, 567 pages

Dietrich, D. E., C. A. Lin, A. Mestas-Nunez and D.-S. Ko, 1997: A high resolution numerical study of Gulf of Mexico fronts and Eddies. *Meteorol. Atmos. Phys.*, **64**, 187-201

Dietachmayer, G. and K. Droegemeier, 1992: Application of continuous dynamic grid adaptation techniques to meteorological modeling. Part I: Basic formulation and accuracy. *Monthly Weather Review*, **120**, 1675-1706.

Dukowitz, J. K., R. D. Smith, and R. C. Malone, 1993: A reformulation and implementation of the Bryan-Cox-Semtner ocean model on the connection machine. *Journ. Atmos. Oceanic Technology*, **10**, 195-208.

Dukowitz, J. K., and R. D. Smith, 1994: Implicit free-surface method for the Bryan-Cox-Semtner ocean model. *Journ. Geophys. Res.*, **99**, 7991-8014.

Dukowicz, J. K., 1994: Computational efficiency of the hybrid penalty-pseudocompressibility method for incompressible flow. *Computers Fluids*, **23**, No 2, pp. 479-486.

Durran, D. R., 1991: The third order Adams-Bashforth method: An attractive alternative to leapfrog time differencing. *Monthly Weather Review*, **119**, 702-720

Dvinsky, A., S., and J. K. Dukowicz, 1993: Null-space-free methods for the incompressible Navier–Stokes equations on non-staggered curvilinear grids. *Computers Fluids*, **22**, No 6, pp. 685-696.

Farrow, D. E. and D. P. Stevens, 1995: A new tracer advection scheme for Bryan—Cox type ocean general circulation models. *Journ. Phys. Ocean.*, **25**, 1731–1741.

Haidvogel, D. B., H. Arango, K. Hedstrom, A. Beckmann, P. Rizzoli, and A. F. Shchepetkin, 2000: Model evaluation experiments in the North Atlantic Basin: Simulations in non-linear terrain-following coordinates. *Dyn. Atmos. and Oceans*, **32**, pp. 239-281.

Hallberg, R. W., 1997: Stable split time stepping schemes for large scale ocean modeling. *Journ. Comp. Phys.*, **135**, 54-65.

Haney, R. L., 1991: On the pressure gradient force over steep topography in sigma coordinate ocean models. *Journ. Phys. Ocean.*, **21**, 610-618.

Higdon, R. L. and A. F. Bennett, 1996: Stability analysis of operator splitting for large-scale ocean modelling. *Journ. Comp. Phys.*, **123**, 311

Higdon, R. L. and R. A. de Szoeke, 1997: Barotropic-Baroclinic Time Splitting for Ocean Circullation Modeling. *Journ. Comp. Phys.*, **135**, 31-53.

Hyman, J. M., 1979: A method of lines aproach to the numerical solution of conservation laws, *Advances in computer methods for partial differential equations*, Vol. III, ed. R. Vichnevetsky and R. S. Stepleman, (Pub, IMACS), pp. 313-321.

Killworth, P. D., D. Stainforth, D. J. Webb and S. M. Paterson, 1991: The development of a free-surface Bryan-Cox-Semtner ocean model. *Journ. Phys. Ocean.*, **21**, 1333-1348.

Leonard, B. P., A. P. Lock and M. K. McVean, 1996: Conservative explicit unrestricted-time-step constancy preserving advection schemes. *Monthly Weather Review*, **124**, 2588-2606.

Lilly, D. K., 1965: On the computational stability of time-dependent non-linear geophysical fluid dynamics problem. *Monthly Weather Review*, **93**, 11-26.

Lin, Shian-Jiann, 1997: A finite volume integration method for computing pressure gradient force in general vertical coordinates. *Q. J. R. Meteorol. Soc.*, **123**, 1749-1762.

Marchesiello, P., J.C. McWilliams, & A. Shchepetkin, 2003: Equilibrium structure and dynamics of the California Current System. *J. Phys. Ocean.*, in press.

Mesinger, F., and A. Arakawa, 1976: Numerical Methods used in atmospheric models, Vol. 1, GARP Publ. Ser. 17., World Meteor. Org., 64 pp.

Mesinger, F., 1982: On the convergence and error problems of the calculation of the pressure gradient force in sigma coordinate ocean models. *Geophys. Astrophys. Fluid Dyn.*, **19**, 105-117.

Multigrid Methods, 1981: NASA conference publication 2202. 303 pages. call # QA 377 M944.

Nadiga, B. T., M. W. Hecht, L. G. Margolin, and P. K. Smolarkiewicz, 1997: On Simulating Flows with Multiple Time Scales Using a Method of Averages. *Theor. and Comput. Fluid Dyn.*, **9**, 281-292.

Shchepetkin, A. F., and J. C. McWilliams, 2003: A method for computing horizontal pressure-gradient force in an oceanic model with a non-aligned vertical coordinate. *J. Geophys. Res.*, in press

Skamarock, W. C., and J. B. Klemp, 1992, The stability of time-split numerical methods for the hydrostatic and the nonhydrostatic elastic equations. *Monthly Weather Review*, **120**, 2109–2197.

Song, Y. T., and D. Haidvogel, 1994: A Semi-implicit ocean circullation model using a generalized topography following coordinate system, *Journ. Comp. Phys.*, **115**, 228-248.

Treguier, A. M., J. K. Dukowicz, and K. Bryan, 1996: Properties of nonuniform grids used in ocean general circullation ocean models. *Journ. Geophys. Res.*, **101**, 20877-20881.

Willebrand, J., B. Barnier, C. Böning, C. Dieterich, P.D. Killworth, C. LeProvost, Y. Jia, J.-M. Molines, A.L. New, 2001: Circulation characteristics in three eddy-permitting models of the North Atlantic. *Progress in Oceanography*, **48**, pp. 123-161.

Yanenko, N. N., 1977: The method of fractional steps, Springer-Verlag, 160 pages.

This preprint was prepared with the AGU LATEX macros v3.1. File roms formatted 2003 March 10.